POLARIZATION OPTICAL COMPONENTS OF THE DANIEL K. INOUYE SOLAR TELESCOPE

by

Stacey Ritsuyo Sueoka

A Dissertation Submitted to the Faculty of the

COLLEGE OF OPTICAL SCIENCES

In Partial Fulfillment of the Requirements

For the Degree of

DOCTOR OF PHILOSOPHY

In the Graduate College

THE UNIVERSITY OF ARIZONA

2016

THE UNIVERSITY OF ARIZONA

GRADUATE COLLEGE

As members of the Dissertation Committee, we certify that we have read the dissertation prepared by Stacey Sueoka, titled Polarization Optical Components of the Daniel K. Inouye Solar Telescope, and recommend that it be accepted as fulfilling the dissertation requirement for the Degree of Doctor of Philosophy.

____ Date: April 26, 2016
Russell A. Chipman

____ Date: April 26, 2016
David F. Elmore

____ Date: April 26, 2016
J. Scott Tyo

Final approval and acceptance of this dissertation is contingent upon the candidate's submission of the final copies of the dissertation to the Graduate College.

I hereby certify that I have read this dissertation prepared under my direction and recommend that it be accepted as fulfilling the dissertation requirement.

____ Date: April 26, 2016
Russell A. Chipman

STATEMENT BY AUTHOR

This dissertation has been submitted in partial fulfillment of the requirements for an advanced degree at the University of Arizona and is deposited in the University Library to be made available to borrowers under rules of the Library.

Brief quotations from this dissertation are allowable without special permission, provided that an accurate acknowledgement of the source is made. Requests for permission for extended quotation from or reproduction of this manuscript in whole or in part may be granted by the copyright holder.

SIGNED: Stacey Ritsuyo Sueoka

ACKNOWLEDGEMENTS

I would like to thank my advisor Dr. Russell Chipman for the introduction to the fascinating world of polarimetry and the wonderful opportunity to join the polarimetry community. I am very grateful for Russell’s encouragement to become a better researcher, public speaker and “retarder expert”.

I would like to thank my Polarization Lab group members who were not only colleagues but also great supportive friends: Soon to be Dr. Christine Bradley, Dr. Garam Young, Dr. Hannah Noble, Dr. Anna-Britt Mahler, Dr. Tiffany Wai-Sze Lam, Dr. Paula Smith, Dr. Alba Peinado and soon to be Dr. Brian Daugherty. Many trips to Café Luce and Allegro Gelato kept me grounded in life. I would like to thank Brittany Foster and Nirantha Balagopal, for their help performing laboratory measurements that supported my work on super achromatic waveplates. I am very grateful to Russell, Dr. Steve McClain, Dr. Greg Smith and Dr. Karlton Crabtree for sharing their expertise in polarimetry.

I would like to thank the late Senator Inouye, who was a strong advocate for science and technology in Hawaii. If it weren’t for him, I wouldn’t have had the opportunities that lead me to pursuing graduate school in Optical Sciences. I would like to thank all of my team members on the Daniel K. Inouye Solar Telescope project. I am grateful to Bill McBride, who introduced me to the project and opened the doors for me to join the DKIST team. I would like to thank David Elmore for mentoring me and serving on my dissertation committee as a Solar Polarimetry Expert. David’s expertise in Lincoln National Forest railroad history also made for fun discussions and fantastic hiking adventures. I would like to thank the DKIST Polarimetry Scientist Dave Harrington for the many hours of discussing polarimetry, engineering, modeling, flying and photography. I am grateful for his support and encouragement to finish this dissertation work. I am extremely grateful to the DKIST Project Director Thomas Rimmele, DKIST Project Manager Joe McMullin, and NSO Director Valentin Martinez Pillet for allowing me to be a part of such an incredible engineering project. I would like to thank my DKIST PA&C team members, Andy Ferayorni, Scott Gregory, Chris Runyan, Wes Cole, Dave Harrington and Austin Kootz, in this collaborative effort to build the world’s greatest solar telescope!

I would like to thank the faculty at Pacific University, in particular Dr. Brosing and Dr. Butler, for providing me with strong fundamentals in physics and

encouraging me to pursue graduate school in Optical Sciences. I also would like to thank the Hawaii Club, Pacific Soccer team, and my many good friends and sisters that I grew close to over the years.

I would like to thank Lisa Hunter, Director of the Akamai Workforce Initiative, for all of her time and commitment in supporting students from Hawaii pursuing STEM related research and careers. If it weren't for the Akamai Alumni Workshop held in the fall of 2011 I never would have been introduced to NSO and the DKIST project.

I would like to thank Dr. Michael Jacobson at Optical Data Associates and Elena Temyanko of Dr. Peyghambarian's research group for their laboratory time and help in the birefringence measurements.

I would like to thank the faculty and administrative staff at the College of Optical Sciences. I would like to thank Dr. Russell Chipman, Dr. Masud Mansuripur, Dr. Harry Barrett, Dr. John Greivenkamp, Dr. Hong Hua, Dr. Tom Milster, Dr. Mike Nofziger, Dr. José Sasián, Dr. John Koshel, Dean Tom Koch, Dr. Jim Wyant, and Dr. Jim Schwiegerling, for their selfless efforts to keep the college competitive and at the forefront of innovation, and for providing excellent optics courses and outreach programs. In particular, I would like to thank Dr. Scott Tyo, not only for serving on my dissertation committee but for his excellent teaching techniques, hard work and commitment to his students. I would also like to thank the friendly faces of the optics department who always were supportive and put a smile on my face: Lucy Valenzuela and her daughter Kiana, Cindy Gardner, Melissa Ayala, Ashley Bidegain, Ruth Corcoran, Kevin Erwin, Marco Favela, Amanda Ferraris, Mark Rodriguez, Hector Garcia, Jennifer Garcia, Kristin Waller, Graeme Hunt, Anabel Moreno, Oli Nordman, Susan Nares, Luz Palomarez, Amy Phillips, Mary Puig, Trin Riojas, Cindy Robertson, Laura Ross, Kay Rowen and Justin Walker.

I am extremely thankful for all of the family and community support that has brought me to this life achievement. I would especially like to thank my parents, Ernest and Janet Sueoka, and my sister Kim Sueoka, for all the love and support. I am grateful for my dad's early efforts to help me with my high school math assignments, he will always be faster at mental math than me but I accept this fact. I would like to thank my grandpa, James Sadami Okada, whose imagination and creativity to build practical and useful things out of anything sparked my initial interest in becoming an engineer. I would like to thank my math teachers Mrs. Uyematsu and Mrs.

Yamamoto, and science teacher Mr. Snow for the positive learning environment they created in their classrooms at Kauai High School. I would like to thank a good family friend Clyde Shiraki and Kauai Community College for my first technology internship opportunity back in 2004 at PMRF. I am very grateful to Aunty Lily and Aunty Eunice, who I love dearly and have constantly cooked and sent goodies to me so I did not starve in grad school. I would like to thank the many positive people in my childhood and while growing up on Kauai: my half siblings Steve and Karen and their families, my Sueoka Store family, all of the Aunties and Uncles of the Pulehu Gang and Waikomo Club House, my Okada and Yamada family, my adopted family the Machado's, the Santos's and the Kaneshiro's.

Last but not least, I would like to thank my friends. I am extremely thankful for the friendships I made during graduate school. We went through a lot together and supported one another along they way. I will never forget the many long evenings doing homework on the 8th floor with the SAGUARO crew: Zach, Laura, Blake, Jennifer, Sam, Ezra, Mihal, Chen and Jason and the grueling prelim studies with Karr, Ayo, Nick, Kevin and Chris. The highlights of those times were the many parties for Halloween, prelim celebrations and other DJ Yogi events. I am very grateful for the friends I met through Tucson soccer leagues: the U of A intramural team, SDFC, A Cup United, and the rest of my Maracana soccer family. I would like to thank all of my other friends who helped keep me sane over the years: Havasu adventure gang: Anael, Christine, Tony, Andrey, Geri, and Ross, Game of Thrones dinner party crew, French pastry baking sessions and Cheese party friends. I would like to thank Anael Guilmo, for his love and support. His love for adventure, good food, and amazing French-Vietnamese cooking helped me through the stressful days of dissertation writing.

The research reported herein is based in part on data collected with the Daniel K. Inouye Solar Telescope (DKIST), a facility of the National Solar Observatory (NSO). NSO is funded by the National Science Foundation under a cooperative agreement with the Association of Universities for Research in Astronomy, Inc.

DEDICATION

To my parents Jan and Ernest Sueoka, sister Kim, Aunty Lily, Aunty Eunice, Grandma Tsugie Okada and Grandpa Sadami Okada.

TABLE OF CONTENTS

LIST OF TABLES

LIST OF FIGURES

ABSTRACT

The Daniel K Inouye Solar Telescope (DKIST), when completed in 2019 will be the largest solar telescope built to date. DKIST will have a suite of first light polarimetric instrumentation requiring broadband polarization modulation and calibration optical elements. Compound crystalline retarders meet the design requirements for efficient modulators and achromatic calibration retarders. These retarders are the only possible large diameter optic that can survive the high flux, 5 arc minute field, and ultraviolet intense environment of a large aperture solar telescope at Gregorian focus.

This dissertation presents work performed for the project. First, I measured birefringence of the candidate materials necessary to complete designs. Then, I modeled the polarization effects with three-dimensional ray-tracing codes as a function of angle of incidence and field of view. Through this analysis I learned that due to the incident converging F/13 beam on the calibration retarders, the previously assumed linear retarder model fails to account for effects above the project polarization specifications. I discuss modeling strategies such as Mueller matrix decompositions and simplifications of those strategies while still meeting fit error requirements. Finally, I present characterization techniques and how these were applied to prototype components.

1 INTRODUCTION

The Daniel K Inouye Solar Telescope (DKIST), when completed in 2019 will be the largest solar telescope built to date. A telescope project of this large scale takes years of planning, development and construction. The project is broken down into sub-components where teams of engineers and scientists focus on specific parts of the telescope. DKIST will have five first light instruments, four of which are polarimeters. All of those polarimeters rely upon the Polarization Analysis and Calibration (PA&C) subsystem. This subsystem primarily consists of the Gregorian Optical Station (GOS) located near the Gregorian focus of the telescope and the polarization modulation optical elements. The modulator elements are provided by the project to the polarimeter instrument partners and are incorporated into the instrument optical system. The GOS is divided into two sections, the upper and lower GOS. The upper GOS houses the artificial light source and polarization calibration optics. The lower GOS has a rotating wheel that holds apertures, targets, occulter, and other alignment tools. This chapter provides further background information on the DKIST project that is important to understand the scope of this dissertation.

The calibration and modulator retarders were deemed high-risk components in the PA&C system. It was known that design and fabrication would be difficult and require extra effort, as current capabilities in technology do not provide a commercial off the shelf solution. It had been determined that designs would include one or more of the materials: crystalline quartz, sapphire or magnesium fluoride. Due to a lack of consistency in the published birefringence as a function of wavelength data the designs could not be reliably completed. Chapter 2 describes the birefringence measurements and generation of functions for use in the DKIST retarder designs.

The final selected retarder designs utilize quartz for the visible to near infrared retarders, and magnesium fluoride for the infrared instrument retarders. Each retarder is composed of a stack of 6 crystal plates with fast axis clocked at different angles. Chapter 3 explains the designs and fabrication requirements.

The normal incident behaviors of these retarder components are well characterized and shown in Chapter 3. In Chapter 4 I discuss angle of incidence effects. The retarders are located in a converging beam, therefore off-axis performance as a function of angle of incidence becomes significant. A three-dimensional polarization ray trace was performed with Polaris-M, software developed in house by Dr. Russell Chipman's polarization laboratory. A key utility of this software is the ability to handle anisotropic ray tracing, the splitting of modes through anisotropic materials and the algorithms to combine the effects. Ray tracing was performed over the 5 arc-minute and 2.8 arc-minute fields of view, and an incoherent sum (averaging) of the Mueller matrices was calculated for every field point.

The baseline polarization calibration plan fits the calibration retarder to an ideal linear retarder Mueller matrix. In modeling of the average Mueller matrices two conclusions are made. First, the average Mueller matrices do not fit the ideal linear retarder Mueller matrix to within the polarimetric error budget allocated to these optical elements. Therefore, other options for parameterizing the Mueller matrix for calibration must be determined. Second, variations as a function of field must be fit in order to stay within the polarimetric error budget. In Chapter 5 Mueller matrix decomposition methods are investigated to determine a minimal parameter solution to fitting the retarder models. Symmetric decomposition resulted in a physically realizable set of Mueller matrices that fit the Mueller matrix as a function of field of view. The modulator Mueller matrix is not fit, as it is part of the modulation matrix determined by the end-to-end polarization calibration.

The NSO laboratory spectro-polarimeter (NLSP) was used and will continue to be used to perform the acceptance tests of the as-built retarder components. The DL-NIRSP calibration retarder and modulator were the first assembled. Preliminary tests on these retarders with the NLSP are described in Chapter 6.

1.1 Daniel K. Inouye Solar Telescope

The Daniel K. Inouye Solar Telescope was formerly known as the Advanced Technology Solar Telescope (ATST). The name was changed in 2013 in honor of Hawaii's late Senator Daniel K. Inouye, who was strongly committed to fundamental scientific research and discovery, and was an advocate for the ATST. DKIST is a facility of the National Solar Observatory (NSO), funded by the National Science Foundation (NSF) under a cooperative agreement with the Association of Universities for Research in Astronomy (AURA), Inc.

DKIST will be an important tool to address fundamental questions in solar physics. It will be the largest aperture solar telescope, providing high resolution imaging capabilities to study the Sun's magnetic activity, including sunspots, flares, coronal mass ejections, the solar wind and solar variability (T. R. Rimmele et al., 2010). Figure 1.1 illustrates the spatial and spectral range of DKIST in comparison to other solar telescopes. DKIST will provide the highest spatial resolution in the visible spectrum, as well as broaden observations in the near infrared.

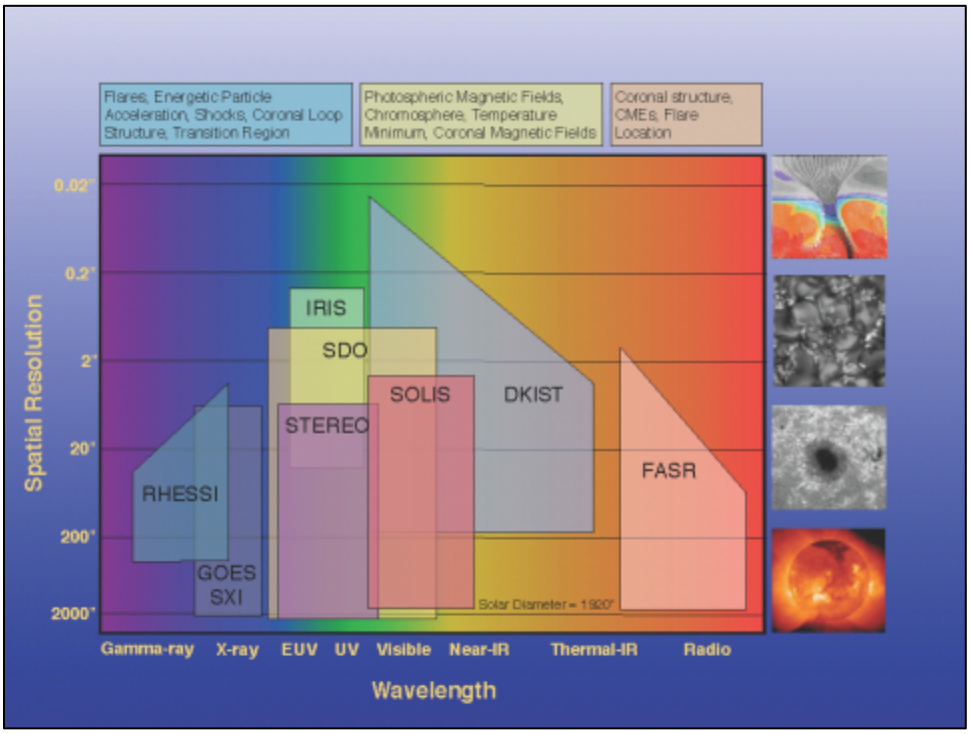

Figure 1.1: Spatial resolution and spectral range of several solar telescopes. From DKIST website. DKIST will have higher spatial resolution than current telescopes over the visible wavelengths. DKIST will expand to IR wavelengths not currently observed. NSO/AURA/NSF.

1.1.1 Site selection: Haleakalā, the “House of the Sun”

The Hawaiian archipelago is a chain of volcanic islands in the middle of the Pacific Ocean, formed over an undersea magma source and slowly pushed northwest by tectonic plate movement. The younger islands of Maui and Hawai’i have high mountaintops and the peaks sit above the inversion layer of the Earth’s atmosphere, therefore the air is clear, dry and stable. The gentle slopes result in less air turbulence and provide a still and dry environment. These locations are considered some of the best in the world for performing astronomical observations. It is not surprising that Maui’s own Haleakalā mountain has been selected out of 72 proposed sites as the prime site for building the world’s largest solar telescope (Navarro et al., 2005). 6 of the 72 sites were selected for site survey testing due to their many continuous hours of sunshine and geographical features believed to be advantageous for solar observing. Those sites included: Sacramento Peak (New Mexico), Panguitch Lake (Utah), San

Pedro Martir (Baja California), Big Bear (California), Haleakalā (Hawaii), and La Palma, (Canary Islands, Spain). Identical instrumentation was placed at each of these sites for a comparative survey of daytime seeing and sky brightness. For daytime observations Haleakalā meets the site criteria of providing low sky brightness levels, lowest dust levels, and the smallest temperature extremes. Only Haleakalā is able to meet the DKIST requirement for excellent seeing, site survey results showed Haleakalā has the most annual hours of excellent seeing conditions (Hill et al., 2006).

1.1.2 Large telescope aperture for high spatial resolution

Dr. Dae Wook Kim describes DKIST as a giant microscope! Current solar telescopes due to their limited aperture cannot resolve small-scale dynamic structures that contribute to solar activity. Spatial resolution necessary to resolve fundamental astrophysical processes at their intrinsic scales in the solar atmosphere can be achieved with a large aperture solar telescope. The DKIST 4 meter aperture, 4.24-meter diameter primary mirror, is designed to provide high spatial resolution over the telescope operation wavelength range. For example, the telescope will have a spatial resolution of 20 km on the Sun, 0.03” angular resolution at visible wavelengths and up to 0.1” angular resolution in the near infrared (T. R. Rimmele et al., 2010). The large aperture also provides higher flux necessary for high spectral and temporal resolution requirements, but is achieved only at less than the diffraction limit.

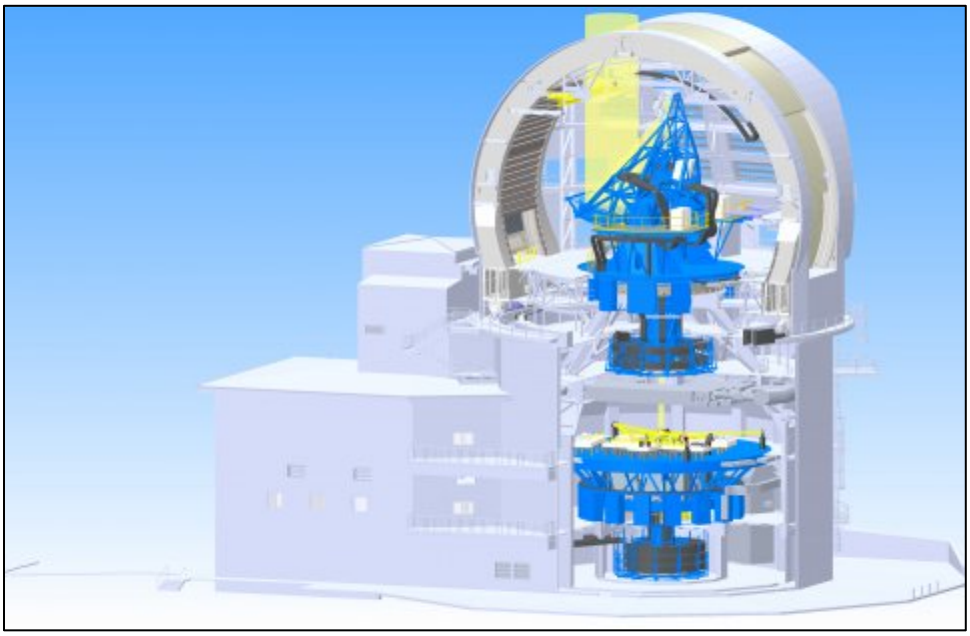

Figure 1.2: Model of the DKIST building facility. A slice through the dome reveals the structure of the telescope from the primary mirror down to the Coudé laboratory platform. NSO/AURA/NSF.

1.1.3 Optical path

The main telescope optical path is shown in Figure 1.3 from the primary mirror **M1**, down to mirror **M9**, on the Coudé laboratory platform. A unique feature of DKIST is its F/2 off-axis Gregorian telescope design. In order to keep the secondary optics out of the collection beam path, the primary mirror is off-axis. The off axis design was chosen primarily to avoid problems due to heated optics in the aperture, and to avoid scattering off structures and optical elements that would hinder faint solar corona light measurements. Secondary mirror **M2**, a 65 cm diameter off-axis aspheric concave mirror, is located in the Top End Optical Assembly (TEOA). The TEOA also contains the Heat Stop Assembly (HSA). The HSA is located at the prime focus of **M1**; it is the first field stop and allows a 5 arc minute field of view to feed down the optical train.

The light reflected off of **M2** produces a F/13 converging beam that comes to focus before **M3**. A subsystem called the Gregorian Optical Station (GOS) is mounted to the telescope mount assembly near the focus. It consists of an artificial light source, polarization calibration optics, and a large aperture wheel that contains alignment targets, field stops and a limb occulter. Following GOS is **M3**, a flat mirror that reflects the beam to **M4**, a powered mirror. The elevation rotation occurs between **M4** and **M5** because they lie along the elevation axis of the telescope. **M5** is utilized as a fast steering flat mirror because it is located near a pupil. Light is reflected off of another flat, **M6**, and sent down to the Coudé laboratory. Coudé – azimuth rotation occurs between **M6** and **M7**. The light is then relayed across the Coudé laboratory where mirrors **M7** through **M9** reimage a system pupil for the instruments and the adaptive optics system.

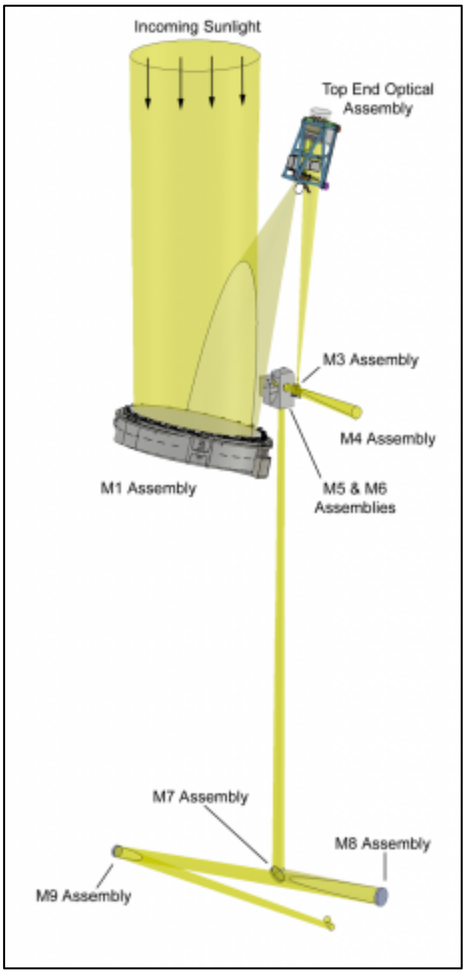

Figure 1.3: DKIST optical path showing the beam path reflected off of mirrors 1 through 9. NSO/AURA/NSF.

1.1.4 Polarization requirements

To infer the Sun’s magnetic activity DKIST must measure polarization and calibrate those measurements. Fundamental science questions drive extremely challenging polarization sensitivity and accuracy requirements for the telescope. The Science Requirements Document states that the polarization sensitivity needs to be less than 1×10^{-5}, which is the amount of fractional polarization that can be detected above a constant background and limited by photon noise (T. Rimmele, 2005). The requirements also state that polarization accuracy needs to be less than 5×10^{-4} of the continuum intensity, which is the absolute error in measured fractional polarization.

1.1.5 First Light Instruments

Five instruments shown in Figure 1.4 will be in operation when the telescope is commissioned. Four are spectro-polarimeters designed to fully measure all four Stokes parameters, the fifth instrument will only perform imaging. Overall, they will span the wavelength range from 0.38 to 5 µm. With a unique set of dichroic beam splitters and window optics in the Coudé laboratory, multiple instruments can operate simultaneously. Two of the spectro-polarimeters are called wavelength diverse because the instruments have multiple reconfigurable detector arms and can measure multiple spectral lines simultaneously. The other two spectro-polarimeters are only wavelength agile, they have the ability to rapidly switch observation wavelength but can only measure a single spectral line at a time. The instrument design and fabrication tasks lies with different instrument partners, although ultimately it is the DKIST team responsibility that all first light instruments are fully operational. A brief overview of the instruments specifications, configurations, and wavelength range follows.

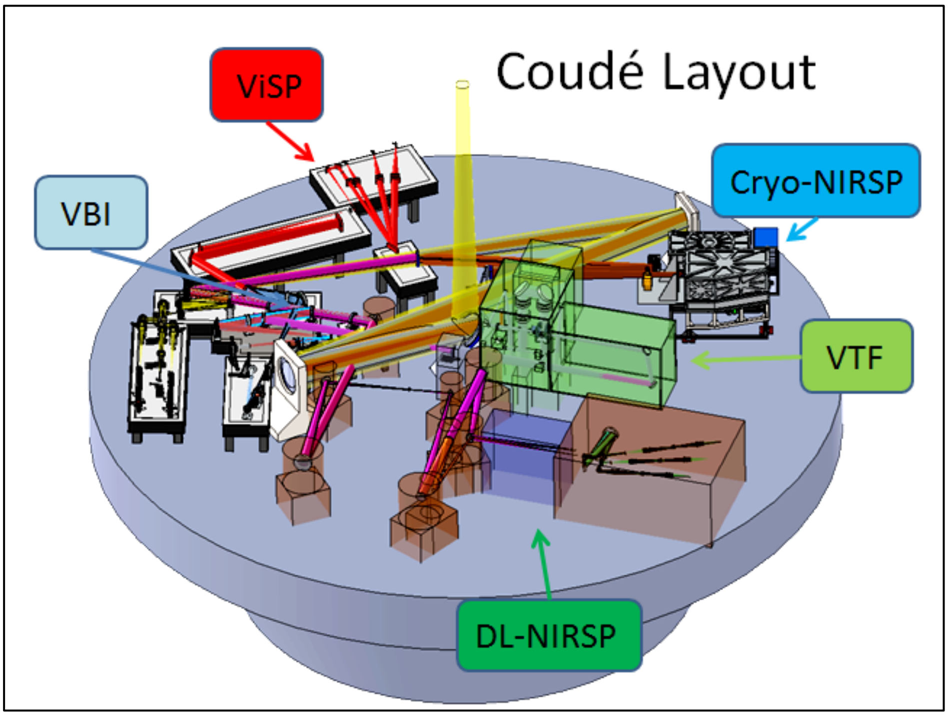

Figure 1.4: Layout of the 5 first light instruments. All are polarimeters except VBI. Adapted from NSO/AURA/NSF.

1.1.5.1 Visible Broadband Imager (VBI)

The VBI, developed by NSO, is the sole first light instrument that will not perform polarimetry. The principal investigator is Dr. Friedrich Wöger. The goal of the VBI is to simultaneously record images at wavelengths within two spectral ranges that span 390 nm to 860 nm. The VBI is split into two channels called Blue and Red. The Blue channel is optimized at 430 nm and operates from 390 to 490 nm. The primary wavelength of the Red channel is 656.3 nm and operates from 600 to 860 nm. Multiple wavelengths allow one to observe different layers of the solar photosphere and chromosphere. The VBI will provide high quality images at a very fast rate by utilizing high spatial and temporal resolution to sample a 4-meter telescope.

1.1.5.2 Visible Tunable Filter (VTF)

Kiepenheuer Institute for Solar Physics is in charge of the VTF design and fabrication. The principal investigator is Dr. O. von der Lühe, and the instrument scientist is Dr. Wolfgang Schmidt. The VTF is a dual Fabry-Perot instrument with spectral range from 520 to 860 nm. It is a polarimeter with a ferroelectric liquid crystal modulator and polarizing beam splitter analyzer. The goal of the VTF is to spectrally isolate narrow-band images of the Sun at the highest possible spatial and temporal resolution from the DKIST telescope. The VTF will have many operational modes; in a typical mode it will sample a line profile with 12 samples and observe each line position for about a second. This allows a two dimensional solar image at a dozen wavelengths across the spectrum line in less than 15 seconds.

1.1.5.3 Visible Spectro-Polarimeter (ViSP)

The ViSP is an instrument developed by the High Altitude Observatory (HAO) and the National Center for Atmospheric Research (NCAR), in Boulder, CO. The project’s principal investigator is Dr. Roberto Casini, and instrument scientist Dr. Alfred de Wijn. The ViSP is an Echelle spectrograph, with a rotating retarder modulator and polarizing beam splitter analyzer that will provide full Stokes parameters for up to three wavelengths simultaneously (de Wijn, Casini, Nelson, & Huang, 2012). The polarimeter will observe spectral lines that fall within a range of 380 to 900 nm. There is a goal to go reach 1600 nm, however with a silicon detector it is only capable of measuring up to 1100 nm. The instrument can be quickly reconfigured to change the observation lines. The spatial sampling will be twice the DKIST resolution or better, and a spatial FOV of 2x2 square arc minute. The spectral resolving power will be greater than 180,000. Theoretically, polarimetric signals down to 10^{-3} times the intensity continuum can be observed within 10 seconds. The goal of ViSP is to provide quantitative diagnostics of the magnetic field vector as a function of height in the solar atmosphere, along with associated variation of the thermodynamic properties. Analyzing the polarization of strong lines during flares will provide information about plasma dynamics.

1.1.5.4 Diffraction Limited Near Infrared Spectro-Polarimeter (DL-NIRSP)

DL-NIRSP is an instrument of the Institute of Astronomy at the University of Hawaii. The principal investigator is Dr. Haosheng Lin and instrument scientist Dr. Thomas Schad. The DL-NIRSP is a reflection grating based multi-armed off-axis integral field Littrow spectrograph being built by a group at the Institute for Astronomy at the University of Hawaii. The instrument is designed to measure full Stokes parameters from 500 to 1800 nm. It has three detector arms, resulting in a wavelength diverse instrument. In other words, it can measure up to three wavelengths simultaneously, one each from three bands separated by dichroic beam splitters. The unique part of this instrument is its use of fiber-optic based integral field spectroscopy (David F. Elmore, Rimmele, et al., 2014). The core of this instrument relies on the fiber-based Integral Field Unit (IFU). The IFU reformats the two dimensional spatial field into several parallel slits, each of which containing fiber ribbons separated by dark pixel rows. The instrument will perform imaging up to the diffraction limit at 900 nm, and have a spectral resolving power from 70,000 to 250,000. By scanning the solar image across the IFU a total field of view will cover up to 120 x 120 arc-seconds. The instrument contains a rotating retarder modulator and Wollaston prisms for dual-beam full Stokes polarimetry.

1.1.5.5 Cryogenic Near Infrared Spectro-Polarimeter (Cryo-NIRSP)

The final first light instrument is the Cryo-NIRSP, also being developed by the University of Hawai'i, Institute for Astronomy. The principal investigator is Dr. Jeffrey Kuhn, and the instrument scientist is Dr. André Fehlmann. The Cryo-NIRSP has a primary purpose to study the solar coronal magnetic fields over a large field of view at near and thermal wavelengths (David F. Elmore, Rimmele, et al., 2014). It is a cryogenically cooled Echelle spectrograph which contains a long slit spectrograph and a two-dimensional intensity imager with passband filters. The wavelength range is from 1000 to 5000 nm, with a goal to extend to 500 nm. The instrument is wavelength agile, and can change measurement wavelengths within 10 seconds. The instrument operates in two modes, coronal and disk. The spectral resolving power is 30,000 for coronal observations, and 100,000 for on disk observations. The field of view for coronal mode is 4 arc minutes parallel to the limb and 3 arc minutes perpendicular to the limb. In disk mode the field of view is 1.5 arc minutes square.

1.2 DKIST Polarimetry

Polarimetry and imaging are necessary measurements to study the Sun's surface and atmosphere. High spatial, spectral and temporal imaging provide one look at the small dynamic effects of the Sun, polarimetry will provide more dimensions for analysis.

1.2.1 Common effects observed with polarimetry

The Zeeman effect is the splitting of atomic energy levels in the presence of a magnetic field. Separated spectrum lines emit different polarization states and are used to infer both the magnitude and orientation of the magnetic field. Another more subtle effect of magnetic fields on scattering polarization is known as the Hanlé effect. There are linear polarized spectrum lines that form dominantly by scattering in the solar atmosphere. Atomic level crossings induced by weak magnetic fields produce circular polarization.

1.2.2 Stokes Polarimetry

1.2.2.1 Stokes vector representation

Stokes formulism is used for solar polarimetry rather than Jones because of its ability to characterize partially polarized light. Stokes parameters, also known as the four-element Stokes vector, represent un-polarized, partially polarized and fully polarized light. The Stokes vector describes the statistics of the electric and magnetic fields in the transverse plane from the propagation direction of light. It provides the orientation of the transverse electromagnetic waves with the difference in intensity of the orthogonal polarization states. It describes the time averaged polarization properties of an electromagnetic field. Any state of polarized light can be completely described by the four measurable quantities of the Stokes vector. The first describes the total intensity, and the remainder describes the polarization state. It is arranged in a column vector and written as

$$\boldsymbol{S} = \begin{pmatrix} \boldsymbol{S_0} \\ \boldsymbol{S_1} \\ \boldsymbol{S_2} \\ \boldsymbol{S_3} \end{pmatrix}. \tag{1.1}$$

Stokes parameters are directly measurable and can result from the sums and differences of intensities. Consider the measurement of a stable partially polarized light source with a simple lab experiment. A detector measures the intensity of the light. One at a time, six polarizers are placed in front of the detector and a measurement is taken. These polarizers are a horizontal linear polarizer, a vertical linear polarizer, a $45°$ linear polarizer, a $-45°$ linear polarizer, a left circular polarizer and a right circular polarizer. The Stokes parameters are calculated with the sums and differences of these measurements: $S_1$is the difference between horizontal and vertical polarized flux, S_2 is the difference between $45°$ and $-45°$ polarized flux, S_3 is the difference between right circular and left circular polarized flux, and S_0 is the sum of any two fluxes that result in S_1, S_2, or S_3.

The example polarimeter described above follows the definition of the Stokes vector and is not an efficient or practical method of measuring Stokes parameters. The detector itself may have several instabilities and moving optics can destabilize the beam path. These effects can reduce the polarization accuracy and precision of the system. To avoid detector polarization sensitivity the polarimeter can be divided into a modulator and analyzer. Such a polarimeter is described in Section 1.2.3.

1.2.2.2 Mueller matrix representation

Light incident on the telescope will refract or reflect through the optical system. Mueller matrices are used to describe the polarization-altering characteristics of matter interacting with an incident light beam. Each optical element in the telescope can be represented as a 4x4 Mueller matrix written as

$$\boldsymbol{M} = \begin{pmatrix} \boldsymbol{m_{0,0}} & \boldsymbol{m_{0,1}} & \boldsymbol{m_{0,2}} & \boldsymbol{m_{0,3}} \\ \boldsymbol{m_{1,0}} & \boldsymbol{m_{1,1}} & \boldsymbol{m_{1,2}} & \boldsymbol{m_{1,3}} \\ \boldsymbol{m_{2,0}} & \boldsymbol{m_{2,1}} & \boldsymbol{m_{2,2}} & \boldsymbol{m_{2,3}} \\ \boldsymbol{m_{3,0}} & \boldsymbol{m_{3,1}} & \boldsymbol{m_{3,2}} & \boldsymbol{m_{3,3}} \end{pmatrix}. \tag{1.2}$$

The Mueller matrix is a 4x4 matrix of real numbers that transforms input Stokes vectors into output Stokes vectors. The Mueller matrix of the optical element can be dependent on a number of factors: wavelength, temperature, angle of incidence, orientation of the optic with respect to the local coordinate system to name a few.

Due to constraints in time, spatial and spectral resolution and a large number of instrumental reasons related to optical, mechanical and detector instabilities, Stokes vector measurements can be difficult. The optimal measurement configuration depends on the application.

1.2.3 Polarization modulation with time multiplexing

Polarimetry is performed in a number of ways, each with its own tradeoffs. For solar polarimetry, there is a need to understand the dynamic magnetic activity at small spatial scales in high temperature plasma. High temporal, spatial and spectral resolutions are important to measure these effects. To obtain the highest spatial resolution, solar polarimeters need to sample the full spatial resolution of the diffraction-limited beam delivered by the telescope. Division of field and division of aperture results in a degradation of the diffraction limited performance. Spatial modulation requires different optical paths and thus may make the measurement susceptible to differential gain effects or differential aberrations. Division of wavefront requires splitting the intensity, but each instrument is flux limited and requires all the light in the passband to meet the science requirements. Solar polarimetry investigates phenomena that occur at extremely narrow passbands due to the Doppler motion or intrinsic spectral line width in the plasma. Division of wavelength results in loss of necessary spectral resolution. Ultimately division of time polarimetry provides the best solution given the diffraction limited spatial sampling.

1.2.4 Primary polarization optical components

Custom design optical components are a necessity for polarization modulation and calibration. These primary polarization optical components are located in two areas of the telescope. Figure 1.3 illustrates the optical beam path through the telescope. Polarimeters and their respective polarization modulators are located beyond M9 in the Coudé laboratory. The polarization calibration optics are placed before M3, just above the Gregorian focus. These calibration optics are not in the beam during measurements but can slide in and out of the beam path for calibration procedures. Combinations of these calibration optics provide known polarization states. Ideally, the optimal location of the calibration optics is at the front of the telescope before M1, but due to the limit in current manufacturing capabilities the next best location is near GOS focus. Sections 1.2.4.1 and 1.2.4.2 describe the polarization optics located in these positions respectively.

1.2.4.1 Instrument polarization optics

As mentioned before, four of the first light instruments shown in Figure 1.4 are polarimeters: VTF, ViSP, DL-NIRSP and Cryo-NIRSP. Two primary polarization components within the instruments are the polarization modulator and analyzer. These optical components are designed to modulate and analyze the polarized light respectively. All other optical elements in the instruments, were not designed to induce polarization effects, but are not polarization benign and can alter the polarization state of the beam. Each instrument partner has designed and procured the polarization analyzer. The modulator optical elements are provided by the DKIST team, as are the sensors for each camera. In order for instruments to run simultaneously and perform time multiplexed polarimetry, each instrument modulator and detector must be synchronized. This is one of the main reasons the DKIST team provides these polarization optical components. The other major reason is the project gains efficiency in acquiring these parts and the calibration retarders in one contract. There is also a symbiosis of the designs that is explained further in Section 3.3. Rotating retarder was selected as the polarization modulator component. As the retarder rotates it modulates the incident Stokes parameters in the intensity signal, the light is then incident on the polarization analyzer before being read out by the detector. The signal is integrated over 360° rotation of the retarder by N number of intervals. Data reduction codes demodulate the signal and calculate back the measured Stokes parameters.

There is one exception for the VTF polarimeter; the VTF team will provide its own modulator. As mentioned in Section 1.1.5.2, the VTF has a ferroelectric liquid crystal retarder modulator. For the VTF, a ferroelectric liquid crystal retarder is preferred over a rotating retarder modulator because timing of the instrument doesn’t lend to the continuous modulation of the rotating retarder. The VTF does sudden and fast changes in their interferometer. Therefore, even though there are 4 polarimeters, this dissertation only discusses the 3 modulator components designed, analyzed, and procured by the DKIST team.

1.2.4.2 Polarization calibration optics

The polarization calibration optics input known polarization states to the telescope optical system in order to fit the Mueller matrix model of the telescope at a number of wavelengths and telescope pointing configurations. A linear polarizer provides linearly polarized states by rotating its transmission axis normal to the propagation direction. A quarter wave retarder added after the linear polarizer can generate circularly polarized light when its fast axis is oriented 45° to the transmission axis of the linear polarizer.

In the ideal calibration case, a polarization state generator system is placed at the entrance of the telescope and a polarization state analyzer just before the detector of one of the instruments. Current technological capabilities limit the ability to provide a large enough aperture polarization state generator system, in this case 4-meter diameter. As a result the calibration optics are placed near the Gregorian optical focus of the telescope, where the beam size is smaller and the F-number is slower than at prime focus. This leaves the first and second mirror polarization characterization to other calibration methods not discussed in this dissertation.

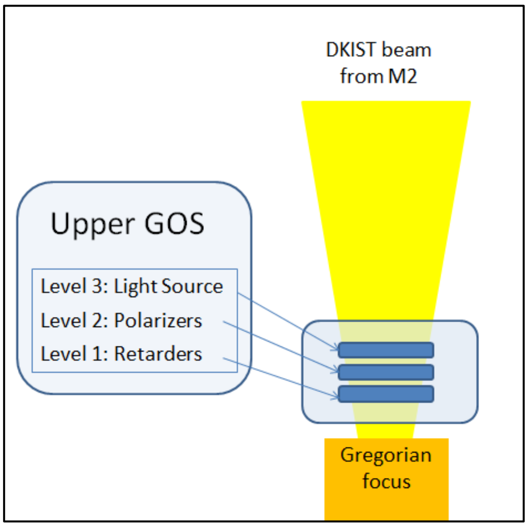

Figure 1.5: F/12.7 light from M2 converging to the Gregorian focus. A box located above the Gregorian focus, named the Upper GOS frame, holds three linear translation stages that move optics in and out of the beam path.

Calibration optical components are located in a large rack attached to the Telescope Mount Assembly (TMA). This subassembly is called the Upper Gregorian Optical System (Upper GOS). The Upper GOS rack contains three levels of horizontal translation stages. Level 3 has a linear stage that will move a broadband light source for alignment as well as for polarization calibration when sunlight is not available. Level 2 has a linear stage that translates a polarization calibration linear polarizer into the beam path. The calibration polarizer sits in a rotation stage. Level 1 holds polarization calibration retarders optimized for different wavelength ranges. Each one sits in a rotation stage (D. Elmore, Ferayorni, Hansen, & Hegwer, 2014). The stage numbering is in ascending order from the Gregorian focus towards the sun as shown in Figure 1.5. Each optical component has the mobility to slide in and out of the telescope optical path.

The calibration optics provide input states to all polarimeters from 380 nm to 5000 nm. A single super achromatic quarter wave retarder design to encompass this entire range is extremely difficult and expensive to manufacture. To reduce cost and risk of building these parts, three individual retarders were designed to cover the full wavelength range. The VTF wavelength range falls entirely within that of the ViSP, so if the ViSP wavelength range is covered, so too is the VTF. Thus, even though there are 4 polarimeters, only 3 calibration retarders were designed. More details are provided about the requirements, design and modeling of the calibration retarders in Chapter 3.

1.2.5 Telescope polarization model

All optical components in the telescope cause some type of polarization effect at DKIST sensitivity levels, and therefore every reflective and transmissive optic impacts the incident Stokes vector that is being measured. Mueller matrices can model these elements to a reasonably high accuracy, and a polarization calibration procedure fits the Muller matrices and in theory removes the polarization effects from the measured signal.

1.2.5.1 Polarized intensity measurement

Essentially, DKIST collects light from the Sun and feeds it to the five instruments. Each polarimeter modulates and analyzes the Stokes vector components into a series of intensity measurements. This telescope/instrument polarization is broken down into a simple model shown in Figure 1.6. Each pixel and wavelength's Stokes vector interacts first with the telescope's Mueller matrix, $\boldsymbol{M_{tel}}$, then the polarimeter's modulation matrix, $\mathbf{W}$, before being read out by a detector as intensity measurements, $\boldsymbol{P_{measured}}$.

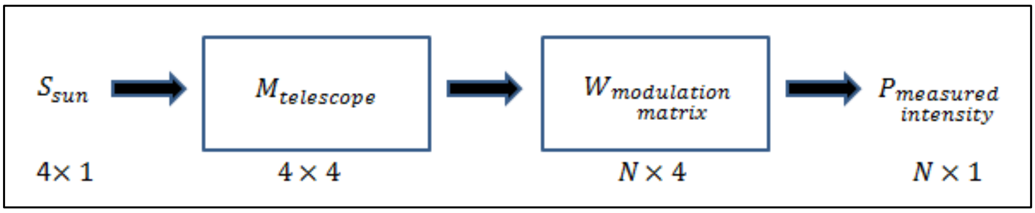

Figure 1.6: The Stokes vector from a point on the Sun passes through the telescope and modulated before being read out by the detector as an intensity signal.

The multiplication of these matrices is given in equation (1.3), where the sequence of light interaction with optical elements results in a multiplication from right to left.

$$\boldsymbol{P_{measured}} = \mathbf{W}.\boldsymbol{M_{tel}}.\boldsymbol{S_{sun}} \tag{1.3}$$

All optical elements after the azimuth rotation are grouped together in $\mathbf{W}$, the modulation matrix. The modulation matrix is not a Mueller matrix, it is an $N\times 4$ array containing N number of analyzer vectors, $\boldsymbol{A(\theta_i)}$ (R. A. Chipman, 1995; del Toro Iniesta & Collados, 2000). The analyzer vector is the first row of the Mueller matrix that represents $\boldsymbol{M_7}$ to the detector for each step of the rotating modulator, $\boldsymbol{M}_{\mathbf{mod}}(\theta_i)$, where θ_i is the ith modulation rotation state of the modulator.

The retarders will sit in a rotation stage and instead of stepping to N states, it will continuously spin during an observation measurement. The number of modulation states N represents the half revolution number of integrated steps. For example, a polarimeter with 8 modulation states means that the instrument is integrating over 8 steps in 180° rotation, or half a revolution. The modulation matrix is given below.

$$\boldsymbol{W} = \begin{pmatrix} \boldsymbol{A(\theta_1)} \\ \boldsymbol{A(\theta_2)} \\ \boldsymbol{A(\theta_3)} \\ \cdot \\ \cdot \\ \cdot \\ \boldsymbol{A(\theta_{N-1})} \\ \boldsymbol{A(\theta_N)} \end{pmatrix} \tag{1.4}$$

The columns of **W** represent the modulation of the Stokes parameters, and equation (1.3) shows that the measured intensity $\boldsymbol{P_{meas}}$ is equal to the modulation matrix **W** multiplied by the telescope matrix $\boldsymbol{M_{tel}}$ and incident Stokes vector $\boldsymbol{S_{Sun}}$.

The measured Stokes vector, $\boldsymbol{S_{meas}}$ is calculated by multiplying the inverse matrices of the modulation matrix and telescope matrix onto the measured intensity vector.

$$\boldsymbol{S_{meas}} = \boldsymbol{M_{tel}^{-1}}.\boldsymbol{W_p^{-1}}.\boldsymbol{P_{meas}} \tag{1.5}$$

The inverse telescope matrix, M_{tel}^{-1}, removes the telescope's polarization signature from the measured Stokes vector. The inverse modulation matrix, $\boldsymbol{W^{-1}}$, also known as the demodulation matrix, converts the intensity measurements into the measured Stokes parameters, S_{meas}. The number of modulation states N must be equal to or greater than 4 to fully recover the Stokes vector. For N greater than 4 the system is overdetermined and the optimum demodulation matrix is the pseudoinverse of the modulation matrix, $\boldsymbol{W_p^{-1}}$. The pseudoinverse is the inverse matrix that provides the least squares estimate for measuring the incident Stokes vector.

$$\boldsymbol{W_p^{-1}} = (\boldsymbol{W^T}.\boldsymbol{W})^{-1}.\boldsymbol{W^T} \tag{1.6}$$

The superscript T represents the transpose of the matrix, and superscript -1 represents the inverse of the matrix.

1.2.5.2 Modeling all optical components

The telescope matrix, $\boldsymbol{M_{tel}}$, is not a static matrix due to the azimuth and elevation rotations of the telescope. In addition the calibration optical element configuration is included in $\boldsymbol{M_{tel}}$. As a starting point, the DKIST team has decided to approximate the behavior of all the telescope optical elements up to the azimuth rotation as a cascaded multiplication shown in equation (1.7). The matrix representations of rotation matrices and calibration components are not static elements and will change depending on the geometry of the telescope or the angle of rotation.

$$\boldsymbol{M}_{\text{tel}} = \boldsymbol{R}_{az}(\boldsymbol{\alpha}).\boldsymbol{M}_6.\boldsymbol{M}_5.\boldsymbol{R}_{el}(\boldsymbol{\vartheta}).\boldsymbol{M}_4.\boldsymbol{M}_3.\boldsymbol{C}_j.\boldsymbol{M}_2.\boldsymbol{M}_1 \tag{1.7}$$

Each mirror element has its own Mueller matrix, where $\boldsymbol{M}_n$ represents the nth mirror. $\boldsymbol{R}_{el}(\boldsymbol{\vartheta})$ and $\boldsymbol{R}_{az}(\boldsymbol{\alpha})$ are matrices that represent the elevation and the Coudé – azimuth rotations respectively. Depending on the time of day and location of the Sun in the sky, ϑ and α rotation angles change. $\boldsymbol{C}_j$ represents the calibration optical configurations located after the second mirror of the telescope allowing characterization from **M3** to the instruments. In the situation where the calibration optics are not in the beam path, $\boldsymbol{C}_j$ is just the identity matrix. The primary and secondary mirror calibration will be performed utilizing either sky polarization or Sun polarization effects such as the correlation method (David F. Elmore, Lin, Socas Navarro, & Jaeggli, 2010).

1.2.5.3 Group model

The Mueller matrices of the telescope optics are grouped together for the optical elements with no change in configuration between them in Elmore's Group model(D F Elmore, 2013). For example, consider a single Mueller matrix $\boldsymbol{X}_{\mathbf{a}}$, where the subscript **a** represents the joined together mirror element numbers. $\boldsymbol{X}_{\mathbf{12}} = \boldsymbol{M}_{\mathbf{2}}.\boldsymbol{M}_{\mathbf{1}}$, $\boldsymbol{X}_{\mathbf{34}} = \boldsymbol{M}_{\mathbf{4}}.\boldsymbol{M}_{\mathbf{3}}$, and $\boldsymbol{X}_{\mathbf{56}} = \boldsymbol{M}_{\mathbf{6}}.\boldsymbol{M}_{\mathbf{5}}$. $\boldsymbol{M}_{tel}$ becomes equation (1.8).

$$\boldsymbol{M}_{tel} = \boldsymbol{R}_{az}(\boldsymbol{\alpha}).\boldsymbol{X}_{\mathbf{56}}.\boldsymbol{R}_{el}(\boldsymbol{\vartheta}).\boldsymbol{X}_{\mathbf{34}}.\boldsymbol{C}_j.\boldsymbol{X}_{\mathbf{12}} \tag{1.8}$$

1.2.5.4 Calibration plan

DKIST Science Working Group and Polarimetry Scientist will determine the best polarization calibration method to use during the operation of the DKIST. The combinations of polarization calibration optics for generating input states are based on a 2013 baseline plan that follows Skumanich et al. The calibration optics have five configurations. First is Clear, where no elements are in the beam; it is represented by the identity matrix. Second is Dark, where the beam is blocked completely. Third is the calibration polarizer only in the beam, $\boldsymbol{M}_{\mathbf{polarizer}}[\boldsymbol{\theta}]$, where the transmission axis will rotate to a number of angles represented by $\boldsymbol{\theta}$. Fourth is the calibration retarder only, $\boldsymbol{M}_{\mathbf{retarder}}[\boldsymbol{\varphi}]$, where the fast axis will rotate to a number of angular positions represented by $\boldsymbol{\varphi}$**.** The fifth configuration is the calibration polarizer followed by the calibration retarder,$\boldsymbol{M}_{\mathbf{retarder}}[\boldsymbol{\varphi}].\boldsymbol{M}_{\mathbf{polarizer}}[\boldsymbol{\theta}]$. $\boldsymbol{\theta}$ and $\boldsymbol{\varphi}$ once again represent rotation angles of the respected components.

Listed below are the configurations represented by $\boldsymbol{C_j}$ from DKIST Report-0055 on the Polarization Calibration Plan by David Elmore:

i. Dark
ii. Clear
iii. Calibration retarder at $0°, 45°, 90°, and\ 135°$
iv. Linear Polarizer at $0°, 45°, 90°,$ and $135°$
v. Calibration linear polarizer at $0°, 45°, 90°, and\ 135°$ followed by a calibration linear retarder at three fast axis orientations relative to the linear polarizer transmission axis orientation, $0°\ and\ \pm 45°$

As mentioned in section 0, the telescope's Mueller matrix $\boldsymbol{M}_{\mathbf{tel}}$ in equation (1.8), excluding $\boldsymbol{X}_{\mathbf{12}}$, and the polarimeter modulation matrix $\boldsymbol{W}$ are characterized with calibration measurements using the configurations of $\boldsymbol{C_j}$ at different telescope geometrical configurations (D F Elmore, 2013).

1.2.6 Conclusion

The DKIST will not only be the largest solar telescope built to date, but also the largest polarimeter. Four of the five first light instruments are polarimeters and will provide vital data to solar scientists in order to better understand the dynamic effects of the Sun. The telescope itself must have a polarization calibration performed on the optical train to determine M_{tel}, as it is important to eliminate polarization effects of the telescope optics and geometrical configurations. The following chapters illustrate the design, fabrication and testing plans for the DKIST retarders.

2 RISK MITIGATION OF MATERIAL BIREFRINGENCE

2.1 Introduction

Due to the extreme conditions of the DKIST telescope system and tight space restrictions, uniaxial crystals were selected as the material of choice for the DKIST calibration and modulator retarder designs. The calibration retarders are located in an F/13 converging beam and exposed to the broad spectral range as transmitted through the atmosphere at Haleakalā. In comparison to other common retarder materials such as polymers and liquid crystals that breakdown when exposed to short wavelengths, birefringent crystal are the only ones that have the ability to withstand the 300-Watt radiant flux experienced by the calibration retarders.

Material candidates were narrowed down to three crystals: Quartz, MgF2 and Sapphire. The materials were chosen based on their birefringence, high transmittance, high damage threshold and low absorption over the wavelength ranges of the DKIST instruments. An uncertainty that posed a large risk in the manufacturing of the retarders was the birefringence dispersion discrepancies in the literature. This section of the dissertation explains the mitigation of this risk with measurements of birefringence performed over the spectrum that the DKIST retarders are required to operate and the evaluation of whether one of the published birefringence functions was valid or whether it required a new birefringence function that fit the measured data over the wavelength of interest.

2.2 Birefringent uniaxial crystal retarders

Retardance produced by a uniaxial crystal depends on a number of factors. First there are the properties of the crystal: The ordinary and extraordinary refractive indices, the orientation of the optic axis with respect to the cut of the crystal (A-cut and C-cut are examples), thickness of the crystal, absorption, stress-optic coefficients, coefficient of thermal expansion, thermo-optic coefficient. It depends on the incident light properties: The wavelength, coherence, angle of incidence, field of view, and polarization of the incident state. Lastly, it depends on the environment: Ambient thermal environment, thermal shifts over time, thermal gradients, mounting, refractive index of the incident and exiting medium.

2.2.1 C-cut and A-cut uniaxial crystals

Uniaxial crystals have a unique axis called the optic axis along which the refractive index is different from the other two orthogonal axes. Two common slicing configurations of uniaxial crystals are the C-cut and A-cut configurations, shown in Figure 2.1. When a crystal is C-cut the optic axis is perpendicular to the face of the crystal. At normal incidence the light propagates along the optic axis, the electric field encounters a single refractive index and therefore the light sees no birefringence. Depending on the angle of incidence, at non-normal incidence small amounts of birefringence is encountered.

When a crystal is A-cut the optic axis lies in the plane of the crystal, perpendicular to the normal incident ray as shown in the figure below. The electric field at normal incidence enters an A-cut crystal and splits into the two orthogonal polarization modes, along the fast and slow axes of the crystal. The propagating wave encounters two different refractive indices, the ordinary and extraordinary refractive index. As the light exits the crystal the beams are superposed, and there is a phase delay in one component with respect to the other called retardance.

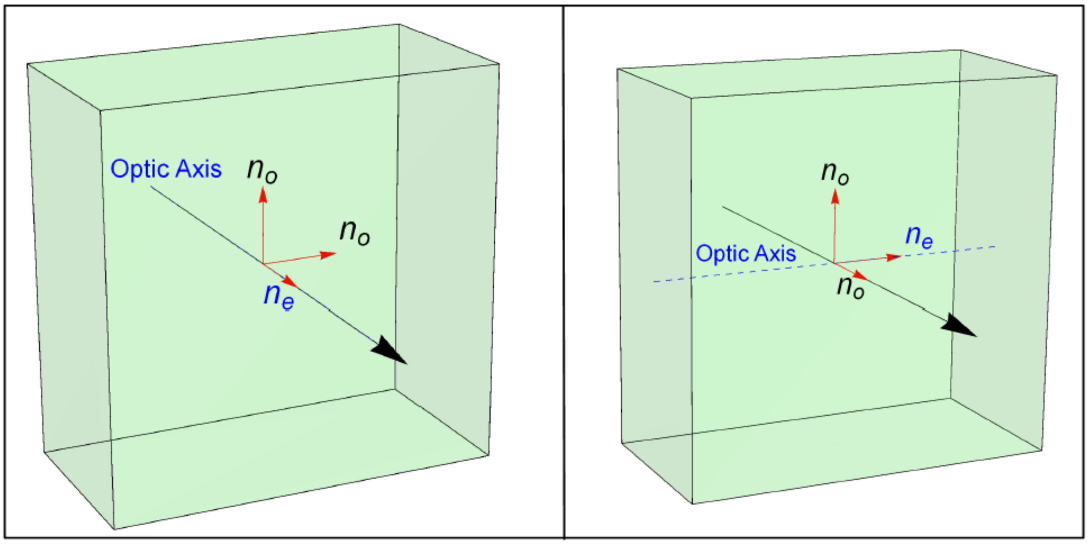

Figure 2.1: Illustrations of a C-cut (left) and a A-cut (right) uniaxial crystal.

There can be both positive and negative uniaxial crystals. Birefringence is the difference between the extraordinary refractive index and the ordinary refractive index. The sign of the birefringence is dependent on whether the ordinary or extraordinary refractive index is larger. If the ordinary refractive index has larger absolute value than the extraordinary refractive index then it is called a negative uniaxial crystal. If the extraordinary refractive index has larger absolute value than the ordinary refractive index then it is called a positive uniaxial crystal. The fast axis is the axis with smaller refractive index. In a positive uniaxial crystal, the fast axis is along the ordinary axis. In a negative uniaxial crystal, the fast axis is along the extraordinary axis.

The polarization of the light exiting an A-cut crystal is highly dependent on the polarization of the incident light and the angle with respect to the fast axis of the crystal. A good visual representation of the behavior of an ideal retarder is on the Poincaré sphere. An ideal retarder has no diattenuation; it purely represents a rotation about the fast axis of the retarder. The starting point of rotation is the input polarization state; the amount of rotation is the magnitude of the retardance in a clockwise direction.

In order to design compound achromatic wave plates, it is vital to know the birefringence as a function of wavelength. Section 2.2.2 explains the risk mitigation measures performed for the DKIST retarder designs. It was necessary to have better confidence in the modeled birefringence functions to create designs that could meet the polarization accuracy goals of the telescope. First, the birefringence functions of crystalline quartz, MgF2 and sapphire in the literature and the discrepancies found among some of the sources is illustrated. Then, birefringence measurements are performed by channeled spectra methods. The measurements were performed over the ultraviolet, visible and near infrared wavelength ranges, and new birefringence functions were created based on these measurements. The new functions are shown with existing functions and published data.

2.2.2 Birefringence of quartz, sapphire, and magnesium fluoride

Over the last century the increased use and interest in understanding crystalline materials resulted in numerous measurements in the literature (Dodge, 1984; Gorachand Ghosh, 1998; Philipp, 1985; Sosman, 1927). In fact, many of the generalized books on optics provide a large amount of information on the optical properties of crystals; OSA Handbook of Optics, American Institute of Physics Handbook, Handbook of Electronic Materials to name a few. Measurements were performed in a number of ways, one method was to measure ordinary and extraordinary refractive indices directly by means of the minimum-deviation method on a precision spectrometer (Dodge, 1984), then the indices were subtracted to get the birefringence. Others used the channeled spectra technique, in which the uniaxial crystal was placed between parallel or crossed polarizers where its crystal axis was aligned 45° with respect to the polarizers transmission axes (Carvalho, 1898; Chandrasekharan & Damany, 1968). It was difficult to determine the most accurate data results from all these publications. Different methods were used at a number of temperatures and some with more accurate measurement techniques than others. Some authors such as Sosman thoroughly described a collection of measured birefringence and refractive index of crystalline quartz, listed them in tables, and compared the accuracy of the results (Sosman, 1927).

This section focuses on three birefringent crystals: quartz, magnesium fluoride, and sapphire. They were selected as candidate materials for the DKIST compound retarders for several reasons. Crystalline quartz and MgF2 comprise majority of the achromatic retarder components in the ultraviolet to near infrared range, due to availability, cost, birefringence not too high or low, and their ability to polish well. Sapphire is the third most commonly used crystal; it has negative birefringence whereas quartz and MgF2 have positive birefringence. The combination of a negative birefringent and positive birefringent crystal can create a retarder with reduced sensitivity to alignment but in general an increased temperature dependence (Hale & Day, 1988). Sapphire crystal has drawbacks that include few commercial sources for A-cut optical wafers and the difficulty to polish due to hardness. In addition, its birefringence spectrum is nearly linearly dependent with MgF2 and crystal quartz, so that sapphire does not substantially open the design space to improve achromaticity. In summary, these three are commonly used materials for crystalline retarders, vendors feel comfortable working with them, transmission is good over the wavelength range of interest and they can be grown to the large diameter required for the DKIST retarders.

In order to design the compound crystalline retarders it was imperative to know the birefringence over the DKIST instrument range of 0.38 to 5 μm. In particular crystalline quartz and sapphire were found to have significant differences between the birefringence functions in the literature. Measurements performed for the three crystals are described in this section. MgF2 had the most consistent values in the literature so measurements were mainly performed as a confidence check that our measurement process was valid. These measured birefringence functions were used in the final DKIST retarder designs.

2.2.2.1 Literature inconsistencies

A literature search showed a number of inconsistencies in the birefringence dispersion functions from various publications(M. Bass, Van Stryland, Williams, & Wolfe, 1995; CVI, 2003; Gorachand Ghosh, 1998). These sources contain tabled properties of optical materials and are used by many in the optics community. In a paper on achromatic athermal retarder fabrication, Mahler showed discrepancies in birefringence and plotted the models and their differences from 0.4 to 0.9 µm (Mahler, McClain, & Chipman, 2011). The inconsistencies resulted in uncertainty in the optical designs that utilized these birefringence functions. There are a number of reasons for the inconsistencies. Some functions were fitted to data sets where the measurements came from separate sources with different measurement techniques. Other functions were extrapolated from measured data where the wavelength ranges of the actual measurements were limited.

2.2.2.1.1 Quartz

Quartz is one of the most widely used uniaxial crystals for retarder design. High transmission from the ultraviolet to the near infrared makes quartz a prime candidate for refractive optical components. Quartz has a Mohs hardness of 7, it is soft enough to polish easily and hard enough that it does not scratch easily. For applications in which thermal fluctuations are expected, the low thermal expansion coefficients benefit designs. With better technology today synthetic quartz crystal is grown to extremely high quality and homogeneity.

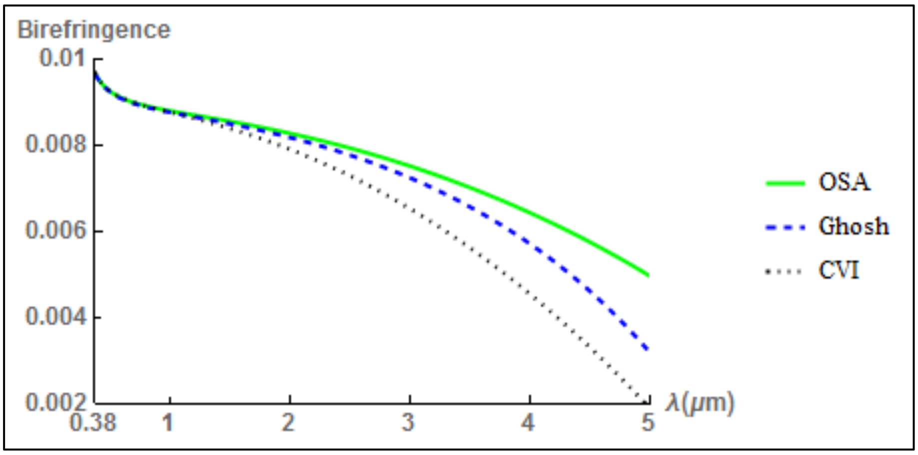

Figure 2.2: Quartz birefringence vs. wavelength extrapolated beyond the measured wavelength range tabled in Table 2.1 from three published sources.

Figure 2.2 shows three birefringence curves, the curves agree well at lower wavelengths but depart drastically in the near infrared. OSA Handbook of Optics (M. Bass et al., 1995) Sellmeier dispersion function for the ordinary and extraordinary refractive indices of quartz comes from a paper by Radhakrishnan (Radhakrishnan, 1951). Refractive index data used to find the coefficients was measured at 18°C from 0.185 to 0.707 µm. The 3rd edition of the Handbook of Optics claims to extend the valid range of this dispersion function to 3 µm even though the data source is still the same.

Gorachand Ghosh wrote a paper on quartz dispersion (Gorachand Ghosh, 1999), it tabled measured ordinary and extraordinary indices of refraction (Gray, 1957) and measured birefringence (Gray, 1957; Hardy & Perrin, 1932; Jenkins & White, 1957). Ghosh formulated what he called a physically meaningful dispersion equation with *select* data points from the above-mentioned sources. He then compared the residual errors from his curve and the data to errors from the function published in the Handbook of Optics (M. Bass, 1995) and the data. This was not an adequate comparison since the data used to fit the Handbook of Optics functions resulted from a different measurement then the ones tabled in this paper.

CVI refractive index data are provided in their catalog but no reference was stated about techniques or sources. The data were measured from 0.193 to 2.010 µm with no temperature range given. Dispersion formulas are of the Laurent series form.

The data cited and used for birefringence curves shown in Figure 2.2 does not extend past 2 µm. Therefore a large discrepancy was observed between the three functions beyond that wavelength. The CVI curve diverges from the other two curves before 2 µm.

Birefringence Equation	**Minimum wavelength (μm)**	**Maximum wavelength (μm)**
OSA Handbook of Optics	0.18	(.707) / 3.0
Ghosh	0.198	2.0531
CVI	0.193	2.010

Table 2.1: Valid wavelength range for each birefringence function source for crystalline quartz. Data for the OSA function only valid to 0.707 µm, but the book tables the maximum wavelength limit as 3.0 µm.

2.2.2.1.2 Sapphire

Sapphire has excellent transmission from 0.2 to 6 µm. It has a Mohs hardness of 9; this is a positive design aspect in terms of strength, but is ultimately more difficult and costly to polish.

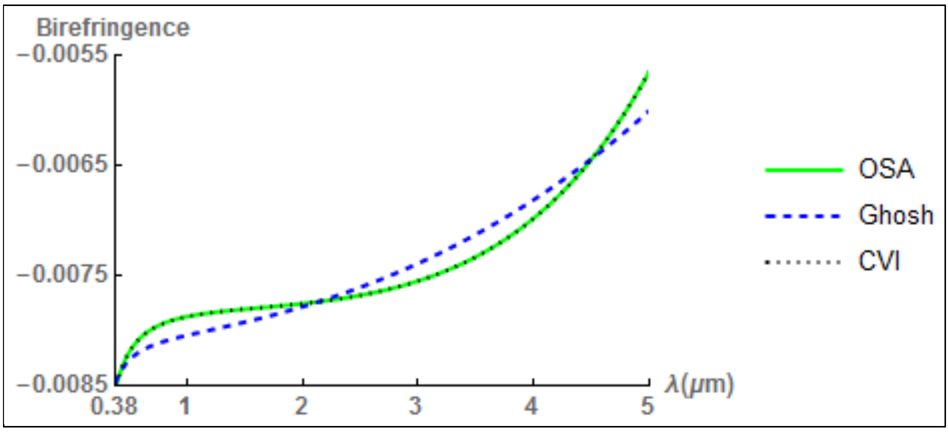

Figure 2.3: Sapphire birefringence vs. wavelength. CVI birefringence is extrapolated from 2.0 µm.

Figure 2.3 plots several published dispersion functions. The CVI curve has a consistent reference to the same set of published data for the OSA Handbook of Optics and Ghosh's Handbook of thermo-optic coefficients. This referenced data cannot be found in the publication cited (Malitson & Dodge, 1972). It is not clear why the Ghosh dispersion does not match OSA since they reference the same data.

CVI refractive index data was provided in their catalog but once again no reference was given. The data was measured from 0.2652 to 2.000 µm with no temperature range provided. CVI Sellmeier coefficients are exactly the same as OSA.

An Applied Optics paper by Chandraskharan and Damany provides birefringence measurements from 0.16144 to 0.32111 µm, but this data was not used in the listed dispersion functions.

Birefringence Equation	**Minimum wavelength (μm)**	**Maximum wavelength (μm)**
OSA Handbook of Optics	0.20	5.5
Ghosh	0.20	5.5
CVI	0.2652	2.0

Table 2.2: Valid wavelength range for each birefringence function source for sapphire.

2.2.2.1.3 Magnesium Fluoride

MgF2 transmission range is by far the most extended of the three crystals, from 0.12 to 7 µm. With a Mohs hardness of 6, it is softer than quartz. Polishing this softer material is more difficult and it is more prone too damage.

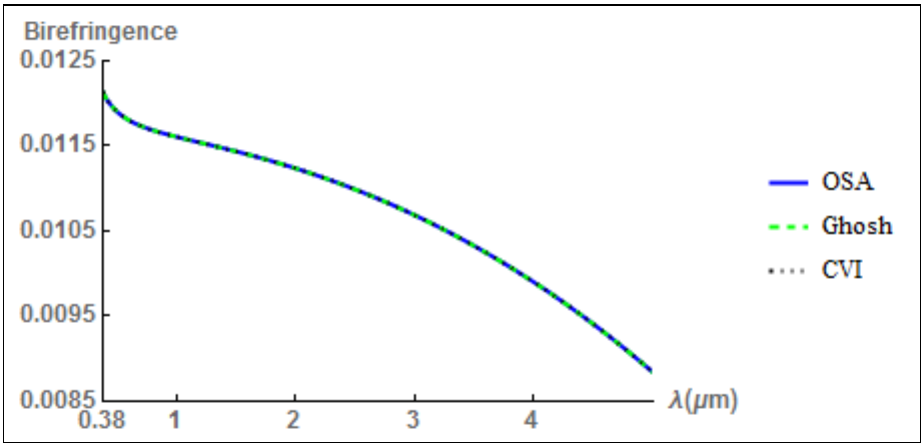

Figure 2.4: MgF2 birefringence vs. wavelength

Data cited by OSA handbook of optics and Ghosh was measured by Dodge (Dodge, 1984) from 0.2 to 7.04 µm at 19°C. Since the data is the same for the two fits it explains why the curves are nearly identical. CVI refractive index data was provided in their catalog but with no reference. Data tabled by CVI was measured from 0.193 to 0.355 µm with no temperature range given. Just as with sapphire, the Sellmeier coefficients are exactly the same as OSA.

Birefringence Equation	**Minimum wavelength (μm)**	**Maximum wavelength (μm)**
OSA Handbook of Optics	0.20	7.04
Ghosh	0.20	7.04
CVI	0.193	0.355

Table 2.3: Valid wavelength range for each birefringence function source for Magnesium Fluoride.

2.2.2.1.4 Conclusion

The birefringence functions of quartz and sapphire were inconsistent among the published sources. As a step toward mitigating the risk of the compound retarder design, measurements were performed on the birefringence of quartz, sapphire and MgF2, shown in the next section.

2.2.2.2 Birefringence measurements of quartz, sapphire and MgF2

The main purpose of these measurements was to mitigate the uncertainty in the birefringence in order to reduce risk in designing compound wave plates for the NSO DKIST calibration and modulation retarders. The primary wavelength range of interest for DKIST instruments is from 0.38 to 5 μm. Two spectrometers were needed to cover this wavelength range, a Varian Cary 5000 for the ultra-violet, visible and near infrared, and a Perkin Elmer 983G for the an extended range in the near infrared. The Nasser Peyghambarian group provided use of a Varian Cary 5000 at the College of Optical Sciences and Optical Data Associates provided the use of a Perkin Elmer 983G.

2.2.2.2.1 Measurement technique

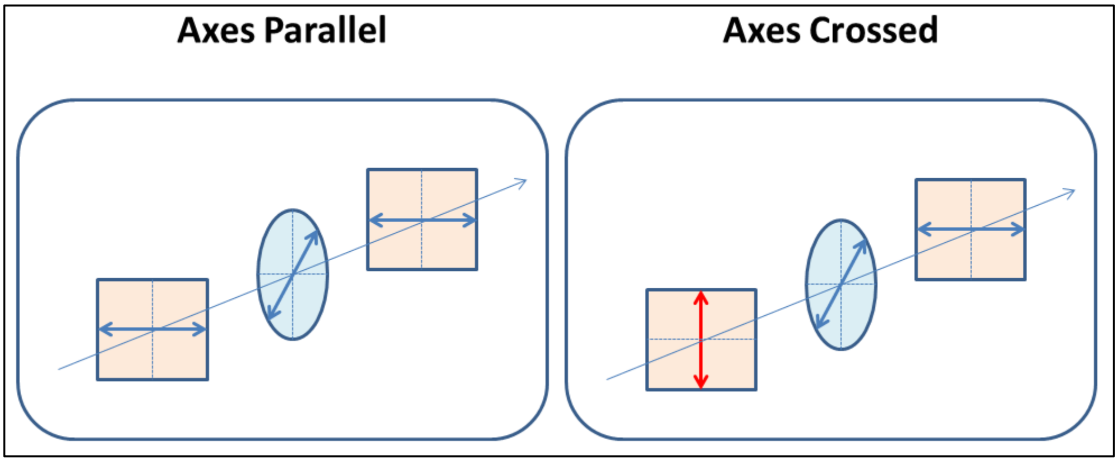

Figure 2.5: Measurement configurations. Arrows represent the transmission axis of the polarizers and optic axis of the retarders.

The retardance of a sample A-cut crystal was measured by placing it between polarizers in the sample compartment of the spectrometer. The first polarizer established the polarization of the light incident on the sample crystal. The second polarizer analyzed how the sample affects the state of polarization of the incident light. To ensure no polarization effects resulted from the spectrometer optics, the analyzer's transmission axis was kept at a fixed orientation. The sample's fast axis was set 45° with respect to the analyzer's transmission axis. Two configurations of the first polarizer were used, parallel and crossed transmission axis with respect to the analyzer.

In the parallel configuration, the transmission through the multi-order waveplate sample is proportional to the cosine squared of the retardance. The period of the sinusoid increases as the wavelength increases. Each period minimum can be approximated by a quadratic function.

$$\mathbf{T} \propto \mathbf{Cos}^{2}[\boldsymbol{\delta}/\mathbf{2}] \tag{2.1}$$

In the crossed configuration, the transmission through the multi-order waveplate sample is proportional to the sine squared of the retardance. The period of the sinusoid also increases as wavelength increases, and the minima are at the same wavelengths of the maxima in the parallel configuration.

$$\mathbf{T} \propto \mathbf{Sin}^{2}[\boldsymbol{\delta}/\mathbf{2}] \tag{2.2}$$

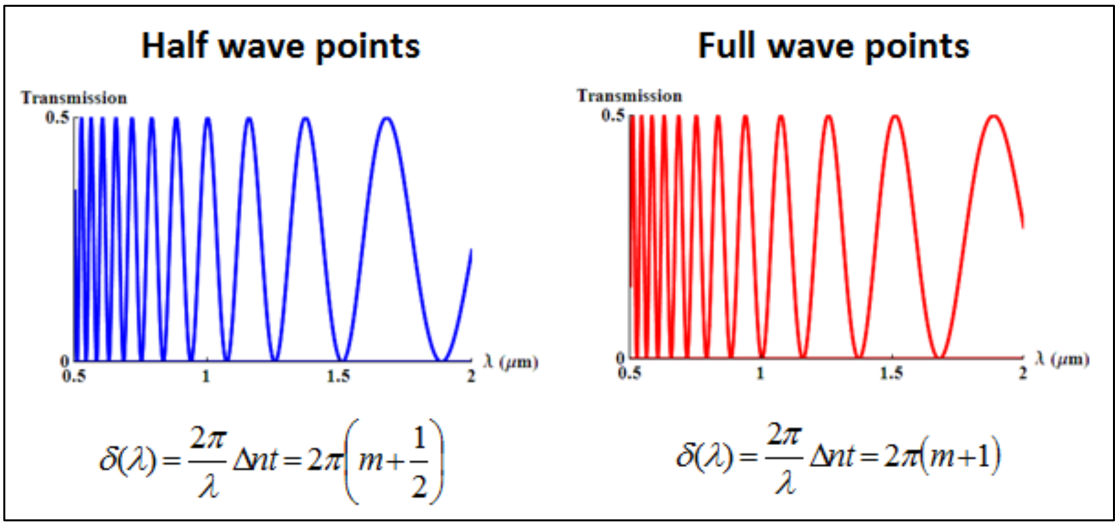

Figure 2.6: Channeled spectra plots, see text for details.

$$\boldsymbol{\delta = 2\pi(m + \varphi)} \tag{2.3}$$

The phase accumulation δ can be represented by 2π radians multiplied by m the integer number of waves of retardance, plus φ the residual phase. Retardance wraps itself between 0 radians and 2π radians as a function of wavelength. The fringes have a longer period as wavelength increases. When $\varphi = 1/2$, the sample plate produces a half wave of retardance, and between parallel polarizers a minimum in the transmission is observed. The wavelengths where the minimum occur are determined and correspond to odd integer numbers of half wavelengths. Likewise for every $\varphi = 0$ the sample periodically becomes a full wave plate, and between crossed polarizers there is a minimum. This is similar to a technique by Fischer et al., measuring the birefringence of ZnGeP2. Birefringence was solved for at the measurement wavelengths of full and half wave point minima.

2.2.2.2.2 Sample Setup

Table 2.4 gives the thickness of our crystalline quartz, sapphire and MgF2 samples. Each is about an inch in diameter and cut as an A-plate. The thicknesses were measured at Idex Corporation Precision Photonics at the specified temperatures. Two Ultra Broad Band (UBB) wire grid polarizers from Edmund Optics Inc. were mounted in the spectrometer oriented such that the fast axis was 45° with respect to the polarizer's transmission axes. All three components were mounted in PRM1 Thorlab rotation mounts, with 5 arc minute resolution.

Crystal	**Measured Thickness (μm)**	**Temperature (C)**
Quartz	1000.3±0.2	22
Sapphire	771.3±0.2	22
MgF2	1324.64±0.07	23.8

Table 2.4: Thickness of sample A-cut crystal plates for birefringence measurements. Thickness was measured at the corresponding tabled temperatures.

A polarizer and sample fixture was constructed to fit in the sample compartment of the spectrometers on a short rail to keep them aligned parallel with the beam. The sample remained stationary as the spectrometer scanned through wavelength. Due to the significant drop off of wire grid transmission around 4.7 μm the wave points were not measured out to the desired 5 μm. Ideally wire grids with transmission that extend beyond 5 μm would provide the best data for fitting the dispersion functions up to that wavelength. Ambient temperatures were monitored carefully throughout the data acquisition and are listed in Table 2.5.

Crystal	**Cary Temperature (C)**	**Temperature shift (C)**
Quartz	21.7	5.8
Sapphire	20.3	7.2
MgF2	22.78	4.7

Table 2.5: Table of measured temperature for Cary data and the difference from the Perkin Elmer temperature.

The polarizers were placed in two configurations, parallel and crossed transmission axes. A dark measurement was performed when the beam was blocked in the sample compartment while measuring the spectra. A clear reference (100% transmission) was measured with the wire grids in the beam path and the sample removed. The dark was subtracted from the clear and sample measurements, and the sample measurement was divided by the clear to normalize the data. Polarization artifacts from the spectrograph's input beam optics could have resulted when the input side polarizer was rotated from parallel to crossed. However, this does not affect the location of the minima with respect to wavelength and therefore only the minima were fit.

2.2.2.2.3 Fitting minima to get wave points

The measured wavelength and normalized intensity values were imported into Mathematica and a quadratic fit of the minima was performed. The approximate wavelength where the minimum would occur was calculated using the measured thickness and one of the published birefringence functions. These predicted wave points were used to define the range of wavelengths about the minimum used for the parabolic fit.

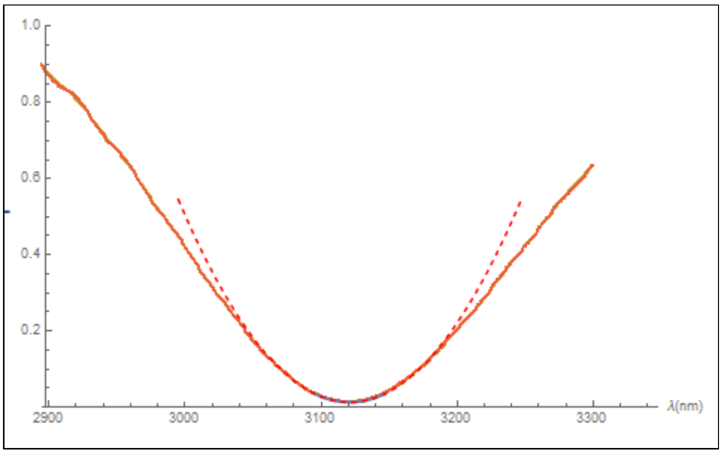

Figure 2.7: Blue curve near the minimum is the parabolic fit over the ±25 μm range of a minimum in the normalized intensity data. Red Dashed curve is the extension of this fitted parabola. Orange data points are the measured data to show the quadratic fit to the minimum method.

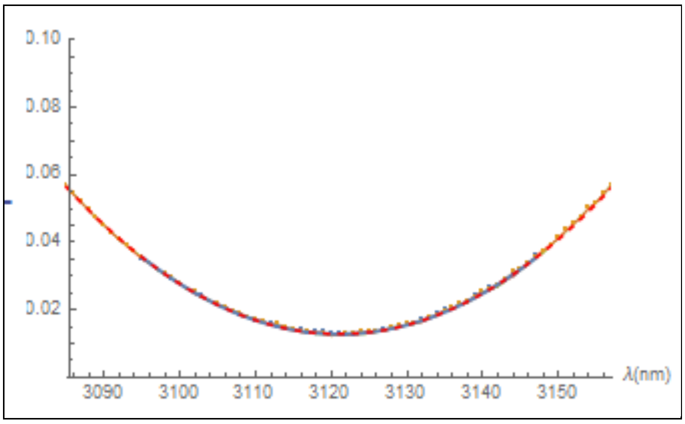

Figure 2.8: Magnified the minimum to view the quadratic fit.

Blue points in Figure 2.9 are the fit residuals from the data points. Note the horizontal scale is different. 150 fit residuals from the red curve fit subtracted from the measured orange data points in Figure 2.8.

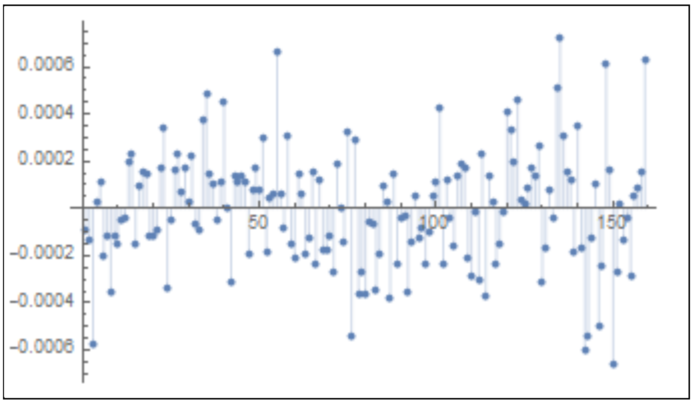

Figure 2.9: Residuals computed as data minus model fit of the data points with the quadratic function fit.

2.2.2.2.4 Finding the uncertainty range of the wave point

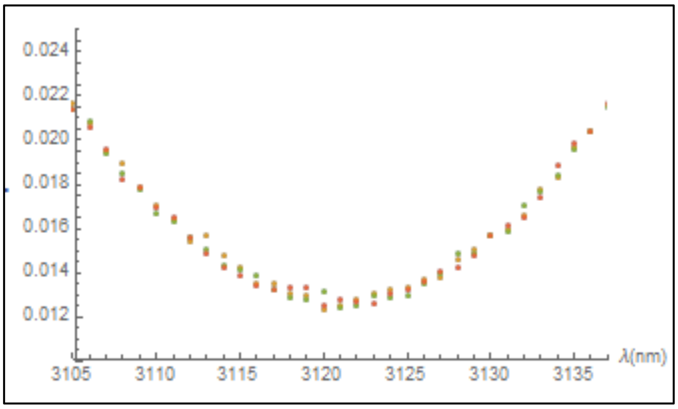

Figure 2.10: Plot of a wave point at 3121nm.

Mathematica fit function on average found the minimum within better than half a wavelength sample spacing, this resulted in an uncertainty of 0.05 nm or better.

The wave point order numbers and the wavelengths they were measured at were tabled for a given thickness and temperature of the measured crystal. Retardance as a function of wavelength, λ, birefringence, Δn, and thickness, t, is

$$\boldsymbol{\delta = \frac{2\pi\Delta n t}{\lambda}}. \tag{2.4}$$

Equating equation (2.3) to equation (2.4) results in the function below. It solves for birefringence using the order number, residual phase and thickness.

$$\boldsymbol{\Delta n = \frac{(m+\varphi)\lambda}{t}} \tag{2.5}$$

$\boldsymbol{\varphi}$ is 0 or ½ for full wave and half wave points respectively. The column with Cary measurement temperatures in Table 2.5 designates the nominal temperature for the birefringence data measured with the Cary spectrometer.

2.2.2.2.5 Converting infrared data to the Cary 5000 temperature with a shift

Data measured by the Perkin Elmer spectrometer is also in Table 2.5, and is higher than the temperature of the Cary spectrometer measurements. In order to combine the data from the two instruments, the current retardance equation had to be dependent on temperature shift. To make it temperature dependent a thermal component was added to equation (2.4). The thermal component is the partial derivative of the retardance with respect to temperature multiplied by the temperature shift. $\frac{d\delta}{dT}$ is shown below in equation (2.6).

$$\boldsymbol{\frac{d\delta}{dT} = \frac{2\pi}{\lambda}\Delta n t\left[\frac{1}{t}\frac{dt}{dT} + \frac{1}{\Delta n}\frac{d\Delta n}{dT}\right]} \tag{2.6}$$

The thickness t is dependent on temperature because of thermal expansion of the crystal characterized by the thermal expansion coefficient α.

$$\boldsymbol{\alpha = \frac{1}{t}\frac{dt}{dT}} \tag{2.7}$$

The thermal expansion coefficient parallel to crystal axis differs from the coefficient normal to it. The coefficient used in this analysis was the α that corresponded to the ordinary refractive index. This is because the crystals measured were cut in an A plate configuration, so incident light propagation direction is perpendicular to the crystal axis. In other words, the thermal expansion that affects the thickness of the crystal plate is the one associated with the ordinary refractive index.

Birefringence is a temperature dependent property of uniaxial crystals because the indexes of refraction of the ordinary and extraordinary axes are dependent on temperature. Coefficients for a functional form of $2n_e\frac{dn_e}{dT}$ and $2n_o\frac{dn_o}{dT}$ were computed by Ghosh from published experimental data (Gorachand Ghosh, 1998). This information was used to substitute into $\frac{d\Delta n}{dT}$.

$$\boldsymbol{\frac{d\Delta n}{dT} = \frac{dn_e}{dT} - \frac{dn_o}{dT}} \tag{2.8}$$

The thermal shift component was added and the retardance equation was extended as shown below.

$$\boldsymbol{\delta = \frac{2\pi}{\lambda}\Delta n t\left(1 + \left[\alpha + \frac{1}{\Delta n}\frac{d\Delta n}{dT}\right]\Delta T\right)} \tag{2.9}$$

Solving equation (2.9) for birefringence results in equation (2.10).

$$\boldsymbol{\Delta n = \frac{\frac{m\lambda + \varphi}{t} - \frac{d\Delta n}{dT}\Delta T}{1 + \alpha\Delta T}} \tag{2.10}$$

The birefringence of the Perkin Elmer measurements was shifted to be at the same nominal temperature as the Cary measurements. Thus, all the birefringence data from both spectrometers was fit to a single function for the same temperature. Another reason the birefringence spectrum from the Perkin Elmer data was shifted to the Cary measurement temperature was because the temperature of the Cary measurements was closer to the most common measurement temperatures in the literature ($18 - 22°\mathrm{C}$).

2.2.2.2.6 Fit coefficients for birefringence function

Birefringence spectral data from each of the three crystals were fit to Sellmeier birefringence function by nonlinear optimization, based on a technique by Ghosh that he used for ZnGeP2 birefringence fit (G Ghosh, 1998).

$$\boldsymbol{\Delta n} = \frac{\mathbf{1}}{\boldsymbol{n_e + n_o}}\left[(\boldsymbol{A_e - A_o}) + \frac{(\boldsymbol{B_e - B_o})\boldsymbol{\lambda}^2}{\boldsymbol{\lambda}^2 - \boldsymbol{C}} + \frac{(\boldsymbol{D_e - D_o})\boldsymbol{\lambda}^2}{\boldsymbol{\lambda}^2 - \boldsymbol{F}}\right] \tag{2.11}$$

Where $\mathrm{A_e, A_o, B_e, B_o, C, D_e, D_o,}$ and F are the Sellmeier coefficients used in the dispersion equations of the refractive indices of the crystal. The nonlinear optimization algorithm required initial values that were close to the optimized values. The coefficients used as initial values were obtained from The Handbook of Thermo-Optic Coefficients. The nonlinear optimization yielded coefficients for birefringence H, I, G, J and L. The birefringence function is expressed as

$$\boldsymbol{\Delta n} = \boldsymbol{H} + \frac{\boldsymbol{I\lambda}^2}{\boldsymbol{\lambda}^2 - \boldsymbol{G}} + \frac{\boldsymbol{J\lambda}^2}{\boldsymbol{\lambda}^2 - \boldsymbol{L}}, \tag{2.12}$$

and the fitted coefficients are tabled below.

Crystals	**H** $(\times 10^{-3})$	**I** $(\times 10^{-3})$	**G** $(\times 10^{-3})$	**J** $(\times 10^{-3})$	**L**	**RMSD** $(\times 10^{-6})$
Quartz	0.61339	8.2187	13.476	13.644	82.208	0.9871
Sapphire	1.8299	-9.6436	10.432	-0.38758	21.660	4.640
MgF2	-19.364	30.992	2.3253	40.060	388.37	1.512

Table 2.6: Sellmeier coefficients that resulted from fitting the measured wave points for the birefringence functions of quartz, sapphire and MgF2.

2.2.2.2.7 Plot comparison of published curves and measured data and fit curve

Plots similar to figures (2.2), (2.3), and (2.4) are shown below. Both measured data and NSO fitted birefringence curve are plotted with the published curves. Fit residuals are also plotted for each crystal. All the previously published curves are shown in black, the NSO curve is in red. For quartz, the Ghosh curve has the closest birefringence dispersion of the three published curves. For sapphire, the OSA and CVI curves nearly overlap the measured data, the Ghosh curve had a very different functional form. Finally the MgF2 curves show an overall match in the published curves and the data to an order of magnitude of 5×10^{-6}.

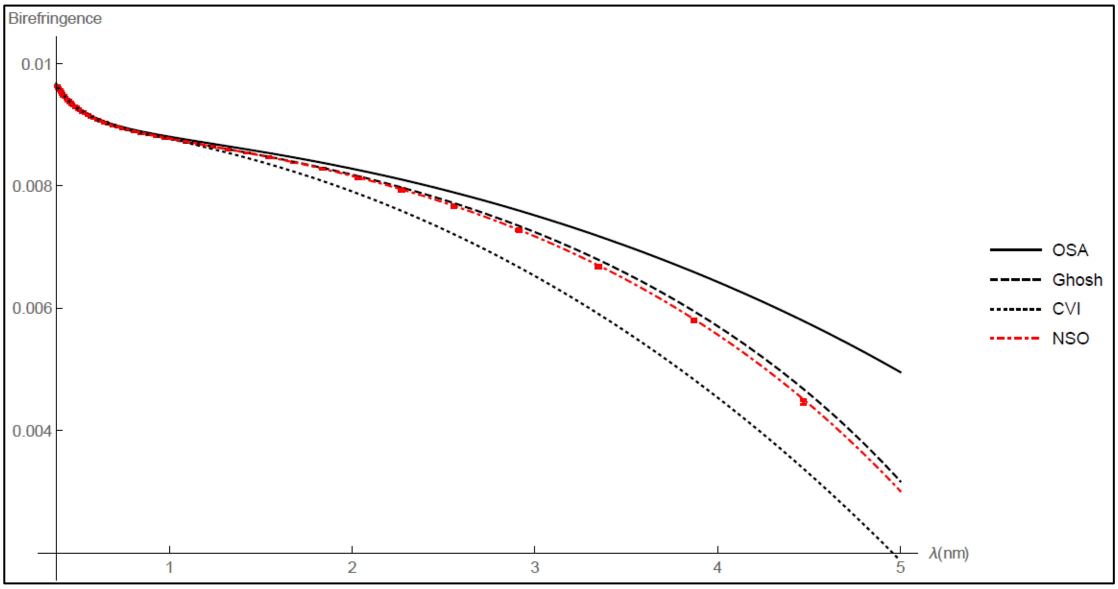

Figure 2.11: Quartz birefringence curves and measured data with errors plotted.

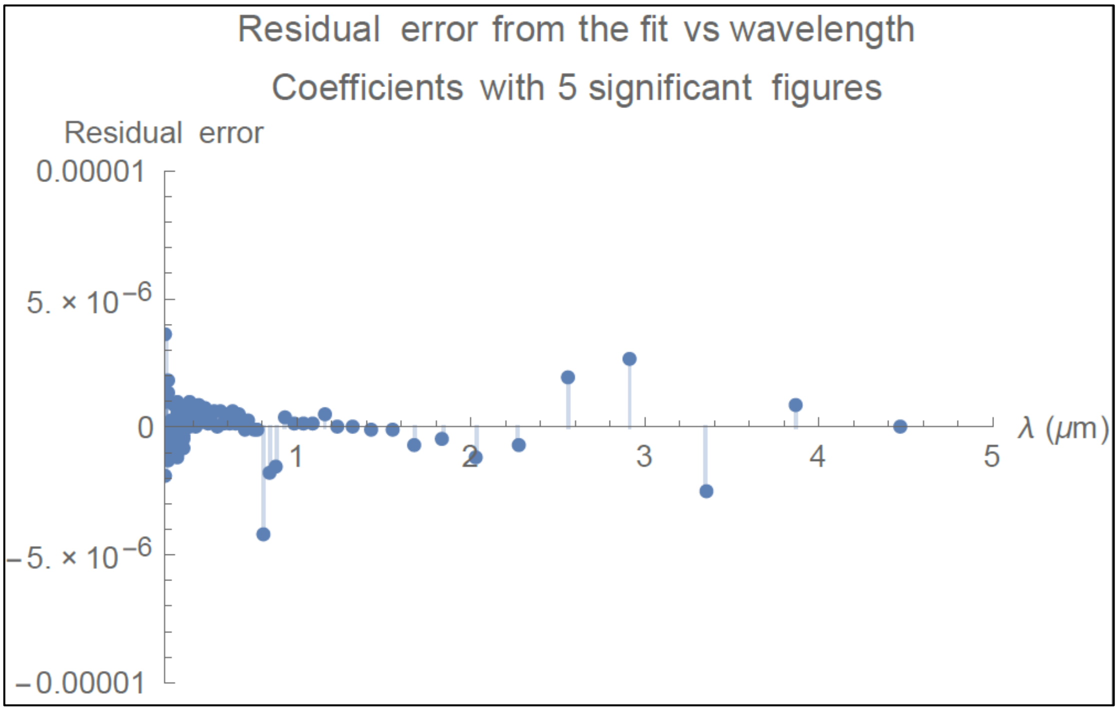

Figure 2.12: Quartz birefringence fit error.

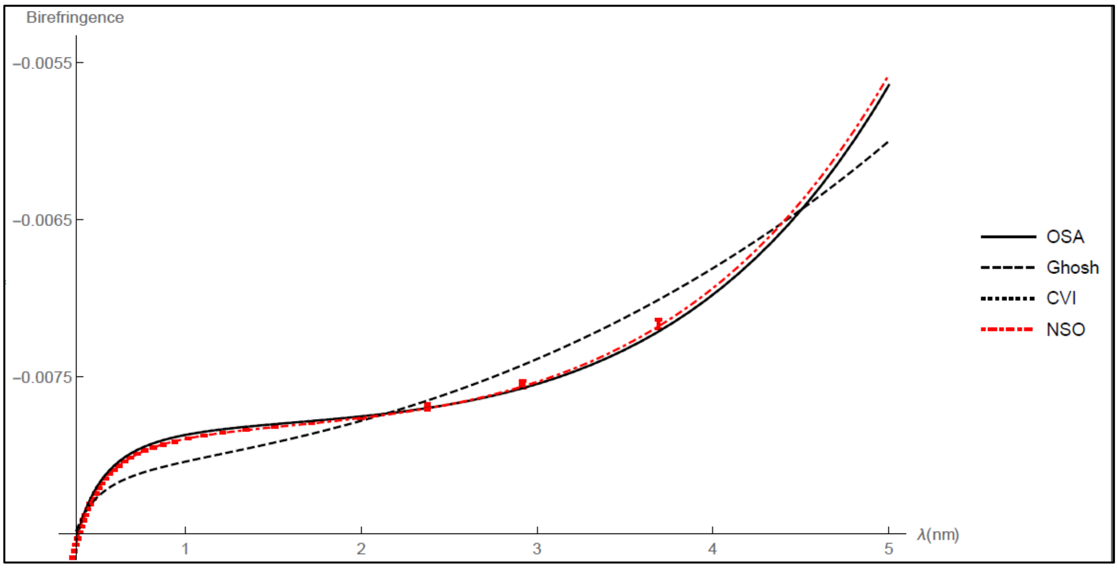

Figure 2.13: Sapphire birefringence curves and measured data with errors plotted.

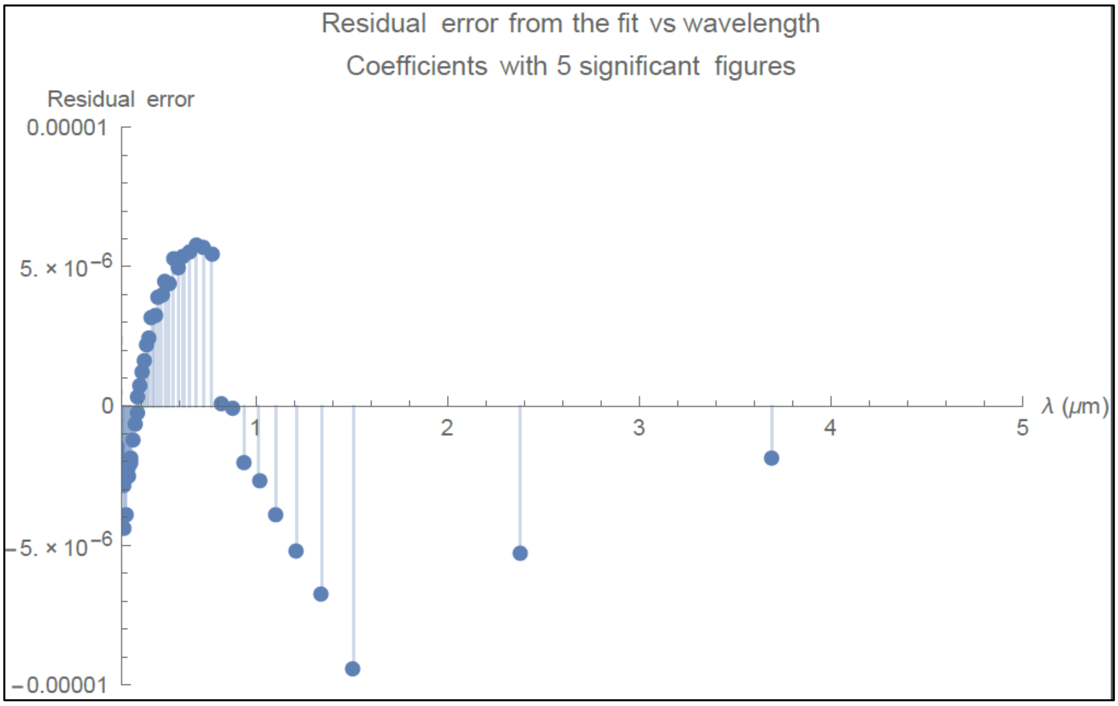

Figure 2.14: Sapphire birefringence fit error. There is a clear functional dependence with wavelength that is not captured by the Sellmeier formula, however these errors are at the 5x10^-6 level and are far below the amplitude necessary to perform a reasonable optical design. Furthermore sapphire was too costly to implement so further investigation was not performed.

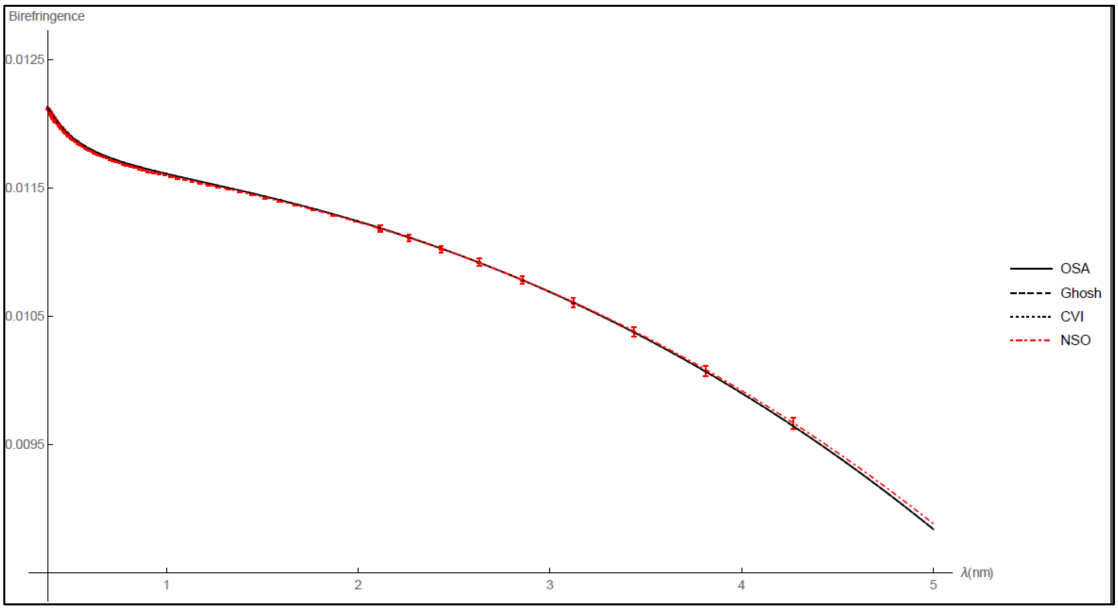

Figure 2.15: MgF2 birefringence curves and measured data with errors plotted. Published curves and measured data consistency provided confidence in the measurement technique.

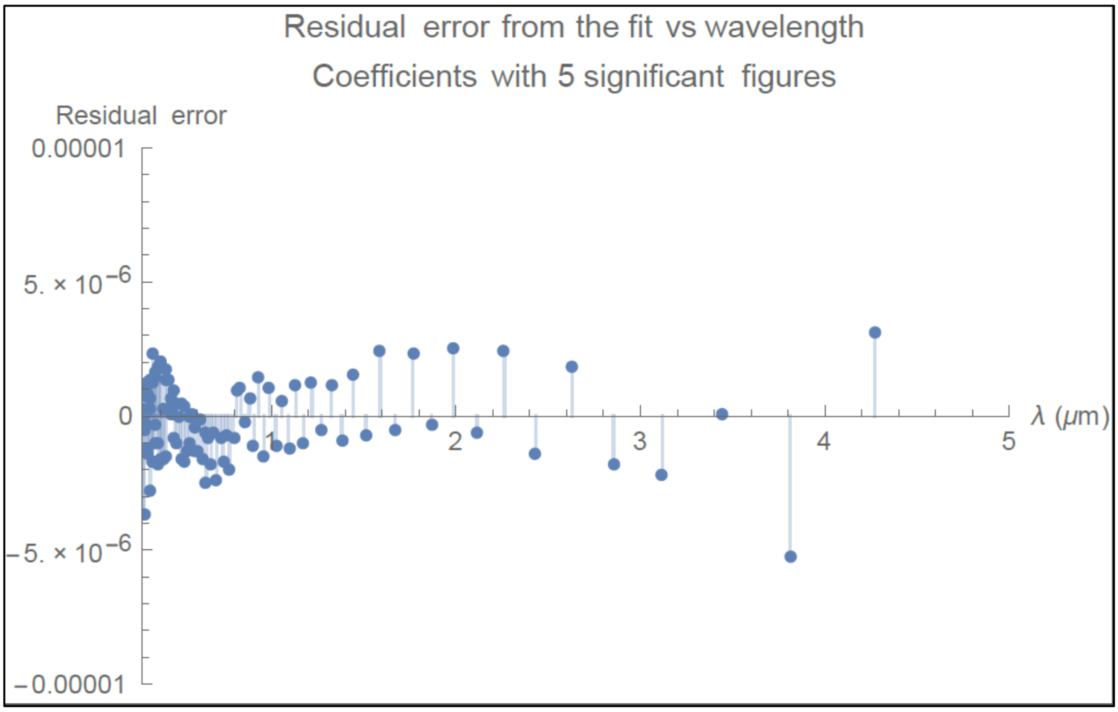

Figure 2.16: MgF2 birefringence fit error.

2.2.2.2.8 Error analysis

Error bars in the preceding figures were calculated from the uncertainties in wavelength, thickness and temperature. The root sum squared of the errors due to wavelength, thickness and temperature were used to achieve the total uncertainty in the birefringence.

$$\Delta(\Delta n)^2 = \frac{\partial^2 \Delta n}{\partial \lambda^2}\Delta\lambda^2 + \frac{\partial^2 \Delta n}{\partial t^2}\Delta t^2 + \frac{\partial^2 \Delta n}{\partial T^2}\Delta \mathrm{T}^2 \tag{2.13}$$

Equation (2.13) was rewritten as

$$\begin{aligned}\Delta(\Delta n)^2 &= \left(\frac{\Delta n(\lambda+\Delta\lambda)-\Delta n(\lambda)}{\Delta\lambda}\right)^2 \Delta\lambda^2 \\ &+ \left(\frac{\Delta n(t+\Delta t)-\Delta n(t)}{\Delta t}\right)^2 \Delta t^2 \\ &+ \left(\frac{\Delta n(T+\Delta T)-\Delta n(T)}{\Delta T}\right)^2 \Delta \mathrm{T}^2\end{aligned} \tag{2.14}$$

The final error in the birefringence was calculated as

$$\begin{aligned}\Delta(\Delta n)^2 &= \big(\Delta n(\lambda+\Delta\lambda)-\Delta n(\lambda)\big)^2 + \big(\Delta n(t+\Delta t)-\Delta n(t)\big)^2 \\ &+ \big(\Delta n(T+\Delta T)-\Delta n(T)\big)^2\end{aligned} \tag{2.15}$$

$\Delta\lambda$ was determined from two sources of uncertainty: spectral resolution of the spectrometer and the error in determining the wave points. Spectral bandwidth (SBW) determines the spectral resolution of the spectrometer. The SBW was a parameter set before each data run, it was determined by the width of the light at half peak height exiting the monochromator. In other words, it adjusts the physical width of the entrance and exit slits of the monochromator and the dispersion of the grating.

$$\Delta\lambda = \sqrt{\Delta\lambda_{wave\,point}{}^2 + \Delta\lambda_{spectrometer\,resolution}{}^2} \tag{2.16}$$

Spectral Bandwidth (SBW): There were concerns about the setup accuracy and measurement feasibility at short wavelengths given the equipment limitations. Tests for the optimum spectral bandwidth setting were performed to ensure quality fits. At the shorter wavelengths, the sample points were tightly spaced. Better spectral resolution plays a big factor in the ability to discern the minima with the fitting technique. With a fixed interval size of 1 nanometer, scans were run at several SBW values to demonstrate the detected intensity variation. As seen in Figure 2.17, the reduced SBW from 2 nm to 0.04 nm resulted in better resolution of the wave points. Decreasing the SBW reduced the SNR due to the physically smaller slit widths and the increase in spectral resolution was needed for determining the minima. For the Quartz and Sapphire measurements and SBW of 0.04nm was used.

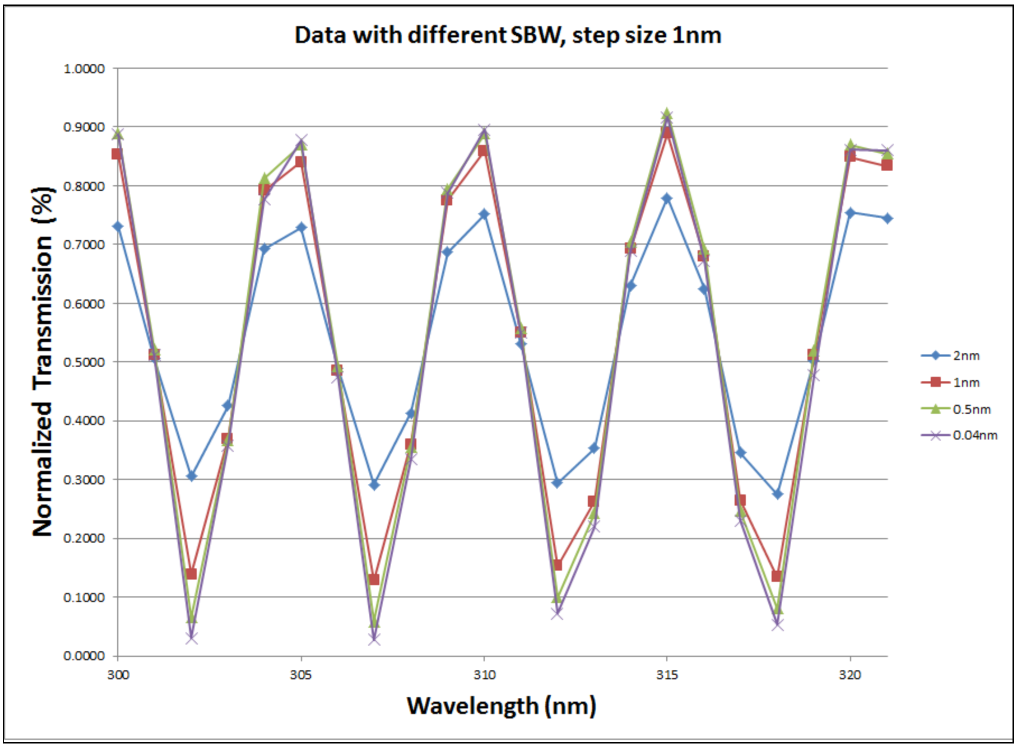

Figure 2.17: SBW comparison of several wave points in the short wavelength region.

Interval size: With a fixed SBW of 0.04 nm scans were performed with step sizes of 0.25, 0.5 and 1 nm. Increased step size at the lower wavelengths increased the number of points available to fit the minima. At higher wavelengths it was not as useful because the minima were so much broader and there were enough points with just the 1 nm step size. The downfall of using smaller steps is the increase in time to complete a measurement. Therefore, measurements were performed in two separate scans, only using the smaller step size in the region where the minimum needed the additional sampling to be resolved. Between 200 and 800 nm a 0.25 nm step size was used, and 1 nm step size for the spectral range 700 to 3300 nm.

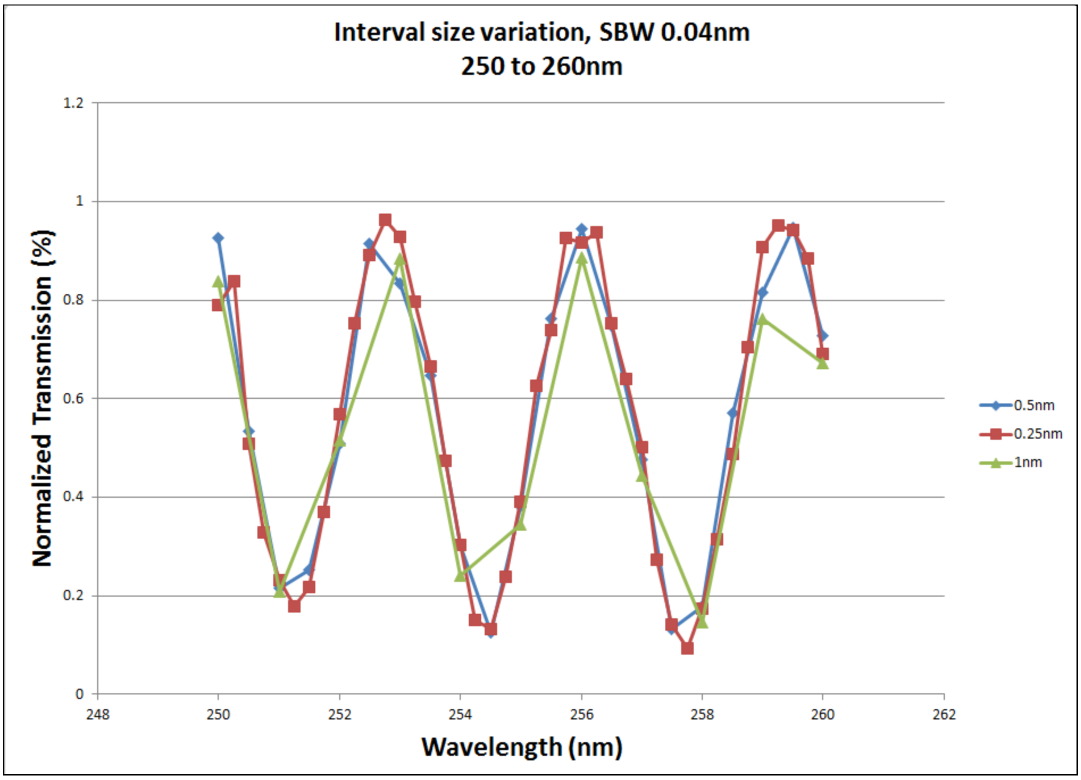

Figure 2.18: Interval size comparison between 250 and 260 nm shows how the minimum is under-sampled using a 1 nm step size, but better resolved with 0.5 nm or even better 0.25 nm.

2.3 Conclusion

Crystalline quartz, sapphire and magnesium fluoride were determined as the best candidate materials for the DKIST retarder designs. It was discovered early on in the project that there was a risk in the design effort due to the uncertainty in the birefringence of these crystals because of inconsistencies in the literature. Sample crystals of precision measured thickness were procured and wave point measurements were performed to determine the birefringence dispersion over the DKIST retarder design wavelength range. The measured data was fit to a Sellmeier function and plotted against published curves. The measurements led to the elimination of dispersion curves that did not follow the form of the measured data. In the end, the NSO functions were used in the DKIST retarder designs discussed in the next chapter.

3 DKIST RETARDERS

3.1 Introduction

Two types of retarders are discussed in this chapter, modulator and calibration retarders. Each polarimeter in DKIST relies on the ability of the modulator retarder in conjunction with a polarization analyzer to encode the polarization signal in the intensity signal read out by the detectors. M_{tel}, the telescope's Mueller matrix contributes polarization errors into the measured signal. Accurate calibration is necessary to remove these polarization effects from the measured signal. Polarization calibration should be located as close to the front of the telescope as possible to characterize as many of the telescope optics as possible. Since the primary and secondary mirrors are large, it is not feasible to illuminate routinely with a calibration system.

This chapter focuses on the design simulation and performance challenges faced prior to fabrication of the DKIST retarders (David F. Elmore, Sueoka, & Casini, 2014). Section 3.2 discusses the requirements that drove the design of the DKIST retarders. Section 3.3 describes the final selected retarder designs and the fabrication requirements.

3.2 Requirements

Section 3.2.1 describes the requirements for the preliminary design of the modulator and calibration retarders derived from top-level science requirements. Sections 3.2.2 and 3.2.3 explain requirements related to the modulator and calibration retarders respectively.

3.2.1 Design requirements

The DKIST Polarimetry Analysis and Calibration Design Requirements Document, PA&C DRD, is driven by the top-level science requirements of the telescope. The DKIST Science Requirements Document (SRD) contains the observational requirements that drive the design requirements and design goals for the telescope and instruments (T. Rimmele, 2005). The telescope must perform precision polarimetry at high spatial resolution. Polarization sensitivity needs to be less than 1×10^{-5}. This is the amount of fractional polarization that can be detected above a constant background and it is limited by photon noise. Polarization accuracy needs to be less than 5×10^{-4}, which is the absolute error in measured fractional polarization. The PA&C DRD provides all instrument requirements for the preliminary design of the modulator and calibration retarders (D. Elmore et al., 2014).

3.2.1.1 Transmitted Wavefront Error and Beam Deflection

The retarder is a polarization optical component that induces a phase delay but does not change the shape of the wavefront. Therefore, retarders are typically flat optical components, with a planar face perpendicular to the incident wavefront propagation direction. In order to prevent wave aberrations and preserve image quality, the project has a transmitted wavefront error (TWE) requirement. TWE requirement for each of the retarders is listed in Table 3.1. It is given in peak to valley, with power removed, at 633 nm (D. Elmore et al., 2014).

Beam deflection requirements for all calibration retarder components must be met so that the light beam does not vignette on any optic following the calibration retarder (David F. Elmore, Sueoka, et al., 2014). Maximum beam deflection specification for the modulators constrains its contribution to image motion on the sensor. The modulator position is either just before the instruments or integral parts of the instruments. Therefore, tighter requirements were given to the modulators than the calibration retarders because they have to comply with the instrument beam deflection internal requirements. The specification comes from the DKIST documents that outline performance requirements derived elsewhere. Table 3.1 displays the maximum beam deflection allowed for each retarder.

Instrument	**Retarder**	**TWE**	**Beam Deflection**
ViSP	Modulator	3 waves	< 90 arc seconds
	Calibration	3 waves	< 96 arc seconds
DL-NIRSP	Modulator	3 waves	< 84 arc seconds
	Calibration	3 waves	< 96 arc seconds
Cryo-NIRSP	Modulator	2 waves	< 10 arc seconds
	Calibration	3 waves	< 96 arc seconds

Table 3.1: Transmitted Wavefront Error and Beam Deflection.

3.2.1.2 Transmission and retarder performance wavelength range

The DKIST retarders are required to have low absorption and high transmission over 0.38 µm to 5 µm. The four polarimeter's wavelength ranges are shown in Table 3.2. In parenthesis are the goal wavelengths where it is desired to expand the wavelength range beyond the required range. The VTF operates within the wavelength range of the ViSP and can use the same calibration retarder because its calibration can be performed simultaneously with the ViSP. The DL-NIRSP retarder originally was designed from 0.5 µm to 2.5 µm, however due to limitations of other optical components in its system, the final maximum wavelength was reduced to 1.8 µm, and 2.5 µm became a goal.

Instrument	**ViSP**	**VTF**	**DL-NIRSP**	**Cryo-NIRSP**
Wavelength range (μm)	0.38-0.9(1.6)	0.52-0.86	0.5-1.8(2.5)	(0.5)1.0-5.0

Table 3.2 DKIST instrument wavelength ranges, goal wavelength in parenthesis. Retarders must have high transmission over these spectral ranges.

3.2.1.3 Diameter

The location of the calibration retarders and modulators in the DKIST optical path determined the diameter of these optical elements. The calibration retarders are located in the upper GOS frame at Level 1, 350 mm above the F/12.7 Gregorian focus. The 5 arc-minute field of view is passed through the heat stop; it requires a clear aperture of 105 mm on the calibration retarder. Modulators are located at the instruments and span the field of view of each instrument. For Cryo-NIRSP the field of view is 5 arc-minutes, ViSP and DL-NIRSP its 2.8 arc-minutes. Table 3.3 lists the required clear aperture and physical diameter of each instrument.

Large diameter retarders are manufactured as custom order options, but most vendors can't and don't fabricate retarders larger than 50 mm. The physical diameter needed for these components is nearly five times the size of a conventional 25.4 mm diameter retarder. Prior to fabrication, Meadowlark Optics, the vendor of choice for these retarders explained that fabrication efficiency would increase by using a common diameter for all retarders. Therefore, a 120 mm diameter was selected for all retarder components.

Instrument	**Retarder**	**Clear Aperture**	**Physical Diameter**
ViSP	Modulator	$\geq 90\ mm$	$\geq 95\ mm, \leq 125\ mm$
	Calibration	$\geq 105\ mm$	$\geq 110\ mm, \leq 125\ mm$
DL-NIRSP	Modulator	$\geq 81\ mm$	$\geq 86\ mm, \leq 125\ mm$
	Calibration	$\geq 105\ mm$	$\geq 110\ mm, \leq 125\ mm$
Cryo-NIRSP	Modulator	$\geq 105\ mm$	$\geq 110\ mm, \leq 125\ mm$
	Calibration	$\geq 105\ mm$	$\geq 110\ mm, \leq 125\ mm$

Table 3.3: Clear aperture and physical diameter specifications of the retarders.

3.2.1.4 Durability/Heat and absorption

Retarders are one of a few telescope optical components that are transmissive. This makes them more susceptible to heating due to absorption. Calibration retarders located near the Gregorian focus must withstand an incident solar radiant flux of approximately 293 Watts. Modulators in the Coudé laboratory experience a reduced solar radiant flux. The ViSP and DL-NIRSP modulators are located after the deformable mirror and will have a reduced FOV of 2.8 arc minutes. The solar radiant flux is less than 74 Watts. The ViSP modulator is located behind the instrument's slit, and that further reduces the incident flux on the retarder. The Cryo-NIRSP modulator is before M_{10}, the deformable mirror, so it sees the transmission of 270-Watts times the transmission of $M_3$to M_9. Cryo-NIRSP receives the entire 5 arc-minute FOV.

Polymer and liquid crystal type materials experience UV darkening and other damage from heating. They do not withstand the solar beam well and has been a long-standing problem for solar telescopes to date.

3.2.1.5 Thermal stability

Calibration retarders are located in the Upper GOS frame housed in the telescope dome. Therefore, these optics are more susceptible to thermal variations of the mountaintop. The ambient temperature for the telescope on Haleakalā is 10°C with a ±12°C expected variation. The calibration retarders incur some bulk heating due to absorption from the solar radiant flux. The shifts in ambient temperature can also destabilize the temperature of the calibration retarder during operation. Thus, for the final retarder design it is important to understand the change in polarization performance of the calibration retarder due to thermal changes in the retarder component.

Modulators are located in the Coudé laboratory where they are isolated from environmental thermal effects. The laboratory environment will be controlled to 20°C±0.25°C. Similar to the calibration retarders, modulator will also incur some bulk heating due to the solar flux incident. The difference though, is that the modulator is in the beam continuously.

3.2.1.6 Rotation rate

In order to perform the time multiplexed polarimetry the polarization modulators are expected to rotate continuously during operation. The modulators reside in a rotation stage and are capable of rotating at a remotely definable, stable speed, up to at least 5 Hz or 300 RPM (D. Elmore et al., 2014). Rotation rate also depends on the instrument. VTF and ViSP require the detectors to measure 30 frames per second with a 4k x 4k detector. ViSP can run at a faster rate when using a reduced spectral range to focus on a particular region of interest. DL-NIRSP detector will run at 30 Hz frame rate, Cryo-NIRSP detector is expected to have a full frame readout time <100ms and a 10Hz frame rate.

3.2.2 Modulator

Each polarimeter has its own continuously rotating modulator optic. The ViSP, DL-NIRSP and Cryo-NIRSP modulators are designed for each polarimeter wavelength range, given in Table 3.2. It is the instrument team that has the final decision on the actual location of the modulator optic, whether it lies in front of the polarimeter or if it is integrated into the instrument beam path. The requirements for the modulator optic and optimization metric are explained in this section.

3.2.2.1 Modulator retardance optimization

For a Stokes vector measuring system, a Polarization State Analyzer (PSA) consists of components that modulate and analyze the polarization signal. For a polarization characterization system, such as a rotating retarder Stokes polarimeter, a retarder sits in front of a fixed linear polarizer and as the retarder rotates it modulates the incident Stokes parameters into a time-varying intensity signal which is later converted back by a data reduction process. Retarders can be optimized to modulate particular Stokes parameters. 180° retardance provides the maximum modulation for linear Stokes parameters, Q and U. 90° retardance provides the maximum modulation for circular Stokes parameter, V. An optimum solution to modulating Stokes Q, U and V is a linear retardance of 132°. However, this type of design restricts the design space to linear retarders. By relaxing this design constraint and allowing for circular retardance, an elliptical retarder solution that modulates the Stokes Q, U and V parameters efficiently while minimizing the measurement uncertainties can be determined.

3.2.2.2 Optimum modulation efficiency metric

In Chapter 1 the optimum demodulation matrix discussed is the pseudo inverse of the modulation matrix. Solar scientists discuss optimization of modulator design to improve the polarimetric accuracy (de Wijn, Tomczyk, Casini, & Nelson, 2011; del Toro Iniesta & Collados, 2000; Snik et al., 2012; Tomczyk, Casini, de Wijn, & Nelson, 2010). Del Toro Iniesta and Collados describe the modulation efficiency metric to optimize the modulation of all the Stokes parameters while minimizing the uncertainties and errors due to noise. If the measured intensity has the same uncertainty $\boldsymbol{\sigma}$, such as due to photon noise, then the error propagation into the calculated Stokes vector can be minimized if the sum of squares of the rows of the demodulation matrix are minimized. The variance $\boldsymbol{\sigma_i}^{\mathbf{2}}$ for each Stokes parameter $i = I, Q, U, V$, is dependent on the number of measurements *n*. $\boldsymbol{W_p^{-1}}$ in del Toro Iniesta's paper is denoted $\boldsymbol{D}$.

$$\boldsymbol{\sigma_i}^{\mathbf{2}} = \boldsymbol{\sigma}^{\mathbf{2}} \sum_{j=1}^{n} \left(\boldsymbol{W_p^{-1}}\right)_{ij}^{\;2} \tag{3.1}$$

Modulation schemes with different number of measurements cannot be compared when using the variance $\boldsymbol{\sigma_i}^{\mathbf{2}}$. However, by normalizing the variances shown in equation (3.2) it is possible to compare modulation schemes.

$$\boldsymbol{\bar{\sigma}_i}^{\mathbf{2}} = \boldsymbol{n\sigma}^{\mathbf{2}} \sum_{j=1}^{n} \left(\boldsymbol{W_p^{-1}}\right)_{ij}^{\;2} = \frac{\boldsymbol{\sigma}^{\mathbf{2}}}{\boldsymbol{\epsilon_i}^{\mathbf{2}}} \tag{3.2}$$

The modulation efficiency $\boldsymbol{\epsilon_i}$ is a factor in the normalized variance that is used to compare the modulation schemes. Equation (3.3) shows efficiency is inversely proportional to variance of the Stokes parameters.

$$\boldsymbol{\epsilon_i}^{\mathbf{2}} = \frac{\boldsymbol{\sigma}^{\mathbf{2}}}{\boldsymbol{n\sigma_i}^{\mathbf{2}}} \tag{3.3}$$

Thus, by maximizing $\boldsymbol{\epsilon_i}$, the variance is minimized. $\boldsymbol{\epsilon_i}$ is the modulation efficiency metric given in equation (3.4), it will be used to optimize the modulator retarder design.

$$\boldsymbol{\epsilon_i = \left(n \sum_{j=1}^{n} \left(W_p^{-1}\right)_{ij}^{2} \right)^{-1/2}} \tag{3.4}$$

Del Toro Iniesta shows that the maximum efficiencies are

$$\boldsymbol{\epsilon_1 \leq 1, \sum_{i=2}^{4} \epsilon_i^{2} \leq 1} \tag{3.5}$$

The maximum efficiency ϵ_I is 1, and to maximize the efficiencies for Q, U, and V the root sum of squares of ϵ_Q, ϵ_U *and* ϵ_V is equal to 1. This results in the efficiencies ϵ_Q, ϵ_U, *and* ϵ_V equal to 0.577.

3.2.2.3 Modulation efficiency specification for DKIST modulators

The efficiencies were maximized over the wavelength range of each of the ViSP, DL-NIRSP and Cryo-NIRSP polarimeters. It is impossible to achieve the theoretical maximum when optimizing the modulation efficiency over such broad spectral ranges. Therefore, the DKIST retarders required an average polarization modulation efficiency greater than 90% of the theoretical maximum for a balanced Q, U, and V polarimeter, using a continuously integrated 10 state polarization as required by the instrument design. DKIST retarders also required the minimum efficiency greater than 80% of the theoretical maximum for any wavelength within the range of a modulator,. These requirements came from the DKIST project's Polarization Analysis & Calibration Specification document. In summary, the design criteria for modulation efficiencies, $\epsilon_{I,Q,U,V}$, was an average $\epsilon_i > 0.9\times0.577\ (0.52)$, and a minimum $\epsilon_i > 0.8\times0.577\ (0.46)$.

3.2.3 Calibration retarders

The ViSP, VTF, DL-NIRSP and Cryo-NIRSP are polarimeters that map the solar disk and the corona. The telescope produces polarization artifacts, and these artifacts need to be calibrated out. The calibration polarizer and retarder act as a polarization state generator, creating known polarization states. The parameters that fit Mueller matrix of the telescope group model are determined through this calibration process, excluding X_{12}. Parameters of the $\boldsymbol{C_j}$, $\boldsymbol{X_{34}}$, $\boldsymbol{X_{56}}$, and $\boldsymbol{W}$ matrices are fit with the calibration procedure. This section will explain the requirements of the calibration retarder.

3.2.3.1 Retardance specification for DKIST calibration retarders

DKIST project specified that the calibration retarder must be achromatic over the wavelength range of the instruments. Ideal retardance of 90°, but has an allowable range of 90°±30°. In order to measure the telescope's polarization signature, known input polarization states are created using two polarization calibration optical elements: a linear polarizer and a linear retarder. The DKIST design requirements documentation calibration retarders specify that the calibration retarder needs to be a linear retarder with a retardation at any wavelength within its range of $(2N+1)\times\frac{1}{4}waves \pm 0.33\times\frac{1}{4}wave$, where N is a non-negative integer. This is simplified to the linear retardance must be within 33% of a quarter wave.

$$\boldsymbol{\delta = 90° \pm 30°} \tag{3.6}$$

Multiple order solutions (N>1) were avoided due to its inherent increased sensitivity to incidence angle. This sensitivity is modeled later in Section 4.3.1.5.2.

3.3 Retarder design

Several retarder types were initially investigated in the design concepts of the DKIST modulator and calibration retarders, they are listed below.

i. Polymer type retarders work great as achromatic, large aperture retarders, but are susceptible to damage by the strong solar irradiance. In particular, these retarders would not survive at the GOS with solar flux of 293 Watts.

ii. Liquid crystal variable retarders perform well as retarders but are not achromatic enough for DKIST instruments, degrade with UV irradiation, and have low thermal stability. Modulators must be polychromatic, (provide high polarimetric efficiency) over the instrument wavelength range. Liquid crystals tend to only be achromatic over a few hundred nanometers, not broadband enough. There are instruments such as FIRS at the Dunn Solar Telescope that divide the spectrum to separate arms, each with its own nematic liquid crystal retarder that tunes retardation to operate for a particular wavelength. If the wavelength range is short enough a single ferroelectric crystal modulator (with fixed waveplates) can cover the wavelength range. An example of this is the Casini polarimeter at the Dunn Solar Telescope. It has 3 passbands, 587, 854, and 1083 nm. Nematic liquid crystal retarders up to this date have not been fast enough.

iii. Retarders made of crystalline material are the most durable and can be stacked in series to produce the desired retarder performance.

3.3.1.1 Pancharatnam-like retarder design

The DKIST modulator and calibration retarders are a Pancharatnam-like design created by Roberto Casini at the High Altitude Observatory and David Elmore of the National Solar Observatory (David F. Elmore, Sueoka, et al., 2014). Pancharatnam described an achromatic wave plate design with three plates of the same birefringent material (Pancharatnam, S. (Raman Research Institute, 1955). The first and last retarders had the same retardance and parallel fast axes. The middle plate fast axis was at an angle χ with retardance π. Discussed in the next two sections are the design steps of the DKIST retarders.

3.3.1.2 Birefringent crystal material

Quartz and MgF2 are more commonly used material for waveplate fabrication than sapphire. Quartz has a even larger fabrication advantage over MgF2 due to it’s hardness and raw material availability. Quartz crystal was the most suitable material for the ViSP and DL-NIRSP retarders because it is highly transmissive in the UV, visible and near infrared range. The Cryo-NIRSP retarder must have high transmission out to 5 µm, MgF2 crystal satisfied this wavelength range.

The designs utilized crystal plates of the same thickness in both calibration and modulator retarders and resulted in a cost saving measure for the retarders made of quartz. The quartz plates are polished in batches of 5. The Cryo-NIRSP retarders were designed with MgF2. For MgF2, the plates were polished one at a time so there was no advantage to use the same thickness for plates in the calibration retarder or modulator designs.

3.3.2 Modulator

The design goal of the modulators followed that described by Tomczyk et al, to achieve highest modulation efficiency of the Stokes parameters over the wavelength range of the instrument (Tomczyk et al., 2010). Tomczyk emphasizes that it is a “polychromatic” rather than an “achromatic” retarder which produces the best polarimetric efficiency. Polychromatic means the retardance does not have to stay constant over the wavelength range, but should have a polarimetric efficiency that is maximized over the polarimeter’s spectrum. This design type is called a Poly-Chromatic Modulator, or PCM for short.

The initial design utilized three crystal plates, quartz for ViSP and DL-NIRSP and MgF2 for Cryo-NIRSP. The degrees of freedom were the two angles between the fast axes of the plates and two thicknesses. The thicknesses of the first and last plate were equal.

The individual plate thicknesses for the DL-NIRSP calibration retarder were around 70 µm for the outer two plates, and 48 µm for the middle plate. These thicknesses were already below the lower limit of most retarder vendor capability to confidently polish even for a 25.4 mm diameter retarder. It was even more unfeasible in our case due to the 120 mm physical diameter of the plate. The aspect ratio would have been on the order of 10^3.

3.3.2.1 Pancharatnam design with zero-order pairs

To ensure the plates were thick enough to be manufactured with confidence by the vendor, they had to be at least 2 mm thick. The 2 mm thickness is equivalent to roughly 30 waves of retardance for quartz crystal. Pairs of thicker crystals can be sandwiched together with their fast axis 90° apart to achieve a total zero-order retardance by subtracting the individual retardance of the plates. Thus, two plates with thicknesses near 2 mm were used in subtraction to generate the desired retardance.

This modified design now consists of 6 crystal plates, grouped into three zero-order pairs. In the end each plate was around 2 mm thick, leading to an aspect ratio of 60 to 1. That’s 30 times smaller, and although still fairly high, this was something accepted by the vendor as a much less risky design. Following are tables of the design thicknesses and orientations for all 3 PCMs.

Thickness (mm)	**Retardance (waves@633.443nm)**	**Fast axis orientation (°)**
2.1324	30.476	0.00
2.0991	30.000	90.00
2.1221	30.328	41.18
2.0991	30.000	131.18
2.1324	30.476	148.23
2.0991	30.000	58.23

Table 3.4: ViSP PCM design thickness, retardance and fast axis orientation.

Thickness (mm)	**Retardance (waves@633.443nm)**	**Fast axis orientation (°)**
2. 1691	31.000	0.00
2.0991	30.000	90.00
2. 1469	30.683	42.20
2.0991	30.000	132.20
2. 1691	31.000	152.51
2.0991	30.000	62.51

Table 3.5: DL-NIRSP PCM design thickness, retardance and fast axis orientation.

Thickness (mm)	Retardance (waves@633.443nm)	Fast axis orientation (°)
2.25500	41.893	0.000
2.15311	40.000	90.000
2.22211	41.282	71.864
2.15311	40.000	161.864
2.25500	41.893	30.390
2.15311	40.000	120.390

Table 3.6: Cryo-NIRSP PCM design thickness, retardance and fast axis orientation.

Tabled above are the design values for thickness, retardance and fast axis orientation for each plate. Physical thickness measurements for transparent substrates are difficult to accurately determine. Instead, the project provided the vendor with a retardance specification at two wavelengths that are measureable. One thing to note from the tables above is that the thicknesses of the subtraction plates of each pair were the same for all quartz elements.

3.3.2.2 Substrate support

To avoid the risk of the plates warping (potato chip effect) the crystal plates were sandwiched between two 10 mm thick window plates of isotropic material. In the end the total retarder compound thickness was around 32 mm, resulting in a 4 to 1 aspect ratio as shown in Figure 3.1. Infrasil glass was used for the ViSP and DL-NIRSP retarders because of its high transmission from 380 nm to 2500 nm. The Cryo-NIRSP used calcium fluoride crystal instead because it has high transmission from 1 to 5 μm.

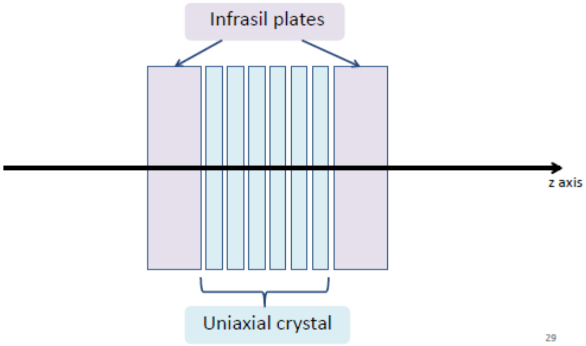

Figure 3.1: Crystalline stack between two thick substrates are shown. Substrates provide support to the thin crystal stack.

3.3.2.3 Bonding method

Instead of adhesive or non-contact bonding techniques, an index matching oil proprietary to the vendor with minimal absorption from the solar flux was chosen.

3.3.2.4 Designed PCM Mueller matrices

The Mueller matrices of the PCM designs over each instrument operation range are plotted below. Modeling of the designed retarder Mueller matrices was an important tool utilized in the acceptance test plan explained in Chapter 6.

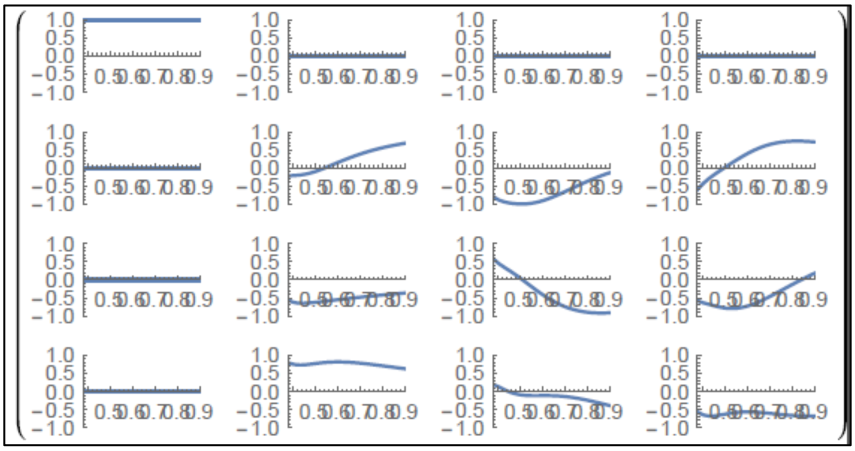

Figure 3.2: ViSP PCM Mueller matrix from 0.38 μm to 0.9 μm.

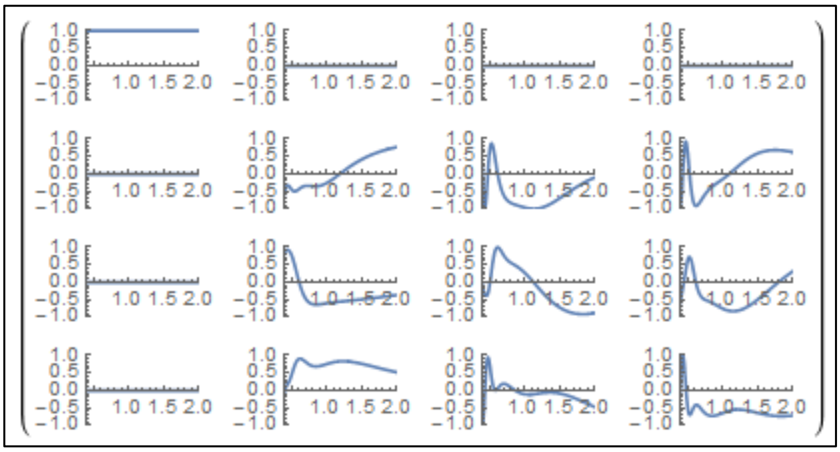

Figure 3.3: DL-NIRSP PCM Mueller from matrix 0.5 μm to 2.5 μm.

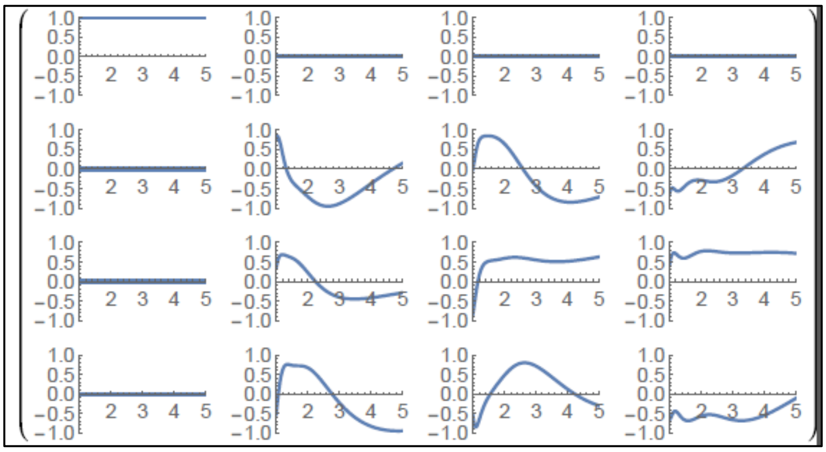

Figure 3.4: Cryo-NIRSP PCM Mueller matrix from 1 μm to 5 μm.

3.3.2.5 Expected modulation efficiency

The modulation efficiencies of the PCM designs over each instrument operation range are plotted below. These efficiencies were calculated for continuously rotating modulators, integrated over 10 modulation states per modulation cycle. Modeling the design modulation efficiencies was another important tool utilized in the acceptance test plan explained in Chapter 6.

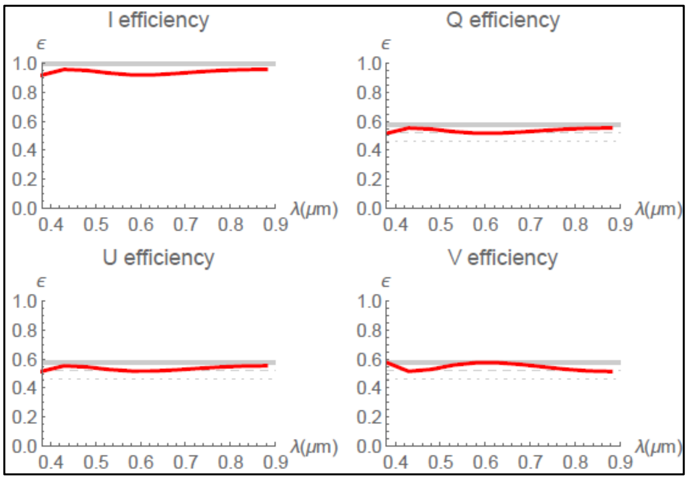

Figure 3.5: ViSP PCM modulation efficiency from 0.38 μm to 0.9 μm.

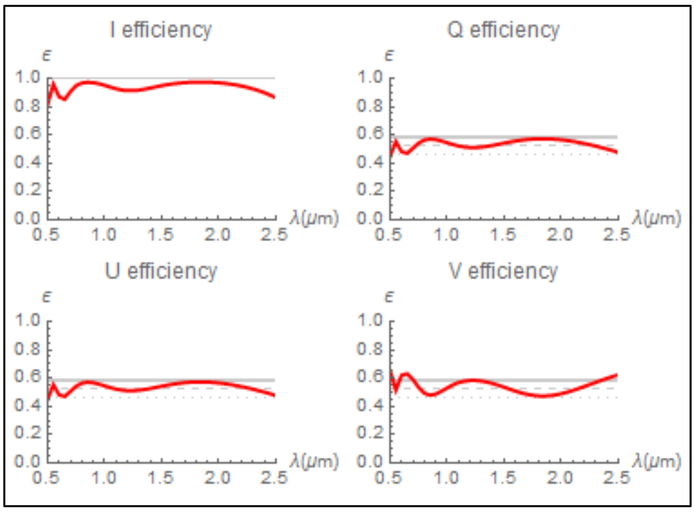

Figure 3.6: DL-NIRSP PCM modulation efficiency from 0.5 μm to 2.5 μm.

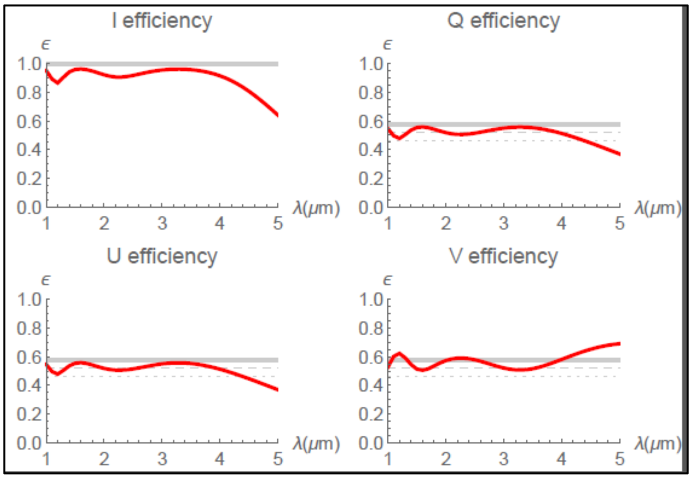

Figure 3.7: Cryo-NIRSP PCM modulation efficiency from 1 μm to 5 μm.

3.3.3 Calibration retarder: The Super Achromatic Retarder (SAR)

The calibration retarders are Super Achromatic Retarders and will be referred to as SARs. To clarify between an achromatic retarder and a SAR, an achromatic retarder refers to a retarder that has been optimized for two wavelengths to yield the same target retardance. The addition of “super” means the retardance has been optimized over the entire wavelength range of operation.

Similar to the PCMs, the calibration retarder designs were also Pancharatnam-like retarder designs. The two outer plates had the same thickness and were parallel to one another. Also, the same substrate support and bonding methods were performed. Dissimilar to the PCMs, the SARs were designed to a linear retardance specification, specifically a combined retardance of 90° ± 30°. The one parameter solved for was the fast axis orientation of the middle plate plates.

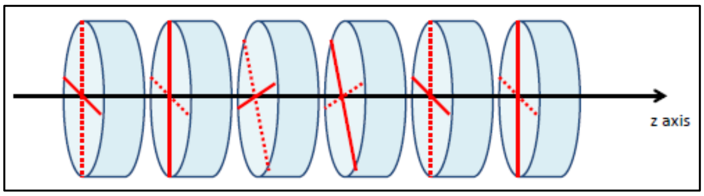

Figure 3.8: Six crystalline plates make up the calibration super achromatic retarder.

Below are tables of the design thicknesses and orientations for all 3 SARs. In Chapter 1 it was explained that 3 and not 4 SARs were designed because the VTF wavelength range falls within the ViSP operation range and therefore the VTF can use the same calibration retarder.

Thickness (mm)	Retardance (waves@633.443nm)	Fast axis orientation (°)
2.1221	30.328	0.00
2.0991	30.000	90.00
2.1324	30.476	70.25
2.0991	30.000	160.25
2.1221	30.328	0.00
2.0991	30.000	90.00

Table 3.7: ViSP SAR design thickness, retardance and fast axis orientation.

Thickness (mm)	Retardance (waves@633.443nm)	Fast axis orientation (°)
2.1469	30.683	0.00
2.0991	30.000	90.00
2.1691	31.000	65.00
2.0991	30.000	155.00
2.1469	30.683	0.00
2.0991	30.000	90.00

Table 3.8: DL-NIRSP SAR design thickness, retardance and fast axis orientation.

Thickness (mm)	**Retardance (waves@633.443nm)**	**Fast axis orientation (°)**
2.27314	42.230	0.00
2.15311	40.000	90.00
2.33321	43.346	107.75
2.15311	40.000	197.75
2.27314	42.230	0.00
2.15311	40.000	90.00

Table 3.9: Cryo-NIRSP SAR design thickness, retardance and fast axis orientation.

3.3.3.1 Designed retarder properties

Plotted below are the designed retardances and fast axis orientations as a function of wavelength of the SARs. The retardance stayed within the $\pm 30°$ of $90°$ over the wavelength range of each instrument and the fast axis orientation changed as a function of wavelength. The dependence of the fast axis orientation on wavelength must be taken into account during the polarization calibration. The expected retardance and fast axis orientation of the designed retarders were utilized in the acceptance testing of the SARs as explained in Chapter 6.

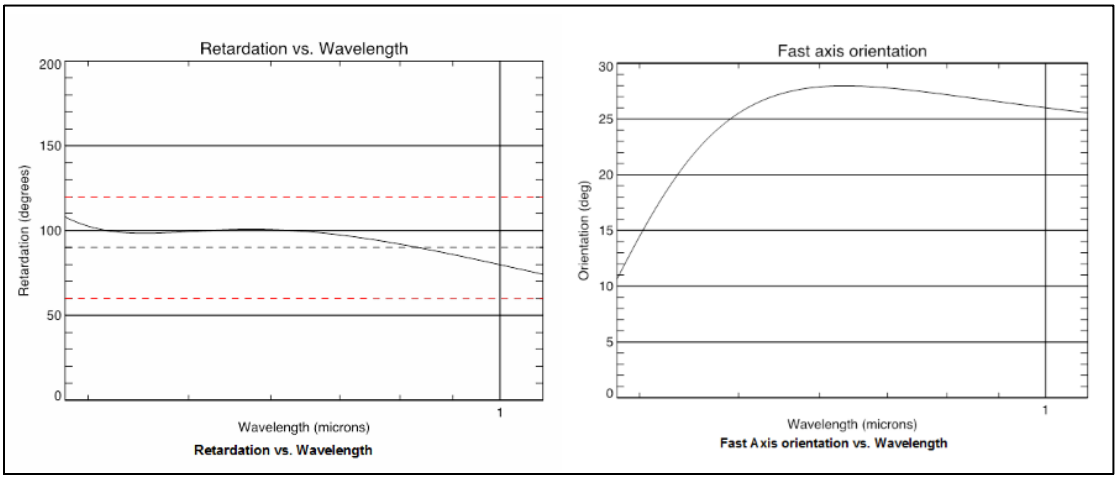

Figure 3.9: ViSP SAR retardance and fast axis orientation versus wavelength.

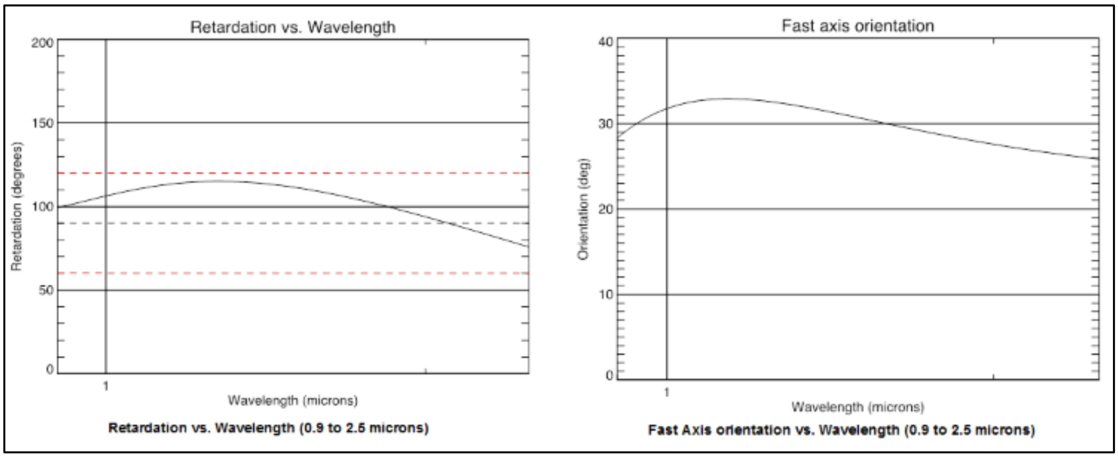

Figure 3.10: DL-NIRSP SAR retardance and fast axis orientation versus wavelength.

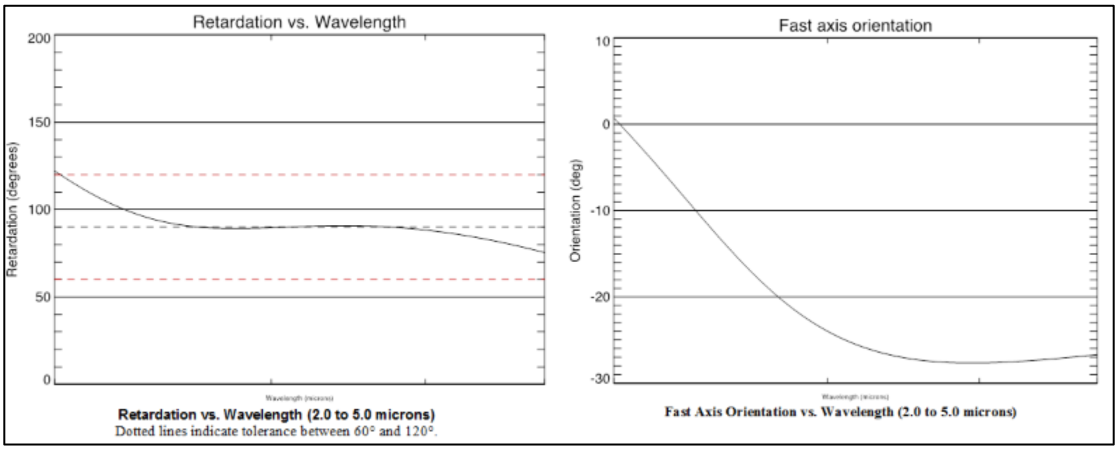

Retardation vs. Wavelength (2.0 to 5.0 microns)
Dotted lines indicate tolerance between 60° and 120°.

Fast Axis Orientation vs. Wavelength (2.0 to 5.0 microns)

Figure 3.11: Cryo-NIRSP retardance and fast axis orientation versus wavelength.

3.3.4 Requirements specific to compound birefringent crystal retarders

This section focuses on the requirements that were specific to the compound birefringent crystal retarders (a stack of crystal plates) designed for DKIST. Thus, the tolerances on the following parameters were provided by the DKIST project to the vendor: Substrate thickness, clocking, optical axis, individual plate retardances, retardance measured at a specific wavelength, bonding, and surface reflections. These requirements are defined below.

3.3.4.1 Substrates

The assemblies were comprised of two non-birefringent substrate plates and six birefringent crystal plates. Six crystal plates were sandwiched between the thick substrate plates. The thicknesses of the individual birefringent crystal plates were approximately 2 millimeters. With an aspect ratio of around 1:60 these plates were prone to damage or possible surface deformations. Two thick substrates were used to provide strength and stability across the diameter of the retarder. Infrasil glass was used for the ViSP and DL-NIRSP retarders, CaF2 crystal was used for the Cryo-

NIRSP retarders. Tabled are the substrate material and thickness specifications for the SAR and PCMs of the different instruments.

	Substrate	**Thickness**
SAR & PCM for ViSP	Infrasil	$10 \pm 1\,mm$
SAR & PCM for DL-NIRSP	Infrasil	$10 \pm 1\,mm$
SAR for Cryo-NIRSP	CaF2	$10 \pm 1\,mm$
PCM for Cryo-NIRSP	CaF2	$10 \pm 1\,mm$

Table 3.10: Material and thickness specification for window substrates.

3.3.4.2 Clocking

A clocking specification was provided to the vendor to ensure the optical axis of each crystal plate in the stack was within a fraction of a degree of the designed orientation.

$$Clocking\ between\ waveplates \pm 0.3°$$

3.3.4.3 Optic axis

Each individual birefringent crystal plate must be single crystal, no twinning. Our vendor has proprietary methods of measuring the optic axis within each crystal plate and provided this information to the project in the data package.

$$Optic\ axis\ in\ the\ plane\ of\ the\ element\ \pm 1.0°$$

3.3.4.1 Plate retardance

In the table below, each letter represents a pair of plates with fast axes crossed. The net retardance of each pair at normal incidence was the difference of individual retardances. These retardance values were specified at 633.443 nanometers at 22° Celsius. The wavelength and temperature were selected based on ease of the vendor to provide the DKIST project the measurements at those values. Plates A through D were A-cut quartz, and E through H were A-cut MgF2.

Plate	**Retardation**
A1	$A2 + 0.476\ waves$
A2	$30 \pm 1\ waves$
B1	$B2 + 0.328\ waves$
B2	$30 \pm 1\ waves$
C1	$C2 + 1.000\ waves$
C2	$30 \pm 1\ waves$
D1	$D2 + 0.683\ waves$
D2	$30 \pm 1\ waves$
E1	$E2 + 1.893\ waves$
E2	$40 \pm 1\ waves$
F1	$F2 + 1.282\ waves$
F2	$40 \pm 1\ waves$
G1	$G2 + 2.230\ waves$
G2	$40 \pm 1\ waves$
H1	$H2 + 3.346\ waves$
H2	$40 \pm 1\ waves$

Table 3.11: Individual plate retardance values.

3.3.4.2 Normal incidence retardance

At normal incidence, the retardance was measured at a wavelength of 633.443 nm and a temperature of 22° Celsius.

$$Retardance\ to\ within \pm 0.01\ waves\ over\ the\ clear\ aperture$$

3.3.4.3 Surface reflections

Reflections within the surfaces of the retarders could lead to fringing effects in the data. In particular, the compound retarders consist of a stack of birefringent crystals with isotropic layers of oil between. The root sum squared of the surface reflections of all elements in the compound had to meet the requirement.

The ViSP and DL-NIRSP calibration retarders required a surface reflection less than an uncoated quartz surface for all wavelengths within its pass band and average $< 3\%$ for all wavelengths. For the Cryo-NIRSP calibration retarder, the surface reflection was required to be less than or equal to that of an uncoated CaF2 surface for all wavelengths within its passband (D. Elmore et al., 2014).

The modulator retarders had a similar requirement for surface reflections. ViSP and DL-NIRSP modulator surface reflection had to be less than an uncoated quartz surface for all wavelengths and average $< 2\%$ and $< 2.5\%$ respectively, for all wavelengths within their passband. The Cryo-NIRSP modulator surface reflection had to be less than or equal to an uncoated MgF2 surface for all wavelengths within its passband.

3.3.5 Conclusion

Six retarder designs were shown, 3 PCMs and 3 SARs over distinct wavelength ranges. The DKIST retarders were made of six birefringent crystal stacks. Each stack contains three pairs of crossed fast axis A-cut plates. The clocking of the fast axes of each pair of plates were expected at a particular angle with respect to each other. The crossed fast axes pairs created a combined zero-order retardance value.

These designs were unique and complex. With the assumed conditions of the telescope, it was important to predict the Mueller matrix and retardance changes. In the next section, models that were developed to understand a major area of concern; the angle of incidence and field of view effects.

4 RETARDER MODELING

4.1 Introduction

Defining the telescope polarimetric error budget is a difficult Systems Engineering task that is still being worked on during the time this dissertation is being written. The error budget is a working spreadsheet, and as the DKIST polarization team researches ways to mitigate large error contributors, the error budget allocations toward these different contributors will change. However, to frame the work discussed in the next few chapters, the maximum uncertainty allowed for primary sources of polarization calibration error was based on the polarimetric error budget outlined in the DKIST Systems Error Budget document.

In this chapter, the current polarimetric error budget allocation to the calibration retarders is described, and the current retarder model for the calibration process is illustrated. In an ideal scenario, one can assume a perfect linear retarder model for the SAR design. Section 4.3 explains the polarization ray trace performed to show how the retarder's Mueller matrix varied as a function of angle of incidence. Section 4.4 shows how angle of incidence ray trace data was used to model the effects of the retarder in a converging f/13 beam, over a 5 arc-minute field of view. The goal of this chapter is to help the reader understand that the calibration retarder's Mueller matrix was not ideal and required other forms of modeling in order to reduce it's contributions to the polarimetric error budget.

4.2 DKIST polarimetric error budget and retarder model

The DKIST top-level specification document describes an extremely tight polarization accuracy specification. The errors in the fractional polarization measured (Q/I, U/I, V/I) must be less than 5×10^{-4} of the continuum intensity. In order to achieve this goal, the telescope group model and modulation matrix must be fit such that the error from polarization aberrations in the telescope is below the specified level at all observation wavelengths. In this section, telescope polarimetric error table and the baseline retarder model selected for the calibration retarder are introduced.

4.2.1 Telescope polarization calibration

The goal is to fit the telescope group model such that the polarization effects of the telescope optics are well understood and can be removed from the input signal. In other words, if $\boldsymbol{M_{tel}}$, the telescope Mueller matrix is fit, then M_{tel}^{-1} can be calculated and removed from the measured signal. Recall equation (1.5), the Stokes vector entering the telescope can be recovered with the highest accuracy if the telescope's Mueller matrix is known, and the intensity measurements are demodulated.

The error table for polarimetric accuracy is defined in the Systems Error Budget Document as the following:

"The amplitude of each element Mij of the end-to-end Mueller matrix M (telescope plus polarimeter) must be known to an accuracy ±ε ij at all times, i.e. Mij ± ε ij. The error matrix, ε, is not a Mueller matrix a strict sense but more accurately a table of the required maximum uncertainty in knowledge of crosstalk among Stokes parameters. The matrix is derived using the method of Ichimoto et al (Polarization Calibration of the Solar Optical Telescope onboard Hinode, Solar Physics, Volume 249, No 2, 2008) using a required accuracy of 5×10-4, maximum input Q, U, and V of 10%, and flat fielding to 1%."

$\mathbf{10^{-2}}$	$\mathbf{10^{-2}}$	$\mathbf{10^{-2}}$	$\mathbf{10^{-2}}$
$\mathbf{5\times10^{-4}}$	$\mathbf{10^{-2}}$	$\mathbf{5\times10^{-3}}$	$\mathbf{5\times10^{-3}}$
$\mathbf{5\times10^{-4}}$	$\mathbf{5\times10^{-3}}$	$\mathbf{10^{-2}}$	$\mathbf{5\times10^{-3}}$
$\mathbf{5\times10^{-4}}$	$\mathbf{5\times10^{-3}}$	$\mathbf{5\times10^{-3}}$	$\mathbf{10^{-2}}$

Table 4.1: The DKIST polarimetric error table represents the maximum uncertainty in each of the Mueller matrix elements.

This error table was divided among the primary sources of calibration error. The root sum square of all the errors resulted in the full error matrix for the telescope. M_1 and M_2 had the largest calibration uncertainty and therefore the largest error allocation. In-situ measurements provides the partially polarized light source for the calibration of these mirrors, but cannot nearly be as controlled as the calibration optics that provide known polarization states to calibrate the rest of the telescope optics. The error budget was broken down further among the telescope group model optics. The plan is to calibrate these elements with the calibration optics. Another allocation divides the error budget into the calibration components.

Error budgeted to the calibration retarder was for orientation and thermal stability on the assumption that the calibration retarder would fit the linear retarder model. Other factors that may contribute to errors in the calibration retarder are angle of incidence and field of view. These were explored and are discussed in the following sections.

4.2.2 Ideal linear retarder model

The Mueller matrix of an ideal linear retarder is

$$\boldsymbol{LR[\delta,\theta]} =$$

$$\begin{pmatrix} 1 & 0 & 0 & 0 \\ 0 & \cos^2 2\theta + \cos\delta \sin^2 2\theta & (1-\cos\delta)\cos 2\theta \sin 2\theta & -\sin\delta \sin 2\theta \\ 0 & (1-\cos\delta)\cos 2\theta \sin 2\theta & \cos\delta \cos^2 2\theta + \sin^2 2\theta & \cos 2\theta \sin\delta \\ 0 & \sin\delta \sin 2\theta & -\cos 2\theta \sin\delta & \cos\delta \end{pmatrix}. \quad (4.1)$$

δ is the linear retardance and θ, the fast axis orientation are two parameters that define a linear retarder. The project had an error allocation for the accuracy of the physical orientation of the retarder upon rotation and the changes in the Mueller matrix as a function of temperature. No other errors were taken into account. The next section illustrates the polarization ray trace of the calibration retarder, showing how the variations in angle of incidence and field of view caused the Mueller matrix to stray from the ideal linear retarder case.

4.3 Modeling with polarization analysis tools

4.3.1 Polarization ray trace modeling of angle of incidence dependence

Rays refracting through isotropic medium are predictable and simple to trace. The refractive index is constant in all directions, so it is easy to trace a ray and keep track of it as it propagates. Anisotropic media such as uniaxial crystals have two principal refractive indices, ordinary and extraordinary. This causes light to travel at different speeds depending on the refractive index it sees. Essentially, polarization properties are different depending on the incidence angle and incident polarization state. In the case of non-normal incidence, rays will split and have different propagation directions.

By utilizing the polarization ray tracing module Polaris-M (Lam, McClain, Smith, & Chipman, 2010; Yun, Crabtree, & Chipman, 2011; Yun, Mcclain, & Chipman, 2011), optical components were modeled and the polarization properties were calculated. Polaris-M is an in house polarization ray tracing software developed at the University of Arizona’s Polarization Laboratory. Polaris-M provides the capability of performing a ray trace through the stack of isotropic and anisotropic materials, keeping track of the polarization state, propagation vector, and optical path length of each of the propagating modes. The unique feature of Polaris-M is its ability to track all the rays from ray splitting caused by anisotropic material interfaces.

This section focuses on the simple case of an A-cut retarder plate. It provides a basic understanding of the retarder ray trace and makes it easier to understand the compound crystal polarization ray trace in Section 4.3.2.

4.3.1.1 Optical system definition:

First, the optical system is defined by creating each surface with several important parameters: surface index number, surface shape, material type, surface vertex position, surface normal at the vertex, aperture function, coating specification and interaction type with the surface.

Starting with a simple example of a single birefringent crystal plate in air as shown in Figure 4.1. Surface index number is defined for each surface of the optical system. In this case there are three surfaces, one for each face of the crystal plate, and a final surface where split rays will recombine. The vertex of each surface in global coordinates defines the location of each surface. For each surface the shape parameters are defined as planar and the surface normal vector is given at the vertex.

The aperture function in Polaris-M allows the software to determine if a particular incident ray passes through the aperture of the element, it returns a Boolean value. Coating specification allows the user to define the type of coating, thicknesses and indices of each layer. In the modeled case discussed here, coatings were not defined. The system mode is defined to tell the software whether the surface interaction will be refracting, reflecting, or absorbed.

Each surface contains information on two materials: the incident medium and the exiting medium. It is in the “material type” definition where the index of refraction or dispersion of the material is defined. An important feature of Polaris-M occurs when an anisotropic material is used. The software automatically performs the ray splitting at this isotropic to anisotropic interface.

Anisotropic materials such as uniaxial crystals have specific material parameters that must be defined: the ordinary refractive index, extraordinary refractive index, and the optic axis of the crystal. Most common crystals dispersion functions are in the Polaris-M materials database and can be called by inputting the crystal name. The optic axis is defined as the following vector,

$$\mathbf{OA} = \{\{\sin\boldsymbol{\alpha}\cos\boldsymbol{\beta}, \sin\boldsymbol{\alpha}\sin\boldsymbol{\beta}, \cos\boldsymbol{\alpha}\}\} \tag{4.2}$$

Where α is the angle between the normal of the crystal plate and the optic axis, and β is the angle counterclockwise from horizontal looking into the beam. For example, a vertically oriented optic axis of {{0,1,0}} has α=90° which puts it in the plane of the crystal, and β=90° which is a counterclockwise angle from +x looking into the beam. It is important to note that Polaris-M uses the optic axis orientation, not the fast axis specifically. One must remember that the optic axis, also known as the crystal axis is associated with the extraordinary refractive index. For positive uniaxial crystals such as quartz and MgF2, this is the SLOW axis.

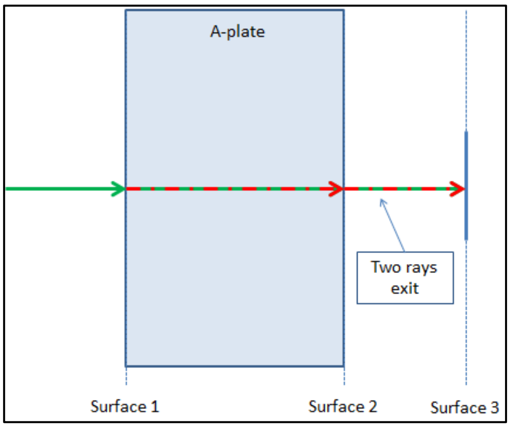

Figure 4.1: Normal incidence ray on a single plate of uniaxial crystal.

4.3.1.2 Ray parameters

Once the optical system is defined the next step is to generate the rays. First, the initial ray position **r** in Figure 4.1 is on the optical axis before surface 1. All rays generated in the ray trace come from this source location. The propagation vector **k** is parallel to the surface normal vector. Both **r** and **k** are defined in global coordinates. Next, the wavelength at which this interaction occurs is defined. In the optical system, if the material dispersion is defined, then the wavelength selected here determines the refractive index seen by the ray. Finally, since Polaris-M is equipped to perform non-sequential ray tracing, the sequential surface order in which the ray interacts with the crystal plate must be defined as a 1-dimensional array of integers {1,2,3}.

4.3.1.3 Ray tracing the A-plate, normal incidence

In the case of a single normal incident ray as shown Figure 4.1 ray splitting occurs at the isotropic to crystal interface. The initial green ray splits into two propagating modes, the green solid ray and the red dot-dashed ray. The two modes follow the same propagation direction but one sees the ordinary refractive index and the other sees the extraordinary refractive index. Polaris-M labels these modes as O and E respectively.

The output ray information from Polaris-M in Figure 4.2 shows the ray interactions with each surface. Columns shown here are: Surface index number, ray position **r**, propagation vector **k**, cumulative optical path length, cumulative PRT matrix, and mode label. The PRT matrix given in equation (4.3), is a three dimensional polarization matrix that contains the information of the orthogonal polarization modes **s** and **p,** and the propagation direction **k**. Essentially it is the Jones matrix converted to 3-dimensional space. The ray splits at surface 1 into the O and E modes, circled in red in Figure 4.2. These two modes continue to propagate separately even though they exit the crystal at the same location.

$$\begin{pmatrix} \boldsymbol{s_x} & \boldsymbol{p_x} & \boldsymbol{k_x} \\ \boldsymbol{s_y} & \boldsymbol{p_y} & \boldsymbol{k_y} \\ \boldsymbol{s_z} & \boldsymbol{p_z} & \boldsymbol{k_z} \end{pmatrix} \tag{4.3}$$

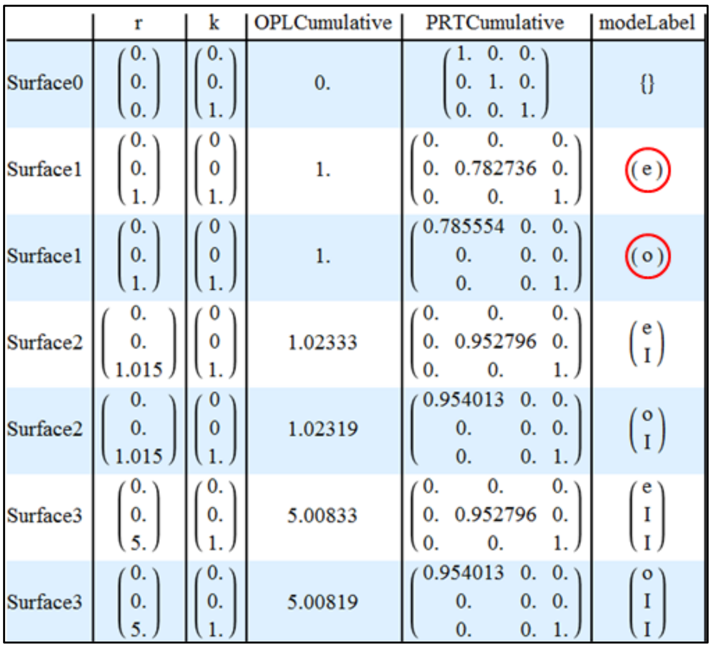

	r	k	OPLCumulative	PRTCumulative	modeLabel
Surface0	$\begin{pmatrix} 0. \\ 0. \\ 0. \end{pmatrix}$	$\begin{pmatrix} 0. \\ 0. \\ 1. \end{pmatrix}$	0.	$\begin{pmatrix} 1. & 0. & 0. \\ 0. & 1. & 0. \\ 0. & 0. & 1. \end{pmatrix}$	{}
Surface1	$\begin{pmatrix} 0. \\ 0. \\ 1. \end{pmatrix}$	$\begin{pmatrix} 0 \\ 0 \\ 1. \end{pmatrix}$	1.	$\begin{pmatrix} 0. & 0. & 0. \\ 0. & 0.782736 & 0. \\ 0. & 0. & 1. \end{pmatrix}$	(e)
Surface1	$\begin{pmatrix} 0. \\ 0. \\ 1. \end{pmatrix}$	$\begin{pmatrix} 0 \\ 0 \\ 1. \end{pmatrix}$	1.	$\begin{pmatrix} 0.785554 & 0. & 0. \\ 0. & 0. & 0. \\ 0. & 0. & 1. \end{pmatrix}$	(o)
Surface2	$\begin{pmatrix} 0. \\ 0. \\ 1.015 \end{pmatrix}$	$\begin{pmatrix} 0 \\ 0 \\ 1. \end{pmatrix}$	1.02333	$\begin{pmatrix} 0. & 0. & 0. \\ 0. & 0.952796 & 0. \\ 0. & 0. & 1. \end{pmatrix}$	$\begin{pmatrix} \text{e} \\ \text{I} \end{pmatrix}$
Surface2	$\begin{pmatrix} 0. \\ 0. \\ 1.015 \end{pmatrix}$	$\begin{pmatrix} 0 \\ 0 \\ 1. \end{pmatrix}$	1.02319	$\begin{pmatrix} 0.954013 & 0. & 0. \\ 0. & 0. & 0. \\ 0. & 0. & 1. \end{pmatrix}$	$\begin{pmatrix} \text{o} \\ \text{I} \end{pmatrix}$
Surface3	$\begin{pmatrix} 0. \\ 0. \\ 5. \end{pmatrix}$	$\begin{pmatrix} 0. \\ 0. \\ 1. \end{pmatrix}$	5.00833	$\begin{pmatrix} 0. & 0. & 0. \\ 0. & 0.952796 & 0. \\ 0. & 0. & 1. \end{pmatrix}$	$\begin{pmatrix} \text{e} \\ \text{I} \\ \text{I} \end{pmatrix}$
Surface3	$\begin{pmatrix} 0. \\ 0. \\ 5. \end{pmatrix}$	$\begin{pmatrix} 0. \\ 0. \\ 1. \end{pmatrix}$	5.00819	$\begin{pmatrix} 0.954013 & 0. & 0. \\ 0. & 0. & 0. \\ 0. & 0. & 1. \end{pmatrix}$	$\begin{pmatrix} \text{o} \\ \text{I} \\ \text{I} \end{pmatrix}$

Figure 4.2: Polaris-M output for single normal incident ray.

When the rays exit the crystal plate at surface 2 the cumulative optical path lengths and PRT matrices are different. In order to determine the PRT matrix that represents the A-plate's total polarization effects on the single input ray, the exiting rays must be combined. Surface 3 is a dummy surface in air following the retarder. It has a surface normal parallel to the propagation vector **k** in air. Equation (4.4) is used to calculate the final cumulative PRT matrix of the retarder (R. A. (College of O. S. Chipman, Yun, & Lam, 2017).

$$\left(\sum_{\boldsymbol{n}} (\boldsymbol{PRT_n} - \boldsymbol{Outer}[\boldsymbol{k_{in}}, \boldsymbol{k_{out}}]) \boldsymbol{e}^{-\frac{2\pi}{\lambda}\boldsymbol{OPL_n}}\right) + \boldsymbol{Outer}[\boldsymbol{k_{in}}, \boldsymbol{k_{out}}] \tag{4.4}$$

As mentioned before, the PRT matrix is a 3 dimensional representation of the Jones matrix in global coordinates. Subtracting the outer product of the incident and exiting propagation vectors allows the addition of the Jones matrices in local coordinates. The optical path lengths are summed together as well. Finally the outer product of the k vectors is added back to the PRT matrix to give a final 3 dimensional matrix.

4.3.1.4 Ray tracing the A-plate, non-normal incidence

When a ray is incident on an A-plate off axis the propagation direction of the O and E mode are no longer the same as shown in Figure 4.3. The two modes exit the crystal at different locations but propagate parallel once they are back in air. Here is an explanation of how the modes are still combined together.

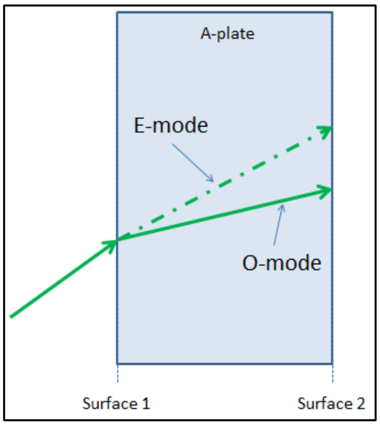

Figure 4.3: Off axis ray incident on the crystal A-plate.

Consider a second ray that is parallel to the first incident ray, shown in Figure 4.4. It is shifted just above the first ray such that its O mode overlaps the exiting E mode of the first ray. These two rays can be combined in the same way as the normal incident ray using Equation (4.4). There is a change in the optical system that needs to be made for each off axis propagation vector. Surface 3 is no longer be parallel to the A-plate, but always normal to the propagation vector of the exiting rays or else the OPL is incorrect.

One can also see in this figure that OPL of the O modes are the same. However, for computing the ray trace it is easier to generate the ray from a single point. If two rays were traced it would be necessary to determine the starting ray position of Ray 2 such that its O mode exactly overlaps with the E-mode of Ray 1.

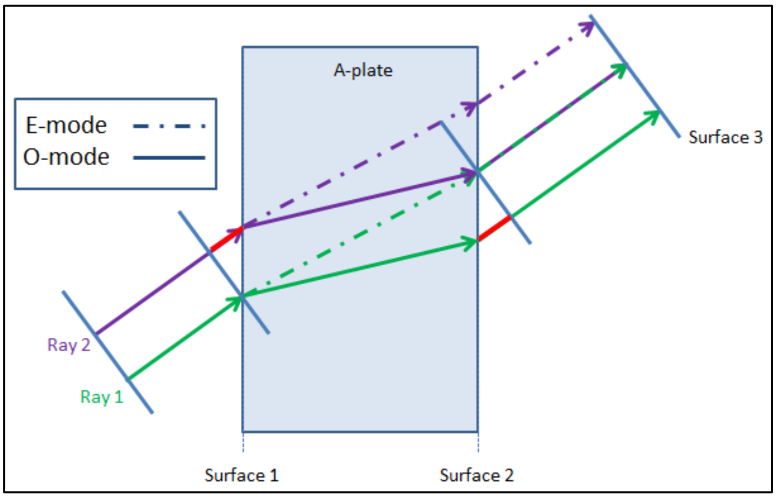

Figure 4.4: First ray in green and second ray from the same wavefront in purple. Rays from the same wavefront can be combined at surface 3. The extra optical path length in red is observed in the o-mode of both rays.

4.3.1.5 Trace a grid of rays over a range of AOI

Sections 4.3.1.3 and 4.3.1.4 illustrated the calculation of the PRT matrix for normal incidence and off axis rays respectively. The three dimensional PRT matrix is converted to a Mueller matrix for the analysis shown in the next sections.

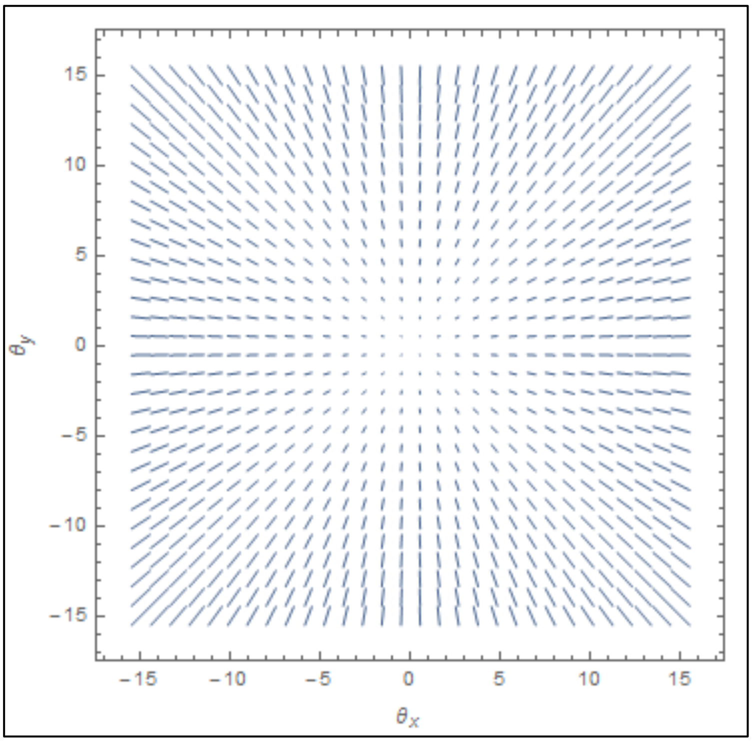

Figure 4.5: Shown is sampling of a grid of rays over a 15°×15° angular range with different incident k vectors traced through the crystal. The length of the vectors represents the magnitude of the incidence angle.

A grid of incident k vectors was created to trace through the retarder. Angularly they were evenly separated and sampled within the angular aperture for each field angle, shown in the figure above. The next section describes a comparison of the Mueller matrix elements, the retarder vector components, and the net retardance magnitude as a function of angle of incidence.

4.3.1.5.1 True zero-order quarter wave retarder

To confirm the ray trace was correct, the well-characterized zero-order quarter wave A-cut retarder was first considered(Hale & Day, 1988; Mcclain & Chipman, 1992). The material modeled was crystalline quartz, with optic axis horizontally oriented along the x-axis. The extraordinary refractive index is greater than the ordinary refractive index because quartz is a positive uniaxial crystal. Therefore the slow axis of this retarder was along the y-axis.

The $\pm 15°$ grid of angles in both the x and y direction was traced through the retarder. For each initial ray the PRT was calculated at a dummy surface outside the retarder in air (where $\boldsymbol{k_{in}}$ and $\boldsymbol{k_{out}}$ are equal). The PRT was converted to a Mueller matrix and plotted in the following figure.

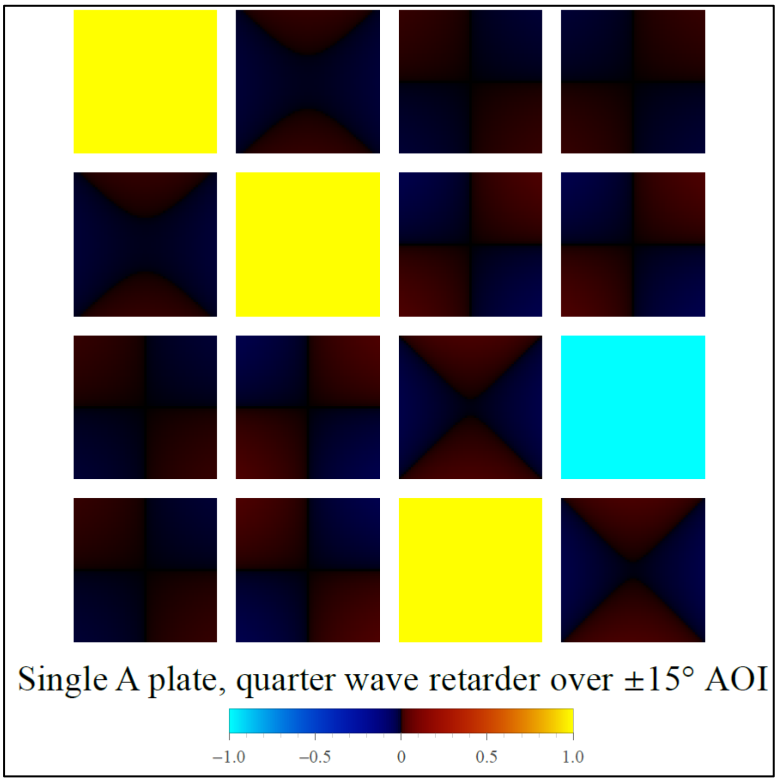

Figure 4.6: Mueller matrix of a true zero-order quartz retarder with fast axis vertical. The color bar at the bottom of the figure represents amplitude of the Mueller matrix elements from -1 to 1. Each Mueller matrix element represents the behavior over a 15°×15° angle of incidence range.

Angle of incidence effects were small in the Mueller matrix elements of this true zero-order retarder. Plotted in Figure 4.7 are the retarder vector components that represent the retardance magnitude of the horizontal, 45° and right circular retardance respectively. The root sum squared of these retarder components equals the total retardance magnitude plotted in Figure 4.8. It was found that the largest change (increase and decrease) in retardance occured along the fast and slow axes, in this case less than 1.5°.

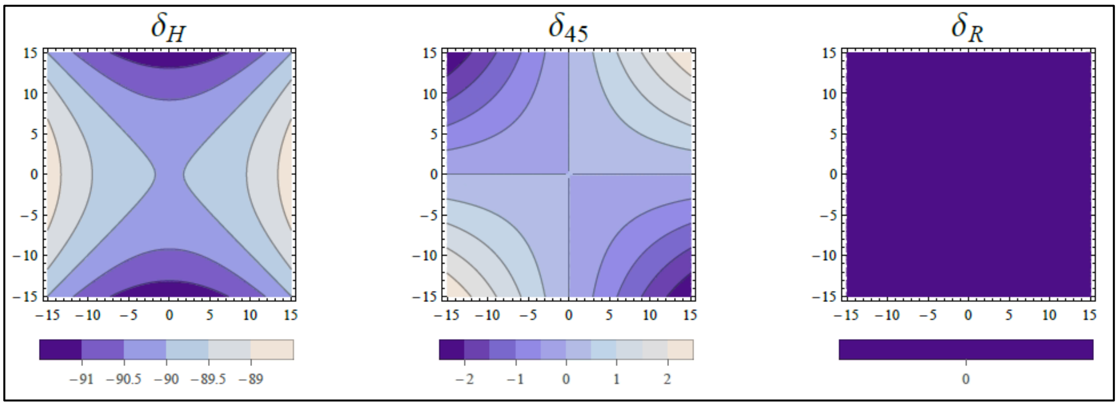

Figure 4.7: Retarder vector components for the zero-order quartz retarder single plate.

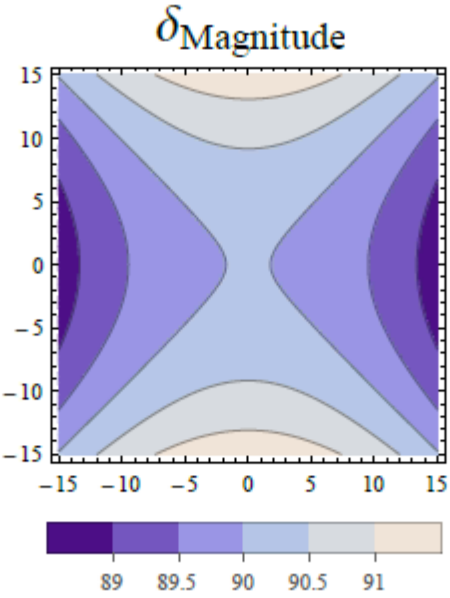

Figure 4.8: Retardance magnitude of the true zero-order quarter wave retarder

4.3.1.5.2 Multi-order quarter wave retarder

The second simple retarder modeled was a thicker uniaxial crystal plate. The retardance of this plate at normal incidence was an integer multiple of 360° plus 90°. Similar to the zero-order retarder shown in the previous section, the material was crystalline quartz, with optic axis horizontally oriented along the x-axis.

The ±15° grid of angles in both the x and y direction was traced through the multi-order quarter wave A-cut retarder element. The figure below shows the Mueller matrix amplitude changed much more over the grid of angles than the zero-order retarder.

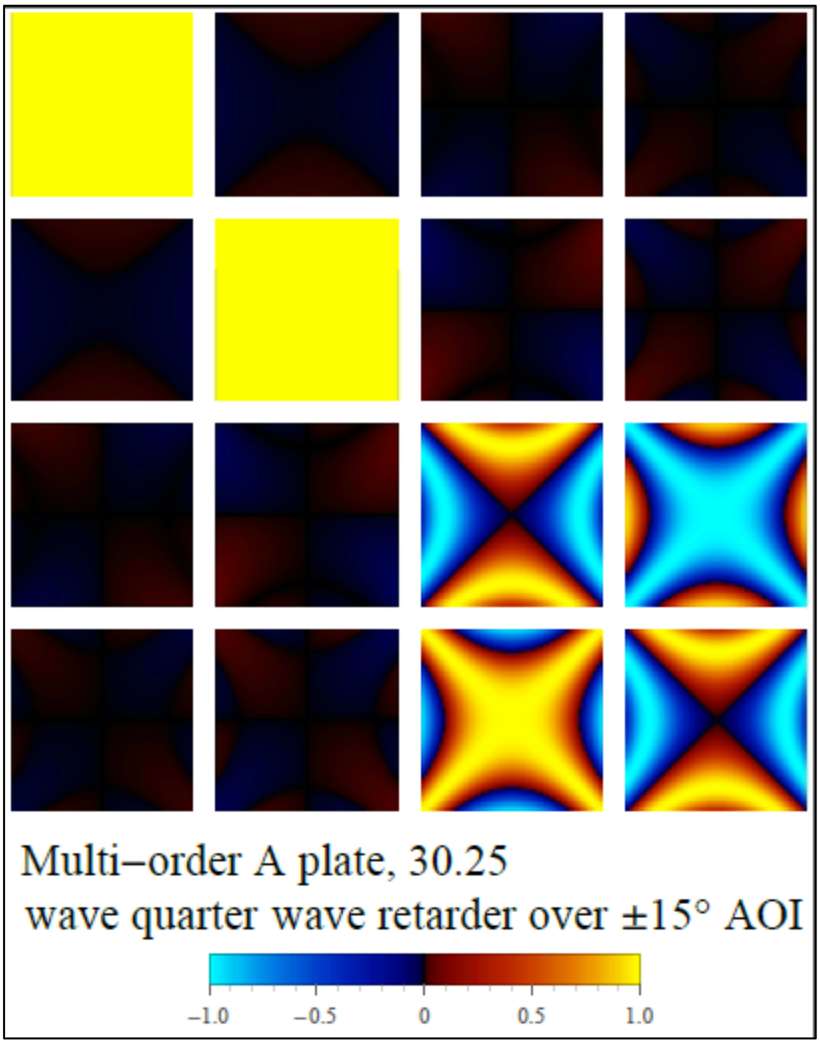

Figure 4.9: Mueller matrix of a multi-order quartz retarder with fast axis vertical over $\pm 15°$ angle of incidence.

The horizontal retarder vector component shows a much larger angle of incidence dependence as phase wrapping occurs at the $-180°$ and $+180°$ border.

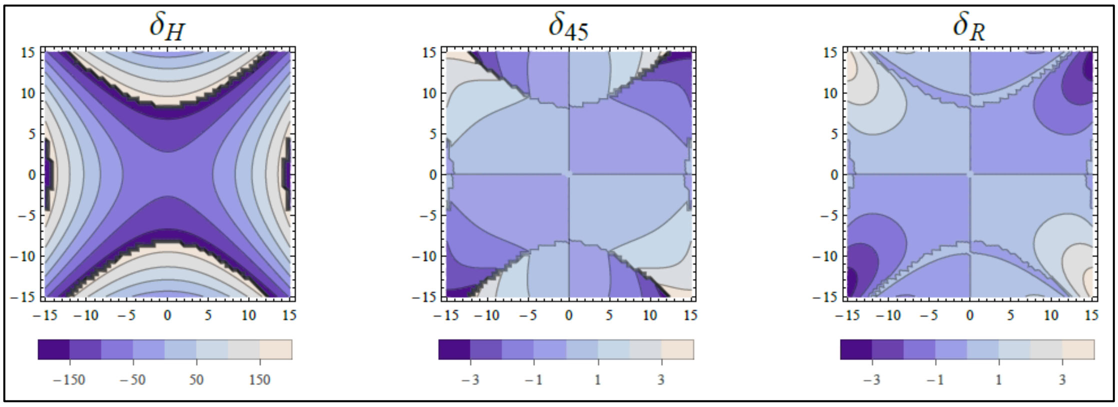

Figure 4.10: Retarder vector components for the multi-order quartz retarder single plate.

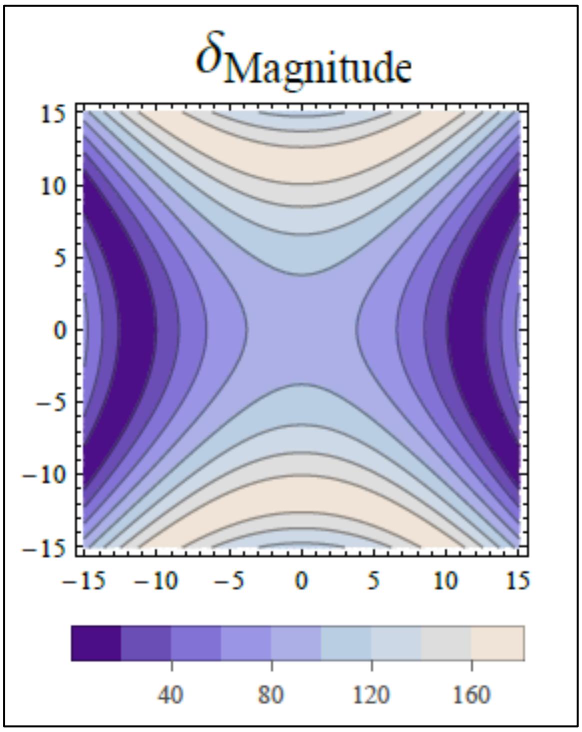

Figure 4.11: Retardance magnitude of the multi-order quarter wave retarder

4.3.1.5.3 Compound zero-order quarter wave retarder

Finally, a zero-order compound retarder was modeled. The compound retarder consists of two multi-order plates with crossed fast axes. Angle of incidence effects shown below are larger than both the true-zero order retarder and the multi-order case. The retardance of this plate at normal incidence was 90° due to the subtracted multi-order retardance of the two plates. Similar to the zero-order retarder, the material was crystalline quartz, with optic axis horizontally oriented along the x-axis. The ±15° grid of angles in both the x and y direction was traced through the multi-order quarter wave A-cut retarder element.

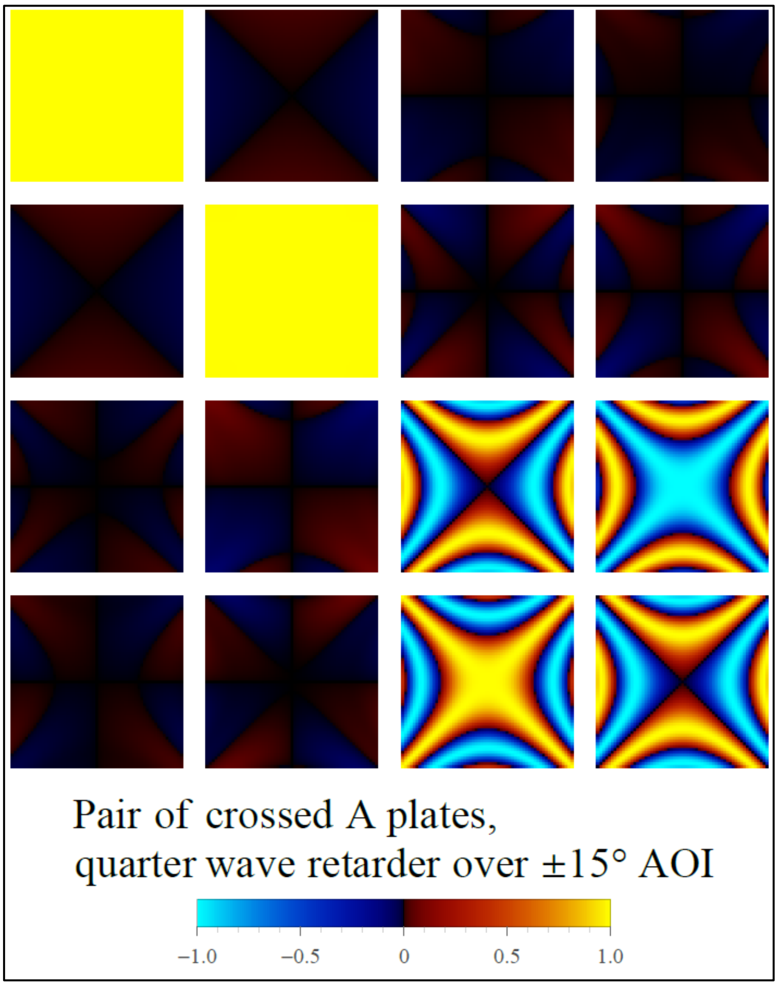

Figure 4.12: Mueller matrix of a compound zero-order quarter wave retarder with fast axis vertical over ±15° angle of incidence.

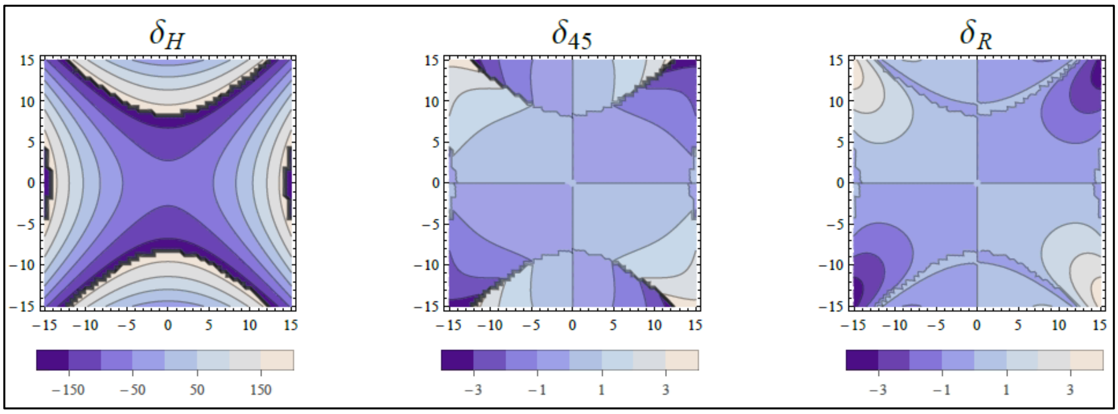

Figure 4.13: Retarder vector components for a pair of crossed A plates with net zero order quarter wave retardance

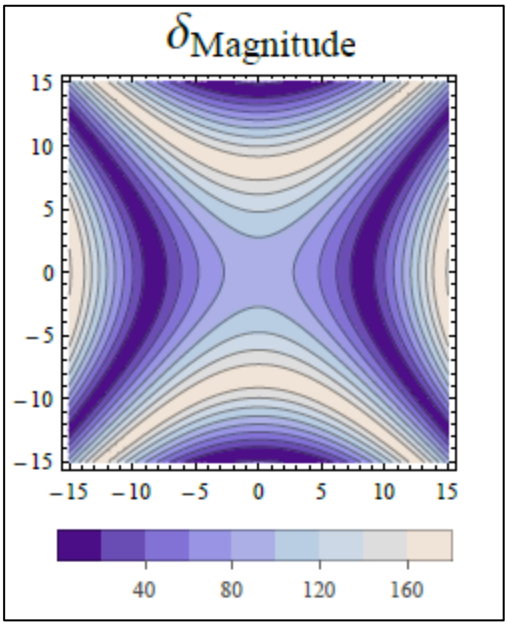

Figure 4.14: Retardance magnitude of the compound zero-order quarter wave retarder

The retardance magnitude showed much larger angle of incidence dependence as phase wrapping occurs. Note, along the vertical axis the retardance goes from 90° at the center, up through $+180°$ and then back down to $-180°$. This was double the retardance magnitude variation seen in the multi-order retarder.

4.3.1.5.4 Conclusion

The last three sections were intended to help the reader understand the angle of incidence effects on several crystal plate cases in order to better understand the effects on DKIST retarders.

4.3.2 Modeling angle of incidence on the DKIST retarders

DKIST retarders were modeled and the angle of incidence effects on the Mueller matrix of the SARs is investigated. The DKIST SAR and PCM retarders were made up of six layers of birefringent material with isotropic layers between each crystal plate. Polaris-M ray tracing software allows one to keep track of all the ray splitting through the birefringent layers and provides the information needed to calculate the Mueller matrix of the retarder as seen by a particular ray. Ordinary and extraordinary modes were propagated through each surface and continued to split as they encountered more anisotropic substrates.

4.3.2.1 PolarisM ray trace of the DKIST retarders

4.3.2.1.1 Optical system definition:

First, the optical system of a DKIST retarder was defined by creating each surface with several defining parameters: surface index number, surface shape, material type, surface vertex position, surface normal at the vertex, aperture function, coating specification and interaction type with the surface.

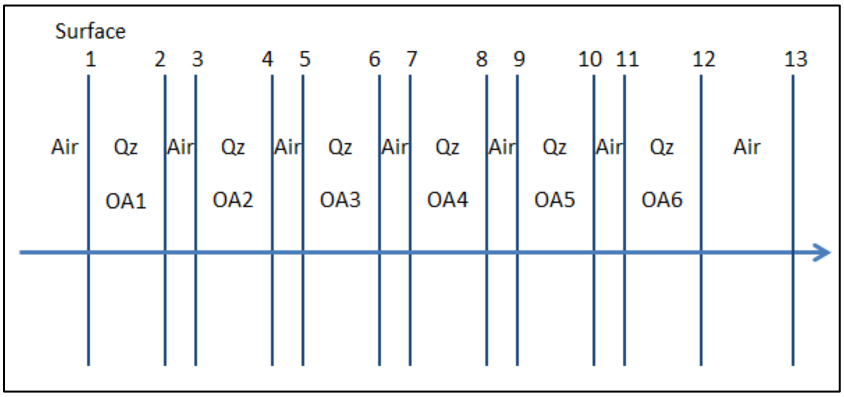

Figure 4.15: Optical system of one of the quartz crystal stacks in Polaris-M.

Initially, a simplified version of the retarder air-spaced and with no substrate plates was modeled in Figure 4.15. A surface index number was given to each surface created in the optical system. In this case we create 12 surfaces to define the compound retarder, and a final 13th surface, a dummy surface in air beyond the compound retarder. At the final dummy surface the rays were combined in order to calculate the cumulative effects of the single incident ray on the retarder.

The surface shape was defined; it was fairly simple in this case as each surface was nominally flat so this parameter was zero. Each surface contains information on two materials: the incident medium and the transmitted medium. The index of refraction or dispersion of the material was specified in the material type. This parameter defines whether the material is either isotropic or anisotropic. By specifying the material as a uniaxial crystal, the software automatically performed the ray splitting at this isotropic to anisotropic interface. The crystal type was defined to automatically pull the dispersion function for that crystal from the materials database.

The surface vertex provided the position of the surface vertex in global coordinates. The aperture function determined if a particular incident ray passed through the aperture of the element. Coating specification allowed the user to define the type of coating, thicknesses and indices of each layer. In this case coatings were yet to be determined and therefore not included in the model. Finally, a mode was defined that told the software whether the surface interaction would refract, reflect, or absorb.

For a uniaxial material the optic axis orientation was defined. It was important to distinguish that Polaris-M uses the optic axis orientation, not the fast axis in the input parameters. One must remember that the optic axis, also known as the crystal axis is associated with the extraordinary refractive index. For positive uniaxial crystals such as quartz and MgF2, this is the SLOW axis. In the retarder design drawings, the retarder clocking angle was specified with respect to the fast axis. For the input into Polaris-M, one must rotate it by 90° to get the optic axis orientation correct.

4.3.2.1.2 Combining split rays

Since the compound retarder is modeled in air, the propagation direction of the rays incident and exiting will remain the same. As the incident vector veers away from normal incidence ray splitting occurs, as shown in section 4.3.1, and causes the modes to split. The resulting rays will exit the compound retarder at offset locations but parallel to one another. The surface normal of the final surface is always parallel to the exiting rays so that the parallel rays that exit the compound retarder can be combined.

4.3.2.1.3 Define optic axis

The optic axis orientation was defined by

$$\mathrm{OA} = \{\{\sin\alpha\cos\beta\,, \sin\alpha\sin\beta\,, \cos\alpha\}\}$$

Where α was the angle between the normal of the crystal plate and the optic axis, and β was the angle counterclockwise from horizontal looking into the beam. For example, a vertically oriented optic axis of {{0,1,0}} has α=90° which puts it in the plane of the crystal, and β=90° which is a counterclockwise angle from +x looking into the beam.

4.3.2.1.3.1 An interesting case regarding coordinate system definition

The PA&C drawings of the ViSP SAR are defined with the right-handed coordinate system looking at the detector. In Polaris-M the right-handed coordinate system is defined as looking into the beam. The difference is shown in Figure 4.16, both coordinate systems consider +z toward the detector.

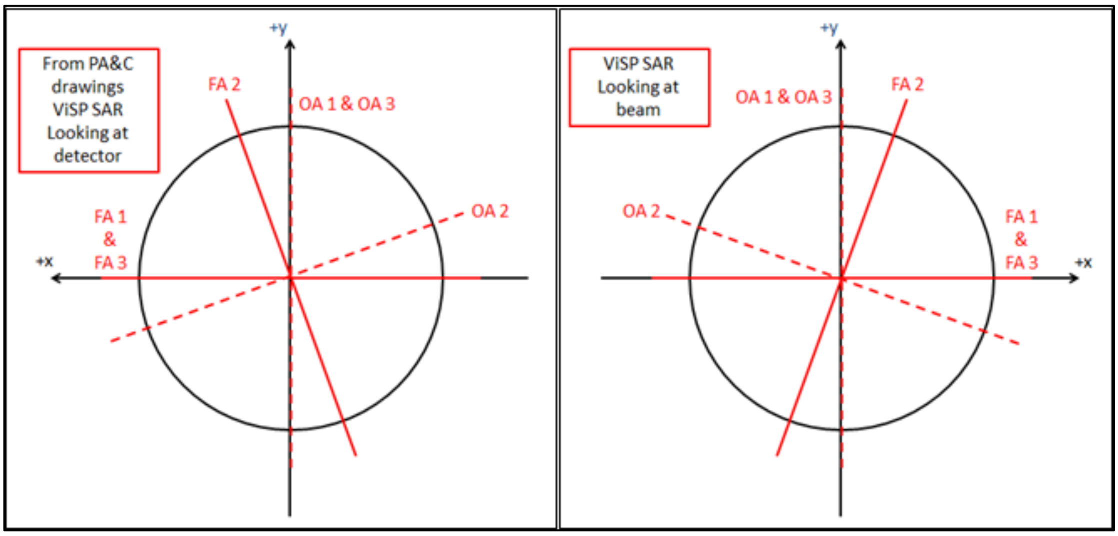

Figure 4.16: Coordinate system difference between design drawing (left) and input to Polaris-M (right). In both cases the +z direction is toward the detector, but this flips the orientation of +x.

4.3.2.2 Ray trace:

After the optical system was defined the ray trace was performed. Some of the optical system parameters were wavelength dependent, so the first step was to determine the ray trace wavelength. For example, if the material dispersion function was defined, then the wavelength selected here determines the refractive index seen by the ray. Next the starting ray position was defined on the optical axis at a nominal position of $\{0,0,0\}$. All rays generated in this ray trace come from this source location. The ray propagation vector **k** was defined and had dependence on the angle of incidence on the compound retarder. Finally, since Polaris-M is equipped to perform non-sequential ray tracing the surface order of the elements in the compound retarder that they rays encounter were defined.

4.3.2.3 Wavelength selection for the DKIST SAR and PCMs:

A sampling of wavelengths was selected over the operation range of each of the DKIST instruments. Minimum and maximum wavelengths were selected, as well as 633.443nm, the wavelength that Meadowlark performs pair retardance measurements at during the fabrication of the retarders.

4.3.2.4 Example ray trace of the ViSP SAR

4.3.2.4.1 On axis

For 6 anisotropic substrates each ray that splits continued to propagate through the rest of the compound retarder and resulted in 64 rays exiting the retarder. Due to the crossed fast axes design of each pair of plates, some rays do not couple any energy into the following mode. After exiting the retarder the rays were combined at a surface normal to the ray propagation vector **k**.

Equation (4.4) was utilized to calculate a cumulative 3x3 polarization ray trace matrix, a cumulative optical path length, and a propagation vector direction in air for all exiting rays. The PRTs and OPLs combined to form a PRT matrix that represented what a single initial incident ray encountered after passing through the compound retarder. For a normal incident ray, the PRT matrix is just a Jones matrix padded with the outer product of the **k** vector. The PRT matrix is converted into Mueller matrix form for performing other conventional calculations such as determining the retardance magnitude and orientation.

4.3.2.4.2 Off axis ray trace

Similar to the normal incident ray, the **k** vector was defined in spherical coordinates. The ray propagated through the retarder and resulted in 64 exiting rays with all the same **k** vector in air, but slightly displaced. These displaced rays combined in the same way performed in section 4.3.1, where rays splitting through a single retarder plate were shown. At the dummy surface following the retarder component the PRT and OPL components were added together in the same way as the on axis case.

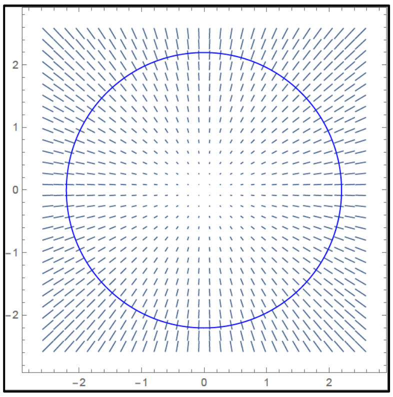

Figure 4.17: Grid of incident k vectors traced through the retarder. The length of the vectors represents the magnitude of the incidence angle. The circle encloses all angles of incidence that contribute to the center field point.

A grid of incident **k** vectors was created to trace through the DKIST retarder. Angularly the **k** vectors were evenly separated and sampled within the angular aperture for each field angle. Then the compound retarder's polarization properties were viewed as a function of angle of incidence. The figure below shows the amplitude of the Mueller matrix elements varied over ±3° angle of incidence for the ViSP SAR. A similar behavior was observed for the single plate retarder, where the largest decrease and increase in retardance was along the fast and slow axis of the retarder.

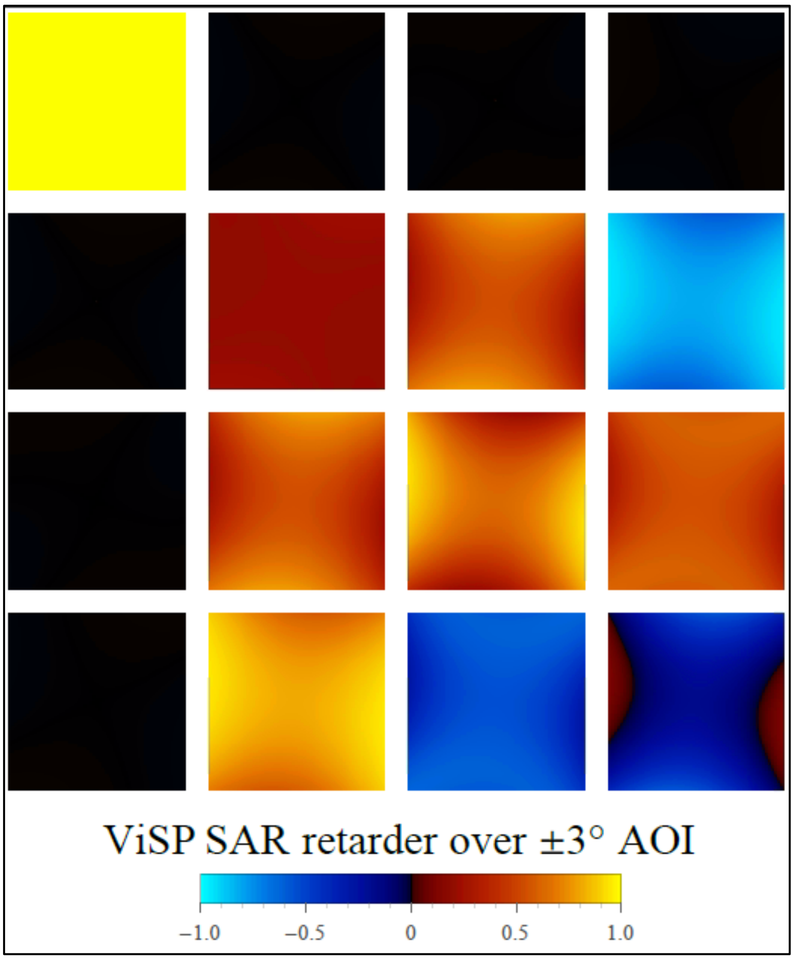

Figure 4.18: Mueller matrix of the ViSP SAR at 633.443 nm is shown over ±3° angle of incidence.

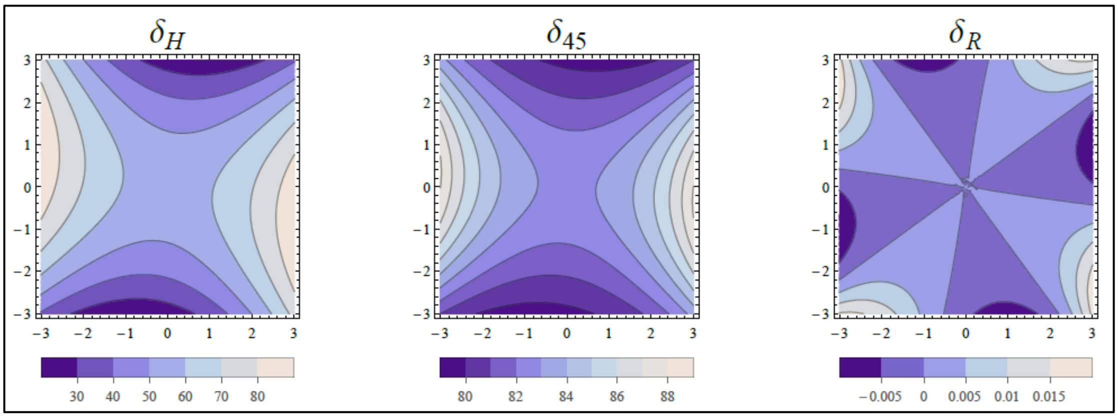

Figure 4.19: Retarder vector components for the ViSP SAR at 633.443 nm is shown over a ±3° angle of incidence.

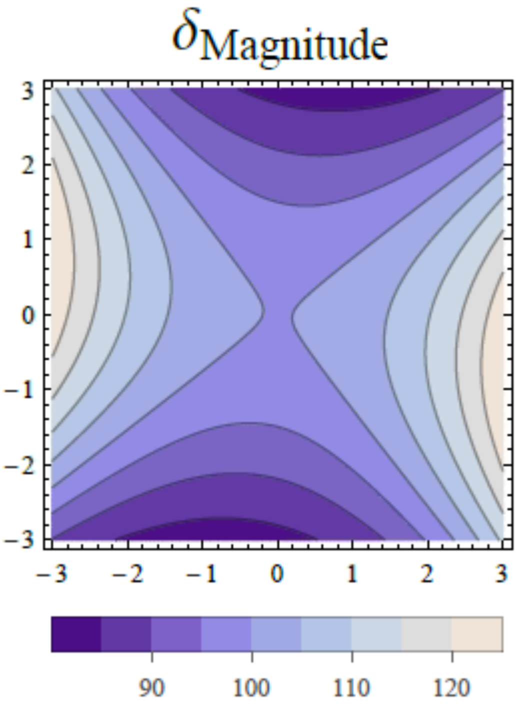

Figure 4.20: Retardance magnitude of the ViSP SAR at 633.443 nm is shown over a ±3° angle of incidence. The retardance magnitude varied more than 45° over a 6° AOI range.

4.4 Characterization over the field of view

In the previous section the DKIST SAR and PCMs were modeled and ray traced to determine their behavior over a grid of incidence angles. In this next section the angle of incidence ray trace data was utilized to better understand the retarders behavior in the non-collimated beam of the telescope. In section 4.3.2, the Mueller matrix of the ViSP SAR was shown over a ±3° angular range. The Mueller matrix at each incident angle within the converging beam must be combined to calculate the overall matrix representation of the retarder for each field point.

4.4.1 FOV on the calibration retarders

The primary mirror of the telescope collects the full 32 arc-minute angular diameter of the sun. The heat stop, which also acts as a field stop, is located in the top end optical assembly and limits the field of view of the telescope to 5 arc minutes. The beam is incident on the secondary mirror before converging to the Gregorian optical focus of the telescope. It is in this F/13 beam that the calibration retarders are located. The angular range of these ray bundles was determined with the F-number of the system. The relationship of the F-number to the numerical aperture is known as

$$\boldsymbol{F/\# \approx \frac{1}{2NA}} \tag{4.5}$$

And the numerical aperture is related to the half angle θ.

$$\boldsymbol{NA = nSin\theta} \tag{4.6}$$

The F/13 beam represents a 2.2° half angle cone centered on each field point. In other words, each colored circle in Figure 4.22 represents a ray bundle with maximum angle of 2.2° from the central ray.

In order to understand the spatial and angular distribution of the rays incident on the calibration retarder, the telescope's Zemax prescription was used to sample the 5 arc-minute field of view. Figure 4.21, shows the five field points that were traced as an example. One at the center field point and four maximum field points along x and y. Rays are shown passing through the calibration retarder and converging at the Gregorian optical focus.

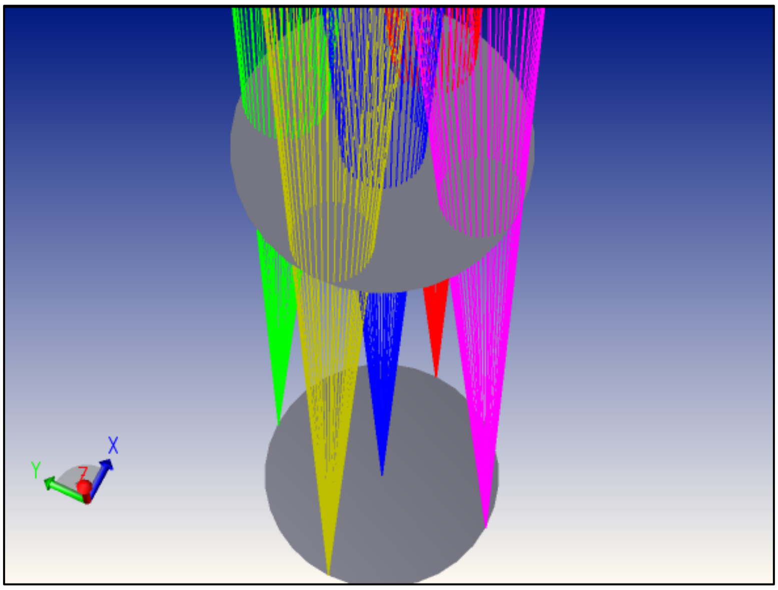

Figure 4.21: Rays incident on the calibration retarder location (top gray disk), converging to the Gregorian focus (bottom gray disk). These colored bundles show 5 field points, 1 center field and 4 at the extreme ends of the field of view.

The image on the left of Figure 4.22 is a footprint diagram from Zemax. It shows a spatial representation of the five beam bundles over the clear aperture of the calibration retarder. On the right is a vector diagram of the angles of incidence on the calibration retarder. The lengths of the vectors represent the increasing magnitude off axis and the orientation of the angle is represented by the orientation of the vector. Each colored circle encircles the angles incident on the retarder for a particular field point. Each field cone sees a slightly different cone of rays, or angular distribution.

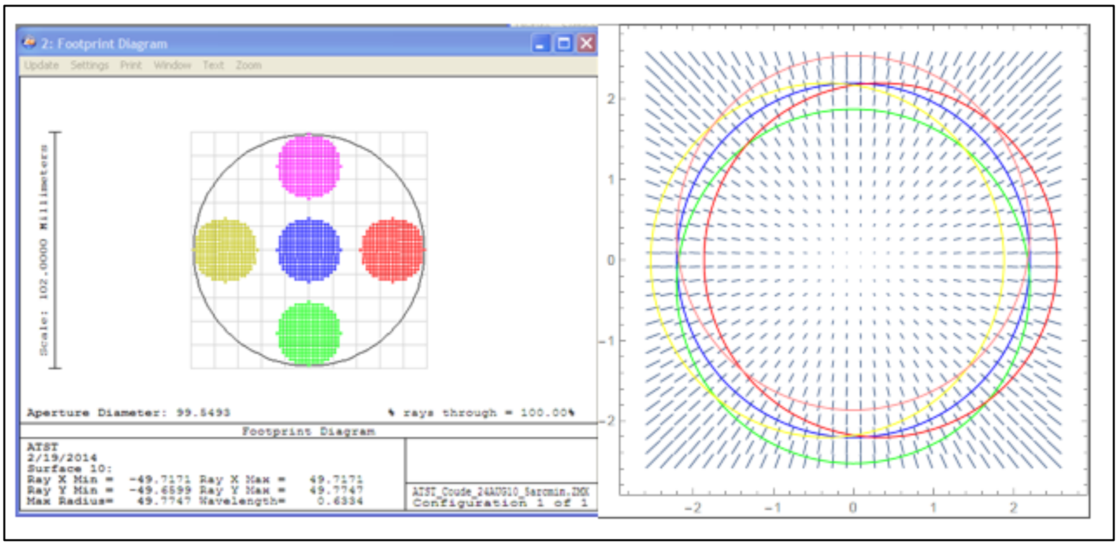

```
Aperture Diameter: 99.5493                          % rays through = 100.00%
                         Footprint Diagram
ATST
2/19/2014
Surface 10:
Ray X Min =  -49.7171 Ray X Max =   49.7171
Ray Y Min =  -49.6599 Ray Y Max =   49.7747      ATST_Coude_24AUG10_5arcmin.ZMX
Max Radius=   49.7747 Wavelength=    0.6334      Configuration 1 of 1
```

Figure 4.22: Left: Footprint plot for the same 5 field points on the calibration retarder. Right: Vector diagram of the angle of incidence over the calibration retarder. Five colored rings encircle the angular range of rays incident on the retarder to the corresponding 5 field points.

4.4.1.1 Obtaining the center ray angles with Zemax

The maximum angular range on the retarder from the center ray for each bundle of rays is 2.2°. The incidence angle of the center ray for each field point was determined. Field points were input into Zemax with the normalized field heights H_x and H_y. Rays were traced over the 5 arc minute field of view. Starting with the center field point, the rays for field $H_x = 0$, $H_y = 0$ were traced at several pupil locations: the center, and 8 points at the edges of the cone of rays. These pupil positions are shown in Table 4.2 along with their direction cosines and the angle from normal incidence.

A macro was written to output the direction cosines for the 5 field points at 9 pupil locations. This provided the angle of incidence information at the retarder location in the optical system. This information was extracted for maximum and the central field points so that the angular range of these cones of rays could be mapped.

Px	Py	X-cosine	Y-cosine	Z-Cosine	Angle
0	0	0	0	1	0
1	0	0.0382	0	0.9993	2.1897
0.7071	0.7071	0.0271	0.027	0.9993	2.1908
0	1	0	0.0382	0.9993	2.1913
-0.7071	0.7071	-0.0271	0.027	0.9993	2.1908
-1	0	-0.0382	0	0.9993	2.1897
-0.7071	-0.7071	-0.027	-0.027	0.9993	2.1886
0	-1	0	-0.0382	0.9993	2.1881
0.7071	-0.7071	0.027	-0.027	0.9993	2.1886

Table 4.2: Example of pupil coordinates of the cone of rays that focus at the central field point $H_x = 0, H_y = 0$. In Zemax the direction cosines for the central ray and rays at the perimeter of the cone were found.

4.4.2 Average Mueller matrix: the matrix representation of the retarder in a converging beam

The cone of rays that converge to the central field point is centered about a ray with normal incidence on the retarder. Off axis field points subtend an angle from normal incidence and the converging beam comes from a slightly skewed angle. The Mueller matrix calculated from the ray trace that represented the polarization properties of the calibration retarder for any given field point was an average of all Mueller matrices within each cone of rays.

The polarization ray trace performed in section 4.3.2 provided the Mueller matrices of the ViSP SAR at 633 nm over a 6° by 6° angular grid. Roughly 14,000 rays were sampled over a 3° angular range. A new grid that represented the angles of incidence centered on the field points, $(\psi_{center}, \chi_{center})$, was sampled evenly over the 5 arc-minute field of view. Each cone of rays had around 6000 rays spaced evenly over a grid. Equation (4.7) was the function used to select the Mueller matrices associated with each angle of incidence.

$$\sqrt{(\psi-\psi_{center})^2+(\chi-\chi_{center})^2}\leq 2.2^\circ \tag{4.7}$$

With Equation (4.8) these matrices were averaged for all incidence angles that lie in the f/13 beam for each field point.

$$\textbf{average Mueller matrix}=\left(\sum_{n=1}^{N} M_n\right)/N \tag{4.8}$$

Figure 4.23 shows the average Mueller matrix and encircled angular range used in the calculation of the Mueller matrix. For this example it was the Mueller matrix of the center field point.

$$\begin{pmatrix} 1. & 0. & 0. & 0. \\ 0. & 0.1958 & 0.5422 & -0.8139 \\ 0. & 0.5422 & 0.6297 & 0.5458 \\ 0. & 0.8139 & -0.5458 & -0.1744 \end{pmatrix}$$

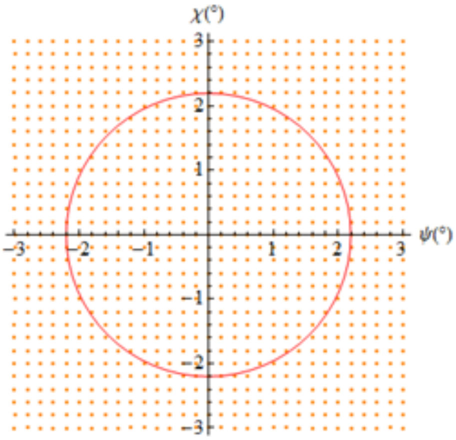

Figure 4.23: Average Mueller matrix for a cone of rays at 633 nm wavelength. A grid of angles and the encircled points contributing to the average Mueller matrix shown on the right.

Figure 4.2 shows the average Mueller matrix over a 5x5 arc-minute field of view for the ViSP SAR.

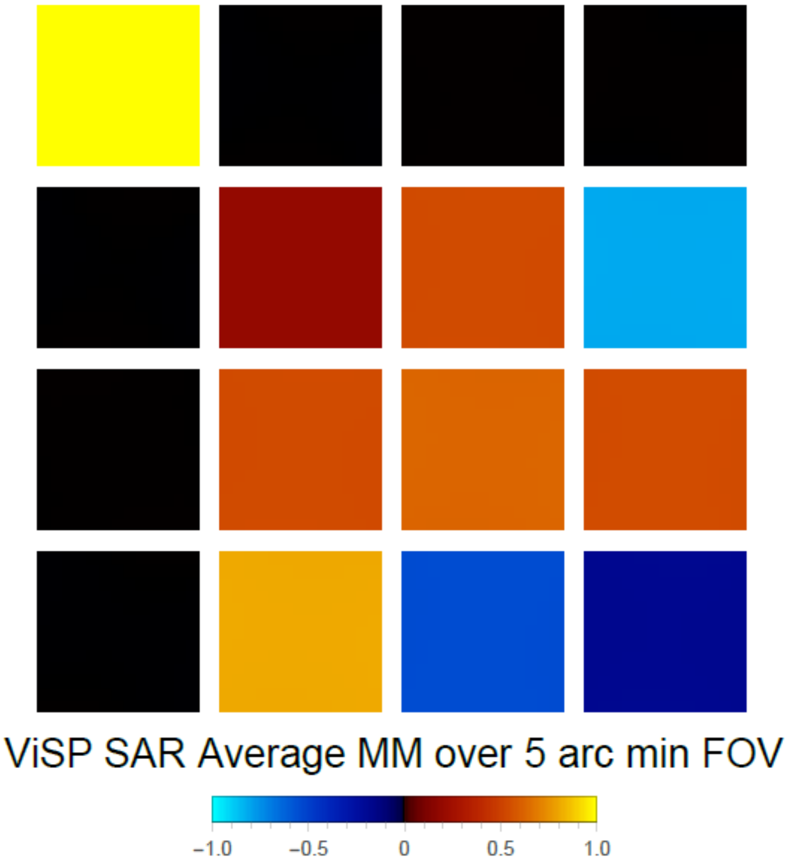

Figure 4.24: Average Mueller matrix of the ViSP SAR

It was difficult to see the difference in the Mueller matrix elements over the field of view. To show the difference between all field points and the center field point, the fit residuals were calculated and shown in Figure 4.25. Differences up to 3×10^{-3}were observed.

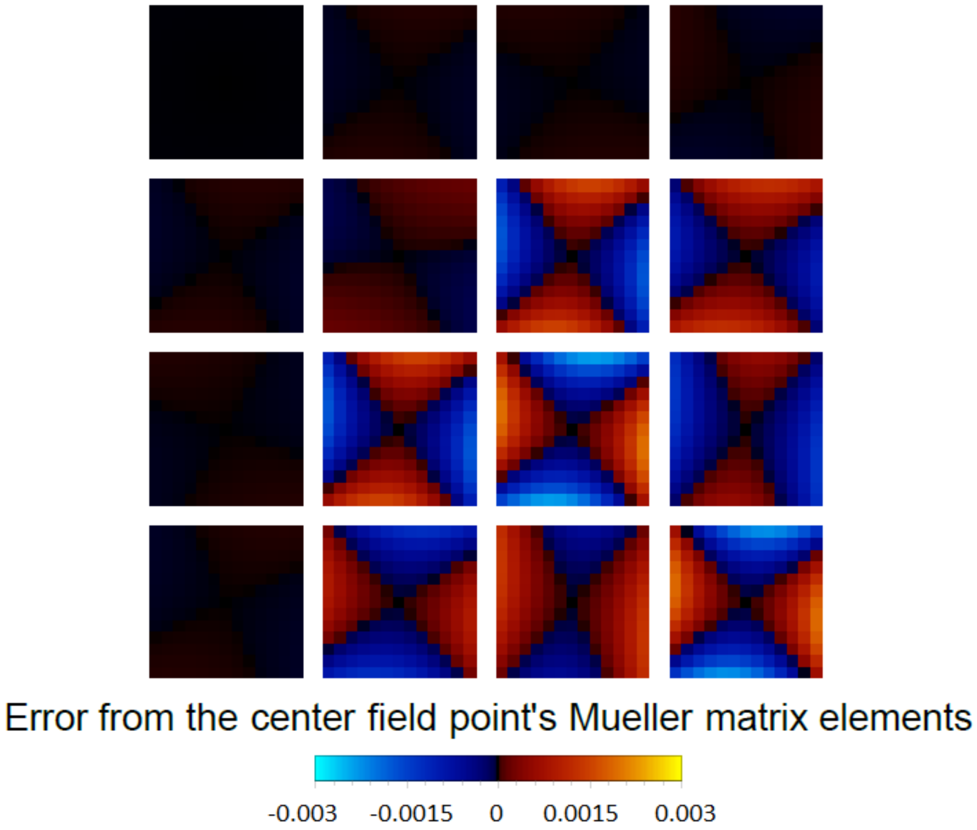

Figure 4.25: Variation across the field is shown with the difference between the average Mueller matrix at each field point and the center field point.

The average Mueller matrix needs to be parameterized in order to perform the telescope's calibration technique. Each element or group of elements in the telescope system are represented by a Mueller matrix (D F Elmore, 2013). In an ideal case, the Mueller matrix would fit to a linear retarder $LR[\delta, \theta]$, where only two parameters exist, retardance magnitude δ, and orientation θ. Errors in the fit are larger than those allowed in the error budget allocation, meaning the fit is not accurate enough to the model the retarder for the DKIST. Fitting the average Mueller matrices over the field of view are discussed in the next chapter.

5 MUELLER MATRIX DECOMPOSITION

5.1 Introduction

In the previous chapter the DKIST SAR retarder components were modeled and a polarization ray trace was performed. This chapter only discusses the fit and decomposition of the SARs and not the PCMs, because the SAR Mueller matrix needs to be fit for in the calibration technique and the PCM doesn't. Instead the PCM polarization properties become a part of the Modulation matrix and are not fit for as an independent Mueller matrix. Rays were traced over the angles of incidence for the field of view of each retarder and an average Mueller matrix calculated for each field point. The average Mueller matrix was not easily parameterized. When the angles of incidence are large enough, averaging all of them for a particular field point introduced depolarization and the Mueller matrix no longer resembled an ideal linear or elliptical retarder.

This chapter describes the exploration of different methods to parameterize the average Mueller matrices in order to develop a model with the fewest number of parameters to fit. This model must also fit the averaged Mueller matrices to within the error budget. First, the averaged Mueller matrices were fit to an ideal linear retarder. Then, decomposition methods explored in this chapter were investigated. These included the Lu-Chipman decomposition and the Symmetric decomposition.

5.2 Fit the average Mueller matrix

Equation (5.1) is the normalized average Mueller matrix for the center field point of the ViSP SAR. The normalized average Mueller matrix for all field points is shown in Figure 4.24.

$$\begin{pmatrix} 1 & 0 & 0 & 0 \\ 0 & 0.1958 & 0.5422 & -0.8139 \\ 0 & 0.5422 & 0.6297 & 0.5458 \\ 0 & 0.8139 & -0.5458 & -0.1744 \end{pmatrix} \tag{5.1}$$

Fits on the average Mueller matrix were performed over the field of view and for each fit the residual errors were calculated and shown.

5.2.1 Ideal linear retarder

First, the Mueller matrix of the center field point was fit to the ideal linear retarder model. Two parameters were fit for, δ and θ, in the end the fit residual error was

$$\begin{pmatrix} 0 & 0 & 0 & 0 \\ 0 & -0.0026 & 0.0019 & -0.0026 \\ 0 & 0.0019 & 0.0034 & 0.0048 \\ 0 & 0.0026 & -0.0048 & 0.0008 \end{pmatrix} \tag{5.2}$$

The fit was used for all field points and the residual error is shown in Figure 5.1.

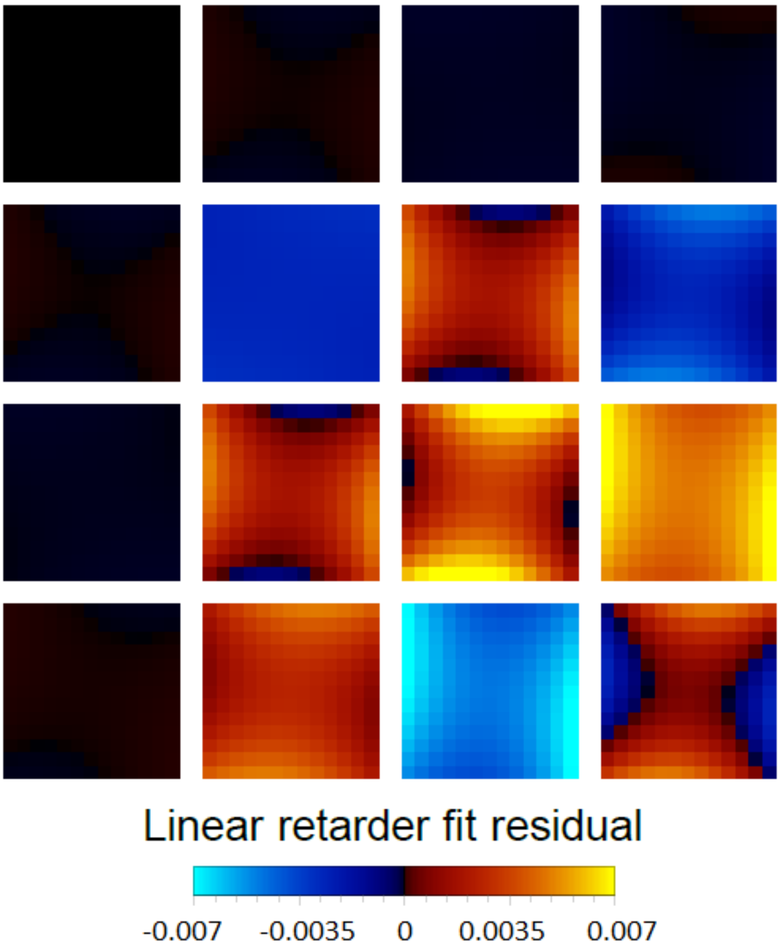

Figure 5.1: Residual error after subtracting the average Mueller matrices with a single linear retarder model.

Figure 5.2 shows the fit residual after the Mueller matrix was fit with an ideal linear retarder model for each field position. Ultimately this figure showed that even if we were able to fit every point with it’s own retardance and orientation, a residual error of up to 0.006 is observed.

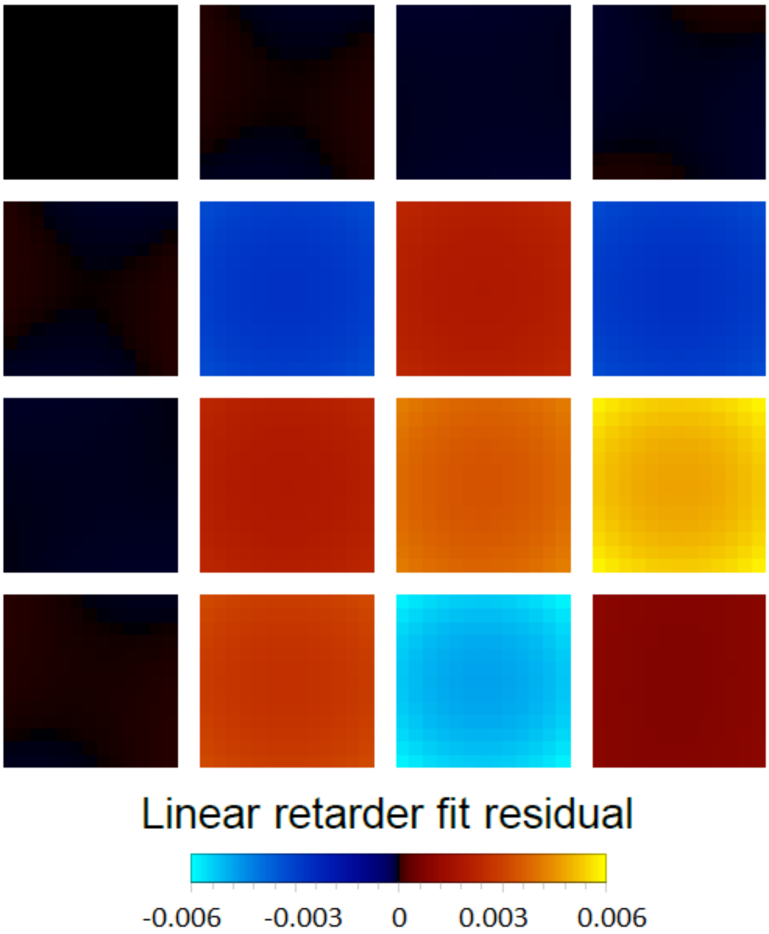

Figure 5.2: Difference between the fit linear retarder and the average Mueller matrices.

5.2.2 Mueller matrix decomposition

Mueller matrix decomposition provides a method to break down a single Mueller matrix into a series of Mueller matrices. Depending on the decomposition method, these matrices can be modeled as physically realizable Mueller matrices. One can then fit the matrices to a reduced number of parameters. Having a Mueller matrix model for the calibration retarders with a minimum number of parameters is the ultimate goal for polarization calibration of the telescope.

The properties of the retarders varied with incident angle, so when the matrices were averaged for each field point depolarization was introduced. The decomposition methods tested were the Lu-Chipman decomposition and the Symmetric decomposition. Both theoretically fit the average Mueller matrix with errors below 10^{-6}. The Lu-Chipman decomposition resulted in a non-diagonal depolarization matrix, whereas the symmetric decomposition resulted in a diagonal depolarization matrix. The symmetric decomposition was chosen since, for this type of optical component, it provided an accurate description of the retarder behavior with a minimum number of parameters.

5.2.2.1 Lu-Chipman decomposition

Lu-Chipman Mueller matrix decomposition (Lu & Chipman, 1996) decomposes a single Mueller matrix into a depolarizer, retarder and diattenuator. The order of matrix multiplication is as follows,

$$\boldsymbol{M}_{\boldsymbol{depolarizer}} \cdot \boldsymbol{M}_{\boldsymbol{retarder}} \cdot \boldsymbol{M}_{\boldsymbol{diattenuator}} \tag{5.3}$$

This decomposition method completely fit the average Mueller matrix. When recombined then subtracted from the average Mueller matrix there was zero error in all matrix elements. Below are the depolarizer, retarder and diattenuator matrices respectively for the center field point.

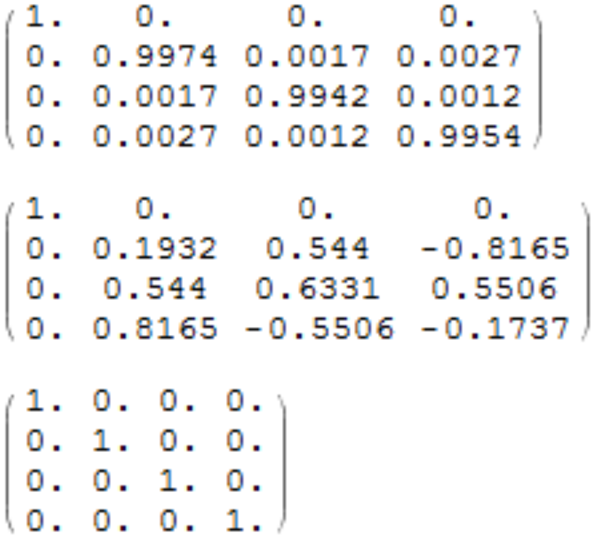

$$\begin{pmatrix} 1. & 0. & 0. & 0. \\ 0. & 0.9974 & 0.0017 & 0.0027 \\ 0. & 0.0017 & 0.9942 & 0.0012 \\ 0. & 0.0027 & 0.0012 & 0.9954 \end{pmatrix}$$

$$\begin{pmatrix} 1. & 0. & 0. & 0. \\ 0. & 0.1932 & 0.544 & -0.8165 \\ 0. & 0.544 & 0.6331 & 0.5506 \\ 0. & 0.8165 & -0.5506 & -0.1737 \end{pmatrix} \tag{5.4}$$

$$\begin{pmatrix} 1. & 0. & 0. & 0. \\ 0. & 1. & 0. & 0. \\ 0. & 0. & 1. & 0. \\ 0. & 0. & 0. & 1. \end{pmatrix}$$

The depolarizer Mueller matrix diagonal elements differed in the third decimal place and the off-diagonal elements were symmetric. All together it 6 parameters are required to model this matrix as shown in Equation (5.5). The retarder matrix fit to equation (4.1), the linear retarder model with a fit residual of less than 10^{-8}. The diattenuator was the identity matrix so no fit parameter was necessary. In total, 8 parameters were required to fit these decomposed matrices.

$$\boldsymbol{M_{depolarizer}} = \begin{pmatrix} \mathbf{1} & \mathbf{0} & \mathbf{0} & \mathbf{0} \\ \mathbf{0} & \mathbf{a} & \mathbf{d} & \mathbf{e} \\ \mathbf{0} & \mathbf{d} & \mathbf{b} & \mathbf{f} \\ \mathbf{0} & \mathbf{e} & \mathbf{f} & \mathbf{c} \end{pmatrix} \tag{5.5}$$

5.2.2.2 Symmetric decomposition

The Symmetric Mueller matrix decomposition (Ossikovski, 2009) resulted in a diagonal depolarizer matrix between a pair of retarders and diattenuators, as shown in equation (5.6).

$$\boldsymbol{M_{D2}.M_{R2}.M_{depol}.M_{R1}.M_{D1}} \tag{5.6}$$

This decomposition method also completely fit the average Mueller matrix. Below the decomposed matrices for the center field point are shown: diattenuator, retarder, depolarizer, retarder and diattenuator respectively.

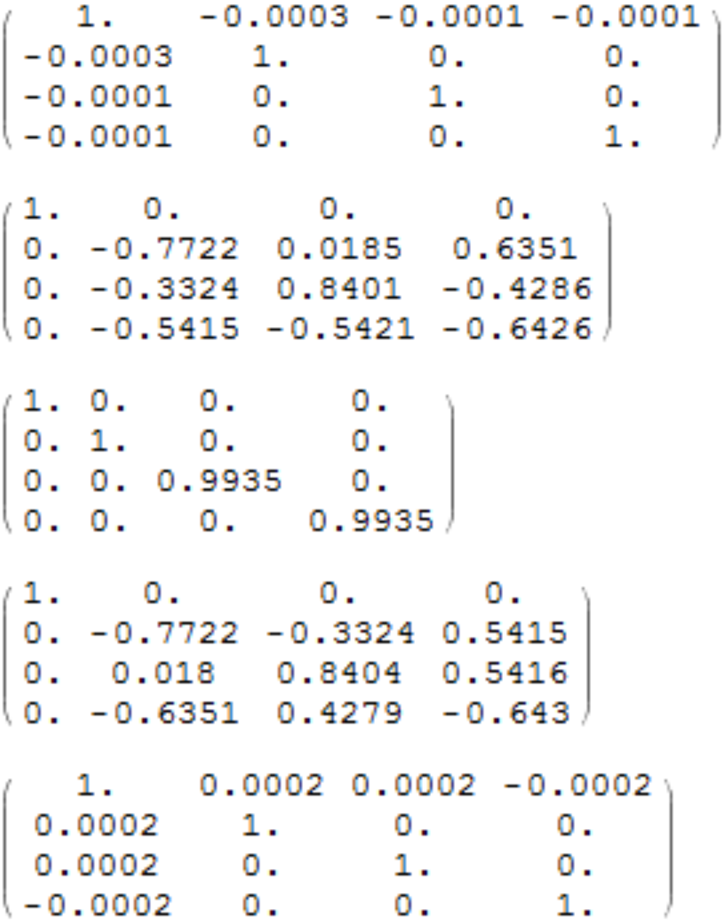

$$\begin{pmatrix} 1. & -0.0003 & -0.0001 & -0.0001 \\ -0.0003 & 1. & 0. & 0. \\ -0.0001 & 0. & 1. & 0. \\ -0.0001 & 0. & 0. & 1. \end{pmatrix}$$

$$\begin{pmatrix} 1. & 0. & 0. & 0. \\ 0. & -0.7722 & 0.0185 & 0.6351 \\ 0. & -0.3324 & 0.8401 & -0.4286 \\ 0. & -0.5415 & -0.5421 & -0.6426 \end{pmatrix}$$

$$\begin{pmatrix} 1. & 0. & 0. & 0. \\ 0. & 1. & 0. & 0. \\ 0. & 0. & 0.9935 & 0. \\ 0. & 0. & 0. & 0.9935 \end{pmatrix} \qquad (5.7)$$

$$\begin{pmatrix} 1. & 0. & 0. & 0. \\ 0. & -0.7722 & -0.3324 & 0.5415 \\ 0. & 0.018 & 0.8404 & 0.5416 \\ 0. & -0.6351 & 0.4279 & -0.643 \end{pmatrix}$$

$$\begin{pmatrix} 1. & 0.0002 & 0.0002 & -0.0002 \\ 0.0002 & 1. & 0. & 0. \\ 0.0002 & 0. & 1. & 0. \\ -0.0002 & 0. & 0. & 1. \end{pmatrix}$$

The depolarizer Mueller matrix only had diagonal values, a single parameter fit the diagonal values that were not unity. The retarder pair fit to an elliptical retarder model, with equal magnitude but opposite sign for the circular retardance parameter.

$$\boldsymbol{ER}[\{\boldsymbol{r_H}, \boldsymbol{r_{45}}, \boldsymbol{r_R}\}] =$$

$$\begin{pmatrix} 1 & 0 & 0 & 0 \\ 0 & \frac{r_H{}^2}{d^2} + \left(\frac{r_{45}{}^2 + r_R{}^2}{d^2}\right)\cos d & \frac{r_H r_{45}}{d^2}(1-\cos d) + r_R \sin d & \frac{r_H r_R}{d^2}(1-\cos d) - r_{45}\sin d \\ 0 & \frac{r_H r_{45}}{d^2}(1-\cos d) - r_R \sin d & \frac{r_{45}{}^2}{d^2} + \left(\frac{r_R{}^2 + r_H{}^2}{d^2}\right)\cos d & \frac{r_{45} r_R}{d^2}(1-\cos d) + r_H \sin d \\ 0 & \frac{r_H r_R}{d^2}(1-\cos d) + r_{45}\sin d & \frac{r_{45} r_R}{d^2}(1-\cos d) - r_H \sin d & \frac{r_R{}^2}{d^2} + \left(\frac{r_H{}^2 + r_{45}{}^2}{d^2}\right)\cos d \end{pmatrix} \qquad (5.8)$$

The elliptical retarder model has 3 parameters, the 3x1 elements of the retarder vector, $\{r_H, r_{45}, r_R\}$. $d = \sqrt{Abs[r_H]^2 + Abs[r_{45}]^2 + Abs[r_R]^2}$, is the norm of the retarder vector.

The diattenuator matrices were eliminated from the model, as they were not necessary to recover the average Mueller matrix. With the remaining three matrices in series, $M_{R2}.M_{depol}.M_{R1}$, the Mueller matrix was recovered with errors of order of magnitude 10^{-6} or less.

$$\boldsymbol{M_{depol} = DiagonalMatrix[\{1, 1, a, a\}]} \tag{5.9}$$

$$\boldsymbol{M_{R1} = ER[\{r_H, r_{45}, -r_R\}]} \tag{5.10}$$

$$\boldsymbol{M_{R2} = ER[\{r_H, r_{45}, r_R\}]} \tag{5.11}$$

With the symmetric decomposition model and 4 parameters the center field point average Mueller matrix was recovered. Fit residual is shown below, where errors of order of magnitude 10^{-6} or less are not shown.

$$\begin{pmatrix} \mathbf{0} & \mathbf{0} & \mathbf{0} & \mathbf{0} \\ \mathbf{0} & \mathbf{-5\times10^{-5}} & \mathbf{0} & \mathbf{-4\times10^{-5}} \\ \mathbf{0} & \mathbf{0} & \mathbf{-5\times10^{-5}} & \mathbf{0} \\ \mathbf{0} & \mathbf{4\times10^{-5}} & \mathbf{0} & \mathbf{1\times10^{-5}} \end{pmatrix} \tag{5.12}$$

The fit parameters $a = 0.9935, r_H = 0.2282, r_{45} = -2.364\ and\ r_R = 0.7045$ are rounded to the fourth decimal place.

5.2.2.3 Conclusion

As shown above the Lu-chipman decomposition had zero diattenuation and the symmetric decomposition had terms of 0.003 or less. The symmetric decomposition method had two diattenuation matrices on the outside of the decomposition which puts the diattenuation terms to second order (squares them) and including those terms in the fit changed the result to less than an order of magnitude of 10^{-6}.

5.2.3 Fit the average Mueller matrix over FOV with the Symmetric decomposition method

Fitting the single central field only took four parameters; additional parameters were necessary to fit the matrix as a function of field of view. The fitted values of the retarder vector components over the field of view are shown below.

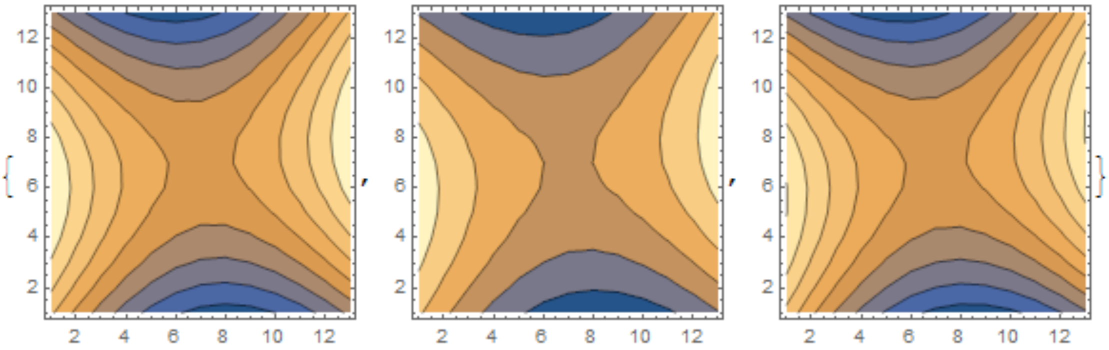

rH r45 rR

Figure 5.3: Fit values of the retarder vector components over the field of view.

Each component is of the functional form $\boldsymbol{a}(\chi^2 - \psi^2) + \boldsymbol{b}2\chi\psi + \boldsymbol{c}$, where χ and ψ represent the field angles, and $a, b, and\ c$ are fit coefficients. The depolarizer parameter did not vary greatly over field of view; therefore a single value averaged over the field of view was used. Figure 5.4 shows the difference between the average Mueller matrix and the fitted series of matrices.

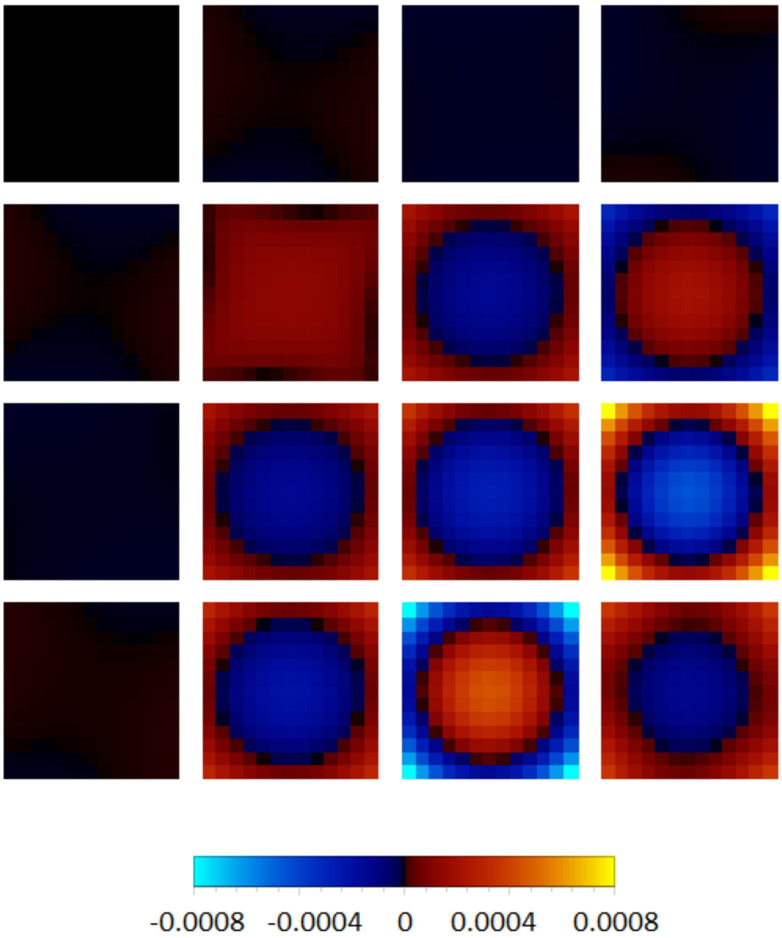

Figure 5.4: Difference between the 10 parameter symmetric decomposition fit and the average Mueller matrices.

Three parameters per retarder vector component and a single depolarizer parameter resulted in 10 total parameters. Using a 10-parameter fit to the series of matrices $M_{R2}.M_{depol}.M_{R1}$ the average Mueller matrices were fit for over a 5 arc-minute field of view for the ViSP SAR. The fit error was on the order of magnitude of 10^{-4} or less.

5.3 Conclusion

The polarization properties of the DKIST calibration optics must be well known in order to achieve the highest precision calibration of the telescope. It was found that an ideal linear retarder Mueller matrix was an insufficient model of the calibration retarder because the averaging over the converging rays for each field point produce depolarization effects. The errors over field of view were of order of magnitude 10^{-3}, larger than what was acceptable in the polarimetric error budget.

Mueller matrix decomposition techniques were explored and the Symmetric decomposition method provided a 10 parameter fit of the retarder over field of view that resulted in errors with the order of magnitude of 10^{-4} or less.

6 ACCEPTANCE TESTING OF THE DKIST RETARDERS WITH THE NLSP

6.1 Introduction

The DKIST retarders play a critical role in the polarization measurement capabilities of the telescope. These elements are of a novel design, therefore they must be tested and the performance verified against the DKIST project requirements. The NSO Laboratory Spectro-Polarimeter (NLSP) is designed to perform validation measurements of the retarders as they are fabricated. The NLSP is easily reconfigured into three basic setups, each of which provides different information that supports the characterization of the DKIST retarders. Validation test measurements of the retarder properties are performed at room temperature. There is no thermal requirement in the contract with Meadowlark, and therefore thermal stability is not part of the validation process. Thermal testing and angle of incidence measurements will be done after the acceptance tests discussed in this chapter.

6.2 NSO Laboratory Spectro-Polarimeter

Three major components comprise the NLSP: a broadband light source, a spectrograph, and a polarimeter. A 75-Watt Xenon arc lamp with a F/4.5 reflector is used as a broadband light source to cover the spectral range 400 nm to 2000 nm. The spectrograph consisted of an entrance and exit slit, a rotating grating and a spherical mirror all housed in a refurbished telescope spectrograph instrument box. Two different gratings and detectors were utilized to cover the full spectral range. The polarimeter components were made up of both polarization state generator and analyzer optics. On the polarization state generator side, a rotating linear retarder followed by a rotating retarder provided known input polarization states into a sample. A rotating retarder modulator followed by a fixed linear polarizer provided the polarization state analyzer optics following the sample. The following subsections explain the configurations of the NLSP that are used in the acceptance testing of the DKIST retarders.

6.2.1 Channeled spectra

Channeled spectral measurements of the sample retarder between crossed and aligned polarizers are shown in Figure 6.1. The channeled spectra measurement is used as a quick check on the sample retarder behavior. The sample retarder between polarizers can be easily modeled and compared with the measured results. The convenient point to this measurement is the entire spectral range of the spectrograph can be covered much faster than the other configurations. Neither the sample retarder or polarimeter components are moving during the spectral scan.

Expected measurement should show a smooth, slowly varying curve over the wavelength range. If the measurements reveal high frequency oscillations an error in the assembly is immediately recognized. Oscillations only occur due to rapidly varying retardance as a function of wavelength. This should not be the case for any of the designed retarders.

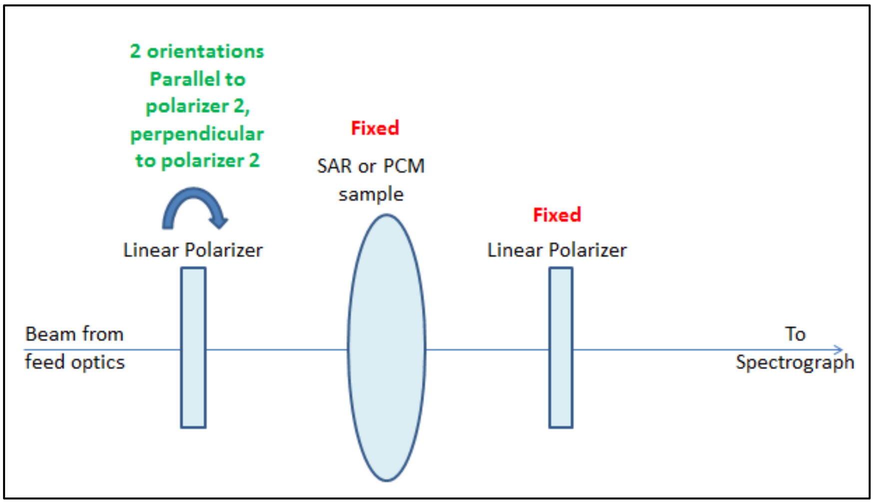

Figure 6.1: Channeled spectra measurement configuration.

6.2.2 Rotating retarder

Figure 6.2 shows the second measurement configuration, a rotating sample retarder between crossed or aligned polarizers. Only one wavelength measurement can be performed at a time. This measurement configuration provides a quick check of the linear retardance magnitude and determines the fast axis of the retarder. Circular retardance cannot be determined and is therefore only useful for testing the SARs and not the PCMs. Another limitation is if the retardance magnitude varies too quickly with wavelength the data is not very useful. As an example, if there are several waves of retardance within a short wavelength range it would require high spectral sampling or else one cannot tell where the retardance wraps over the modulo 2π.

Rotating retarder does provide information on the fast and slow axis orientations as a function of wavelength, magnitude of the oscillation in a linear retarder provides the linear retardance magnitude, but will mask any circular retardance information.

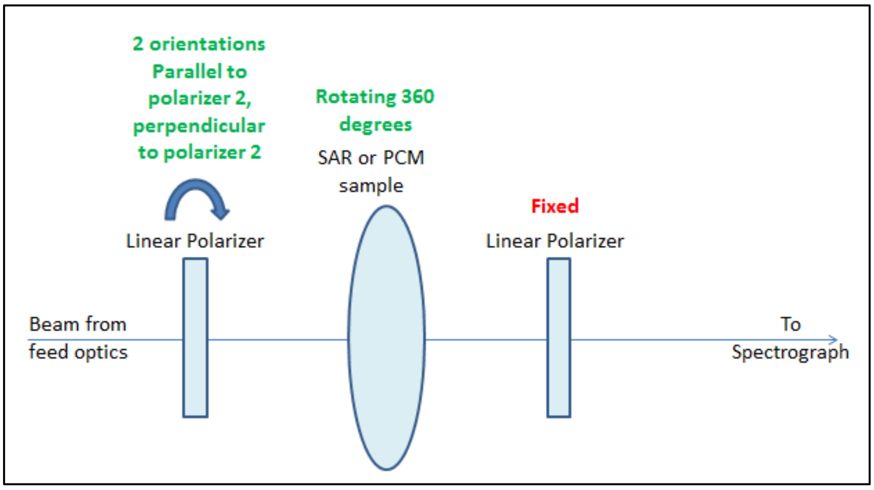

Figure 6.2: Rotating retarder measurement configuration.

6.2.3 Mueller matrix measurements

Ideally, Mueller matrix measurements provide the most information about the polarization properties of the sample. However, due to the limitations of the NLSP these measurements are lengthy and only provide a single wavelength at a time. It was best if major clocking errors were determined in one of the first two configurations, which can be performed faster before moving on to these measurements.

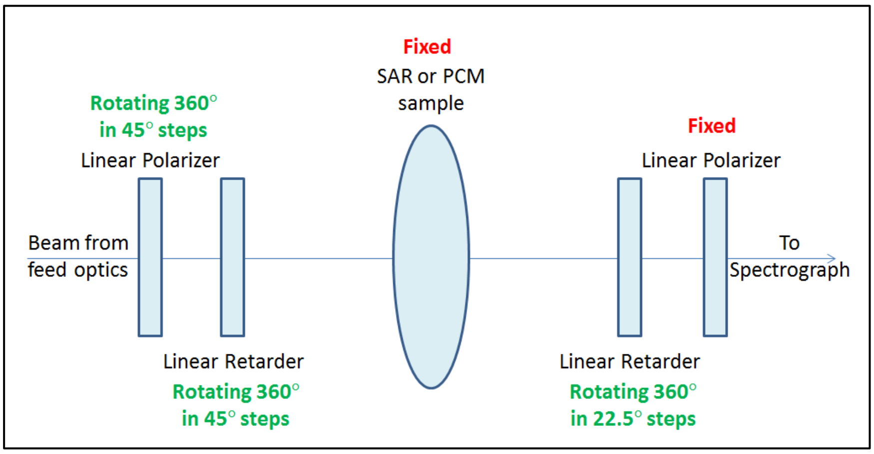

Figure 6.3: Mueller matrix measurement configuration.

6.3 Retarder validation test

6.3.1 Meadowlark measurements

Meadowlark Inc. will provide the final fabricated and mounted retarder components. It is the DKIST project's responsibility to perform validation tests to ensure the retarders perform as designed. The contract with NSO states that Meadowlark will provide measurements of retardance of the crossed pairs of plates at two wavelengths. This information is a confirmation of the polishing accuracy of the individual plates. Table 6.1 contains retardance information of the "C" compound retarder pairs and Table 6.2 contains retardance information of the "D" compound retarder pairs. These numbers were provided by Meadowlark in their 5th and 7th progress reports respectively.

Pair serial number	**C01**	**C02**	**C03**
Component serial numbers	CB1/CS1	CB4/CS2	CB5/CS4
Average retardance	0.997 waves @ 633.443nm, 0.412 waves @ 1449.033nm	0.996 waves @ 633.443nm, 0.412 waves @ 1449.033nm	0.996 waves @ 633.443nm, 0.412 waves @ 1449.033nm
Uniformity standard deviation	0.002 waves @ 633.443nm	0.001 waves @ 633.443nm	0.002 waves @ 633.443nm
Maximum deviation from goal (1 wave @ 633.443nm), at locations 1-5	0.005 waves @ 633.443nm	0.005 waves @ 633.443nm	0.007 waves @ 633.443nm

Table 6.1: C compound retarder.

Pair SN	**D01**	**D02**	**D03**
Component SN's	DB1/DS3	DB3/DS4	DB2/DS2
Average retardance	0.686 waves @ 633.443 nm, 0.282 waves @ 1449.033 nm	0.682 waves @ 633.443 nm, 0.282 waves @ 1449.033 nm	0.686 waves @ 633.443 nm, 0.282 waves @ 1449.033 nm
Uniformity standard deviation	0.002 waves @ 633.443 nm	0.002 waves @ 633.443 nm	0.0005 waves @ 633.443 nm
Maximum deviation from goal (0.683 waves @ 633.443 nm) at locations 1-5	0.005 waves @ 633.443 nm	0.004 waves @ 633.443 nm	0.004 waves @ 633.443 nm

Table 6.2: D compound retarder.

C and D pairs were used in the DL-NIRSP assemblies. The average retardance values were well within the required maximum deviation of 0.01 waves. This information is very important for the acceptance testing. If the retardance values are known then the main error to look for are errors in the clocking of the plates.

6.3.2 Summary of DL-NIRSP prototype assembly measurements

In March of 2015 prototype retarder assemblies were provided by Meadowlark to understand the feasibility of performing the full assembly acceptance tests with the NLSP. These assembled retarders had obvious AR coating issues and needed to be disassembled to strip and recoat, but it provided a good opportunity to shake out the acceptance test plan. The DL-NIRSP PCM and SAR retarders were tested and clocking errors were discovered.

6.3.2.1 DL-NIRSP SAR

6.3.2.1.1 Channeled spectra measurements

The channeled spectra measurements immediately showed that there was a problem in the SAR assembly. High frequency oscillations were observed in the intensity versus wavelength data, as shown in Figure 6.4. In comparison to the expected performance curves shown in blue and orange, there was a definite mismatch. No further measurements were required to show that a clocking error had definitely occurred.

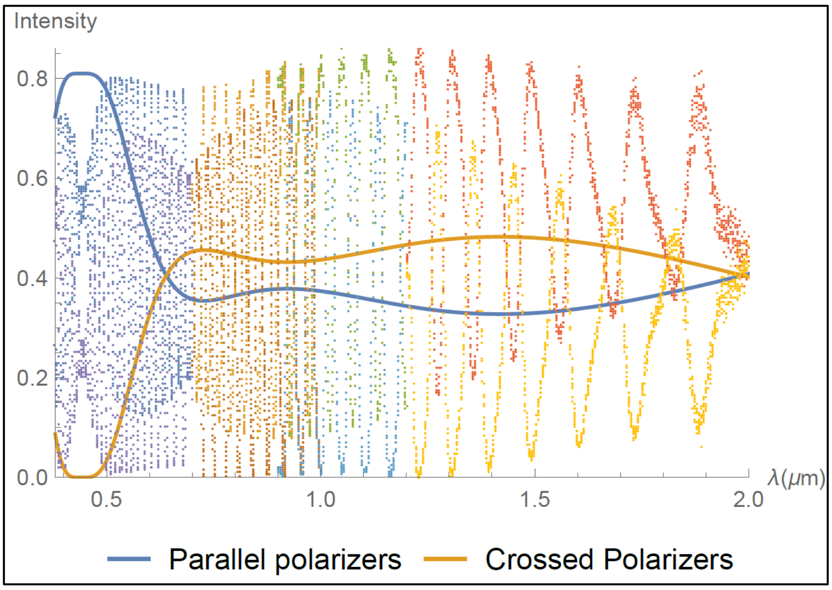

Figure 6.4: Simulated (lines) and measured (points) DL-NIRSP SAR transmission between parallel and crossed polarizers.

6.3.2.2 DL-NIRSP PCM

6.3.2.2.1 Channeled spectra

The channeled spectra measurements of the PCM showed promising results, the data followed the curvature of the expected intensity versus wavelength performance. It was not clear if the modulation efficiency had been met. In order to determine that the Mueller matrix measurements are needed. Since there was no obvious sign of error based on this measurement, then the next step was to move forward with Mueller matrix measurements.

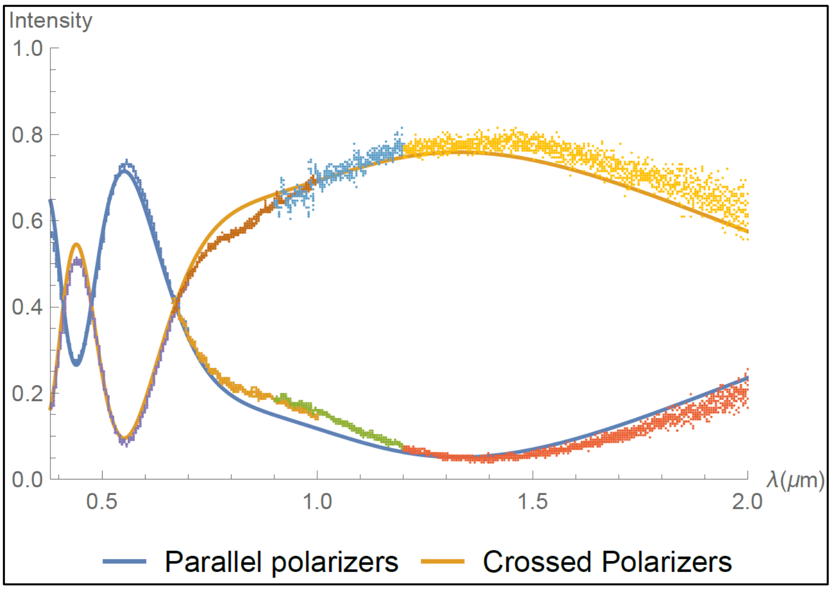

Figure 6.5: Simulated and measured DL-NIRSP PCM transmission between parallel and crossed polarizers.

6.3.2.2.2 Rotating retarder measurements

This measurement configuration was skipped because it was known that the PCMs are elliptical retarders and not linear retarders. Determining the linear retardance magnitude and orientation did not provide useful information for the validation testing of these parts.

6.3.2.2.3 Mueller matrix measurements

Measurements were performed over the wavelength range of the NLSP. Figure 6.6 shows the Mueller matrix for measurements at 24 wavelengths (blue dots) from 400 nm to 2000 nm. The red curve is the modeled performance of the designed PCM as a function of wavelength. It is clearly seen that the data does not match the predicted performance.

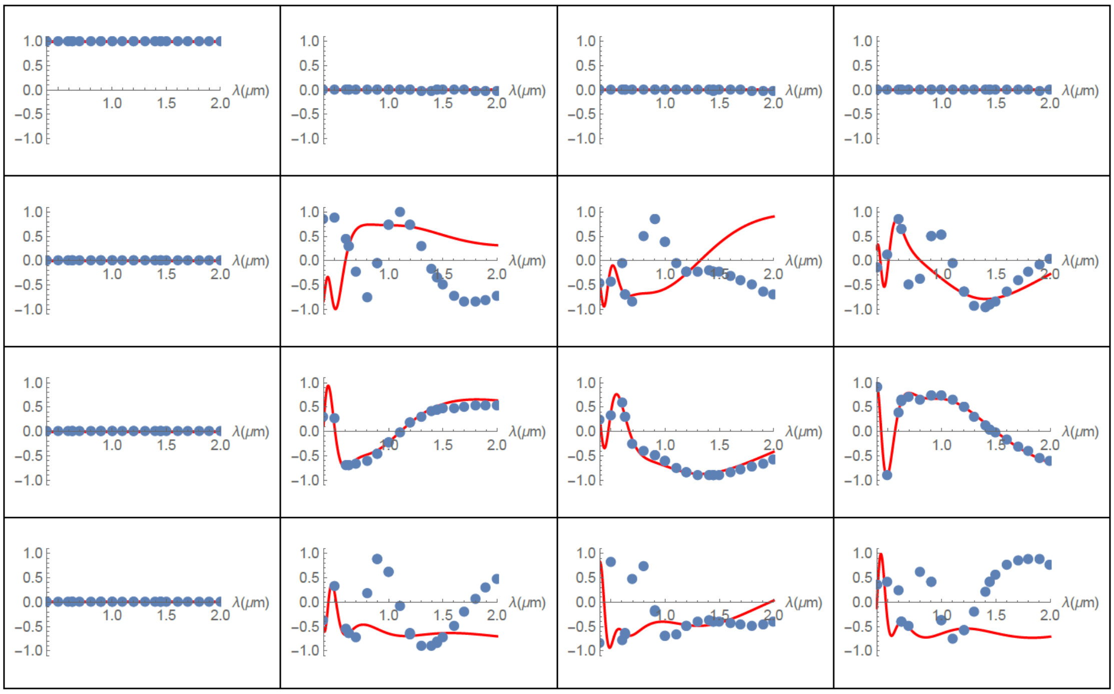

Figure 6.6: Simulated and measured Mueller matrix of the DL-NIRSP PCM from 400 nm to 2000 nm.

Recall Equation (4.1) for a linear retarder. It is a function of the retardance, δ, and the fast axis orientation, θ. Each C and D pairs had two plates made of A-cut quartz crystal, with fast axes crossed. This clocking between the pair of plates reduces the two retarders into a single linear retarder, where retardance, $\delta_{C\,pair} = \delta_{\mathrm{C}} - \delta_{\mathrm{bias}}$, is the difference between the retardance of the two individual plates. The quartz crystal birefringence, $\Delta n[\lambda]$, measured as a function of wavelength in Section 2.2.2.2 is also used to provide the wavelength dependence of the retardance. Utilizing the information reported from the vendor in Section 6.3.1, it is known that the C and D pairs have measured retardance at two wavelengths that show the plates have been polished to the correct thickness. Equation (6.1) below provides the wavelength dependent form that is substituted into the linear retarder function.

$$\boldsymbol{\delta}_{C\,pair} = \boldsymbol{\delta}_{\mathrm{C}} - \boldsymbol{\delta}_{\mathrm{bias}} = \frac{2\pi}{\lambda}\Delta n[\lambda](t_{\mathrm{C}} - t_{\mathrm{bias}}) \tag{6.1}$$

The six linear retarders are now reduced to Equation (6.2), a series of three linear retarders representing each of the plate pairs. The remaining variables to solve for are the orientation angles, θ_1, θ_2, and θ_3 of each of the plate pairs.

$$\mathrm{LR}[\delta_{C\,pair}, \theta_3].\mathrm{LR}[\delta_{D\,pair}, \theta_2].\mathrm{LR}[\delta_{C\,pair}, \theta_1] \tag{6.2}$$

A fitting routine was used in Mathematica and it was determined that θ_1 and θ_2 were the correct clocking angles, but θ_3 was rotated by 90°. The resulting fitted curve is shown in red overlapping the measured Mueller matrix data points in blue in Figure 6.7.

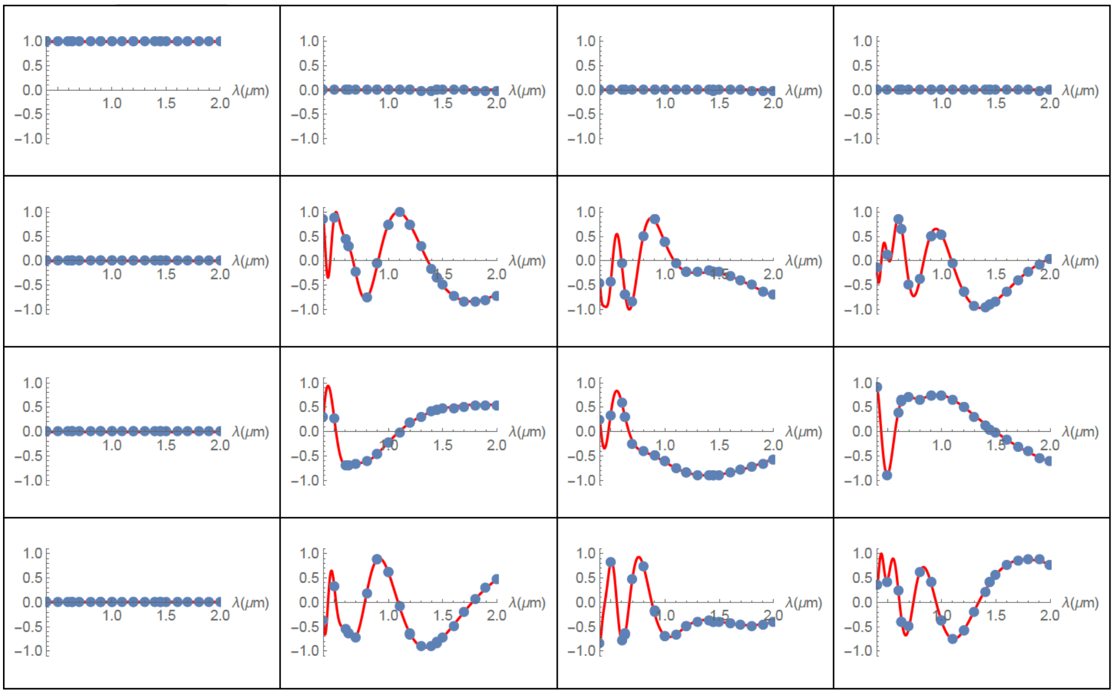

Figure 6.7: Fitted model (line) and measured data (points) Mueller matrix of the DL-NIRSP PCM from 400 nm to 2000 nm.

Clearly, the measured data shows the PCM does not meet the design Mueller matrix. Figure 6.8 shows how much this clocking error results in a large decrease in linear modulation efficiency, and a small decrease in the circular modulation efficiency.

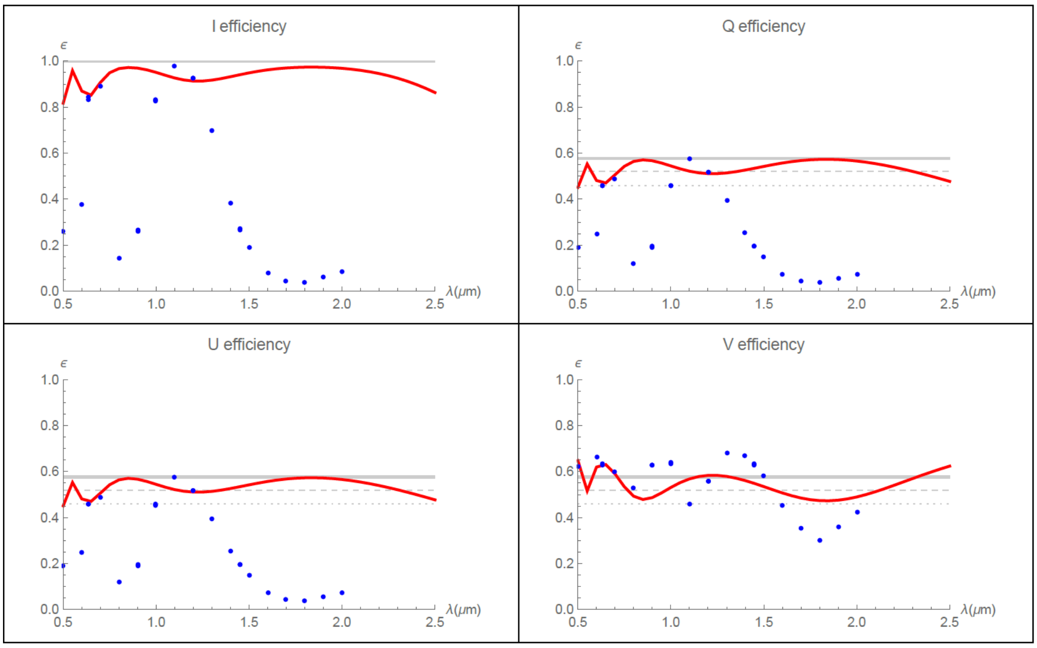

Figure 6.8: Fitted model(line) and measured data(points) modulation efficiency of the DL-NIRSP PCM from 500 nm to 2500 nm.

6.4 Conclusion

I verified that the test configurations for accepting the SAR and PCM components provide the necessary information to tell if Meadowlark has met the design requirements. Plans are already in motion to upgrade the measurement setup to be faster; more compact and work more efficiently. The plan is to use the new NLSP setup to provide Mueller matrix measurements during thermal and angle of incidence tests. Also, it has been agreed upon with Meadowlark that a temporary cell is needed to assemble the retarder and perform the clocking angle verification tests before the retarders are mounted in the final anodized aluminum cells. The temporary cell will be 3D printed with 8 flat sides to measure the retarder at 8 rotational positions during testing.

APPENDIX A - SUPER ACHROMATIC RETARDER DESIGN: SWIR MSPI QUARTER WAVE PLATE DESIGN

The design method illustrated in this appendix section was considered for the DKIST calibration retarders. However, bonding large diameter plates with different thermal expansion coefficients had a high risk of damage due to the solar flux relayed through the telescope.

Airborne and space-borne remote sensing systems play an important role in the characterization of aerosols in the environment, not to mention their influence on humans and the Earth's climate. An example of such a system is the Multiangle Imaging Spectroradiometer aboard NASA's Terra Satellite. A follow-on system is currently in development as a collaboration project between our lab and the Jet Propulsion Laboratory. It is called the Multiangle Spectro-polarimetric Imager, also known as MSPI.

MSPI is designed to measure degree of linear polarization (DoLP) to less than 0.5% uncertainty at spectral bands that span over the UV, Visible and Short Wavelength Infrared. MSPI is in the instrument incubator program at NASA, where new technologies to produce prototypes of a space-based instrument are developed. In order to perform proper modulation of the linear Stokes parameters MSPI utilizes two photoelastic modulators (PEMs) sandwiched between quarter wave retarders whose fast axes are at 45° and -45° relative to the PEM fast axis.

Several wavebands are selected to perform polarimetric measurements, and the retarders require a band averaged retardance within ±10° of 90° for all fields. There is an athermalization requirement of less than 0.1° change in retardance per 1°C temperature change. The materials used in the design of the wave plate must be space qualifiable, which means no UV darkening or outgassing. The material must be durable with excellent transmission from the ultraviolet to short wave infrared. Therefore it requires broadband achromatic retarders with specifications beyond stock retarder capabilities.

MSPI has two previous prototypes, GroundMSPI and AirMSPI, where new technologies were investigated during the design of each prototype. The polarimetric bands where GroundMSPI and AirMSPI are designed to measure DoLP are at 0.470, 0.660 and 0.865 µm. During the design of the AirMSPI quarter wave retarder Mahler found that quartz, MgF2 and sapphire were strong candidate materials for the design (Mahler et al., 2011). A combination of the three birefringent materials with fast axes clocked either parallel or 90° from one another created a super-achromatic quarter wave retarder over the wavelength range.

The next generation SWIR MSPI design required an extension of the polarimetric capabilities to include more spectral bands in the UV and short wave infrared (SWIR). In the first step of the SWIR MSPI retarder design phase, polarimetric wavebands were 0.445, 0.660, and 1.595 µm. It was after the initial design phase that there was an introduction of 3 more polarimetric wavebands, 0.410, 0.470, and 2.130 µm.

With three degrees of freedom, two were assigned for the shape of the retardance curve and one for temperature specification. This allowed us to perform a simultaneous optimization for retardance and athermalization.

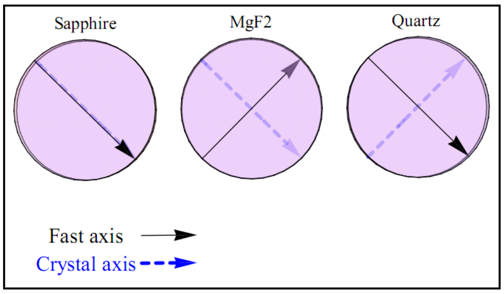

Figure 6.9: Axis orientations of the three crystal plates that make up the MSPI waveplate.

Figure 6.10 shows a 50° range in temperature from the nominal quarter wave plate working temperature. Since athermalization played a factor in the design of the wave plate, we achieved great athermal performance. Only a 0.03° change in retardance for a 1°C temperature change at the camera's current polarimetric channels.

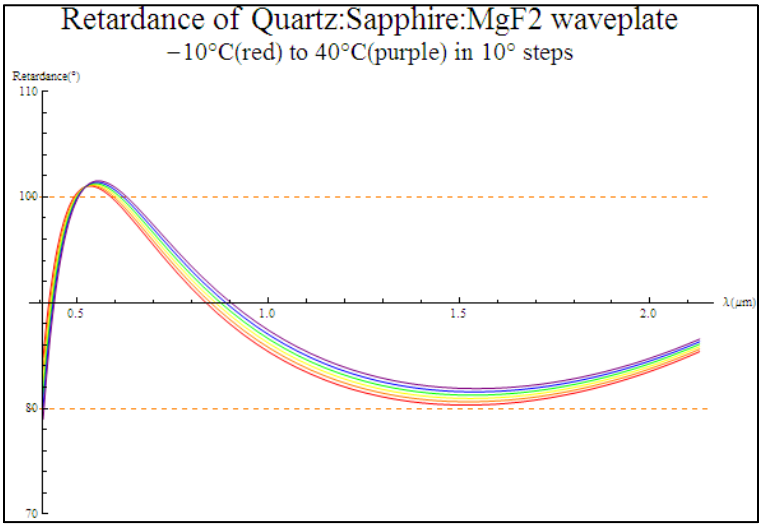

Figure 6.10: Retardance vs. temperature.

Angular dependence of the retardance is shown in Figure 6.11. With Polaris-M I performed a ray trace over a range of ±10° angle of incidence through the SWIR MSPI quarter wave plate. Plotted in Figure 6.11 is a contour plot, showing 9 field points seen by the MSPI camera. This MSPI camera will see over a 2° by 15° field of view. The contour lines represent the change in retardance with respect to the incidence angle.

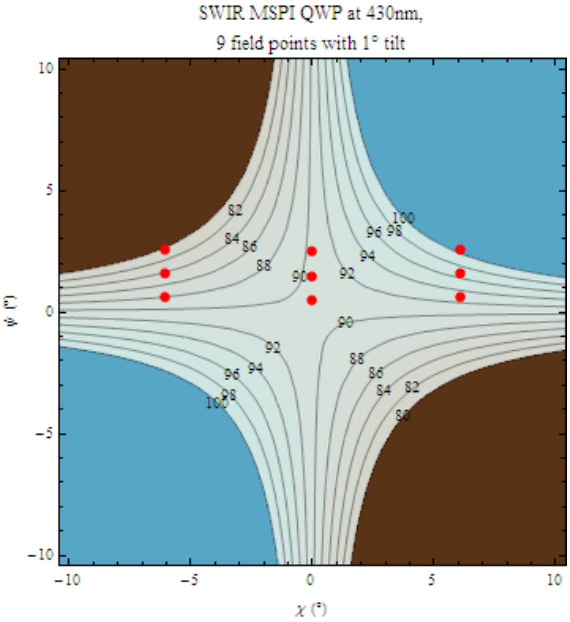

Figure 6.11: Retardance vs angle of incidence.

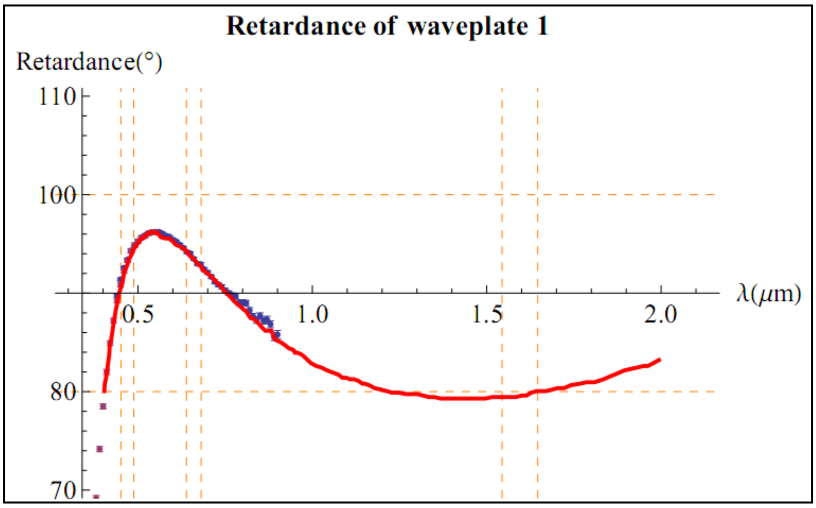

Figure 6.12: Retardance vs wavelength of SWIR MSPI quarter wave plate.

APPENDIX B – MORE MODELING OF CRYSTAL RETARDERS

THERMAL DEPENDENCE

The published information that exists on thermal effects of retarder elements is not consistent. We utilize equation (2.9) to model the effects of temperature shifts on retardance, where it is dependent on α, the thermal expansion coefficient of the crystal and $\frac{d\Delta n}{dT}$, the birefringence shift due to temperature.

In Table 6.3, there are two values of α tabled, one parallel to the crystal axis and the other perpendicular. Because we are only using A-plates, the expansion that will affect the thickness seen by the rays is along the axis perpendicular to the crystal axis.

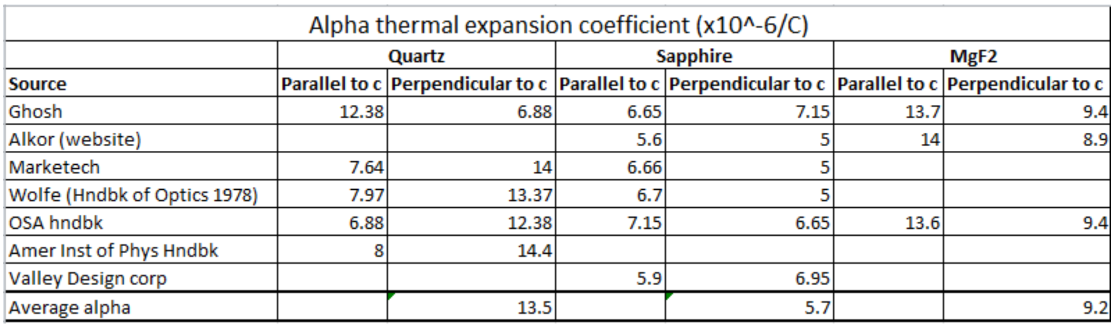

Alpha thermal expansion coefficient (x10^-6/C)

	Quartz		Sapphire		MgF2	
Source	Parallel to c	Perpendicular to c	Parallel to c	Perpendicular to c	Parallel to c	Perpendicular to c
Ghosh	12.38	6.88	6.65	7.15	13.7	9.4
Alkor (website)			5.6	5	14	8.9
Marketech	7.64	14	6.66	5		
Wolfe (Hndbk of Optics 1978)	7.97	13.37	6.7	5		
OSA hndbk	6.88	12.38	7.15	6.65	13.6	9.4
Amer Inst of Phys Hndbk	8	14.4				
Valley Design corp			5.9	6.95		
Average alpha		13.5		5.7		9.2

Table 6.3: Thermal expansion coefficients from various sources.

The change in birefringence caused by a shift in temperature is calculated with the formulas for $2n_e\frac{dn_e}{dT}$ and $2n_o\frac{dn_o}{dT}$ found in Ghosh (Gorachand Ghosh, 1998).

MULTIPLE REFLECTIONS

Multiple reflections within the 14 internal surfaces in the SAR and PCM designs are minimized with AR coatings and index matching oil. However, this reduces the reflected intensity at each surface but does not rule out the possibility of adverse effects occurring due to the multiple reflections. The goal of this section is to model the polarization effects of the ray splitting upon reflections in the crystal stack. All the possible double reflections that could occur in the retarders were traced, larger number of reflections were not included because the amount of flux was not significant. The retarder modeled in this section is the ViSP SAR. Since the materials are the same in the ViSP and DL-NIRSP retarders it was sufficient to perform the ray trace on only one of these designs. The Cryo-NIRSP retarders would experience even less multiple reflection effects since they are made of MgF2, a material with refractive index nearly matching the material between the substrates. The next section explains how the multiple reflection modeling is performed using Polaris-M.

The ViSP SAR design is set up in the same manner as section 4.3.2 for the angle of incidence ray trace. In addition to the optical system used in section 4.3.2.1, the air layers are replaced with the index of oil layers with index of 1.3 over the visible wavelength range. The ray trace is performed at 633.443 nm. The thickness of the oil layers should be very thin and is estimated at 15 µm for the model. The Infrasil substrates have been added as well, with an index of 1.45646 at 656.3nm(Infrasil spec sheet by Heraeus), which is the closest wavelength information to 633.443 nm at the time of the modeling. The thicknesses of the Infrasil substrates are 10 mm, and the thicknesses of the crystals are provided in Table 3.7. One design element that was not decided upon at the time of this ray trace was the AR coating specifications. Therefore, in this simulation AR coating parameters are not assigned. The addition of AR coatings would produce less reflection, so the modeled effect would be a worst-case scenario.

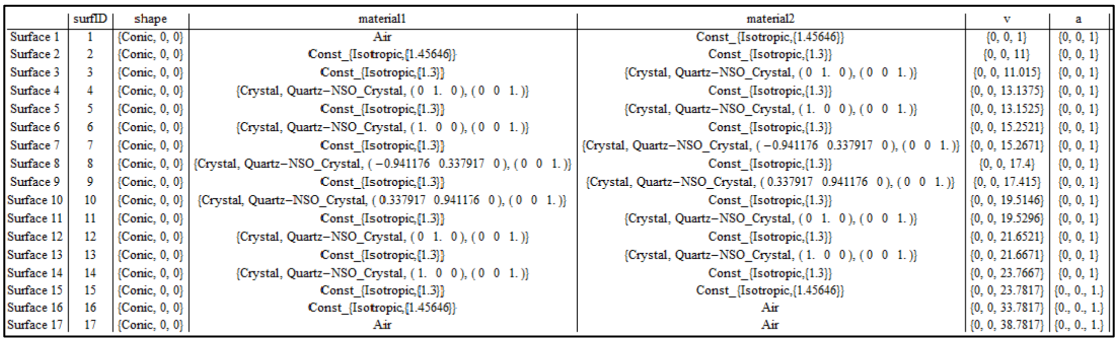

	surfID	shape	material1	material2	v	a
Surface 1	1	{Conic, 0, 0}	Air	Const_{Isotropic,{1.45646}}	{0, 0, 1}	{0, 0, 1}
Surface 2	2	{Conic, 0, 0}	Const_{Isotropic,{1.45646}}	Const_{Isotropic,{1.3}}	{0, 0, 11}	{0, 0, 1}
Surface 3	3	{Conic, 0, 0}	Const_{Isotropic,{1.3}}	{Crystal, Quartz−NSO_Crystal, (0 1. 0), (0 0 1.)}	{0, 0, 11.015}	{0, 0, 1}
Surface 4	4	{Conic, 0, 0}	{Crystal, Quartz−NSO_Crystal, (0 1. 0), (0 0 1.)}	Const_{Isotropic,{1.3}}	{0, 0, 13.1375}	{0, 0, 1}
Surface 5	5	{Conic, 0, 0}	Const_{Isotropic,{1.3}}	{Crystal, Quartz−NSO_Crystal, (1. 0 0), (0 0 1.)}	{0, 0, 13.1525}	{0, 0, 1}
Surface 6	6	{Conic, 0, 0}	{Crystal, Quartz−NSO_Crystal, (1. 0 0), (0 0 1.)}	Const_{Isotropic,{1.3}}	{0, 0, 15.2521}	{0, 0, 1}
Surface 7	7	{Conic, 0, 0}	Const_{Isotropic,{1.3}}	{Crystal, Quartz−NSO_Crystal, (−0.941176 0.337917 0), (0 0 1.)}	{0, 0, 15.2671}	{0, 0, 1}
Surface 8	8	{Conic, 0, 0}	{Crystal, Quartz−NSO_Crystal, (−0.941176 0.337917 0), (0 0 1.)}	Const_{Isotropic,{1.3}}	{0, 0, 17.4}	{0, 0, 1}
Surface 9	9	{Conic, 0, 0}	Const_{Isotropic,{1.3}}	{Crystal, Quartz−NSO_Crystal, (0.337917 0.941176 0), (0 0 1.)}	{0, 0, 17.415}	{0, 0, 1}
Surface 10	10	{Conic, 0, 0}	{Crystal, Quartz−NSO_Crystal, (0.337917 0.941176 0), (0 0 1.)}	Const_{Isotropic,{1.3}}	{0, 0, 19.5146}	{0, 0, 1}
Surface 11	11	{Conic, 0, 0}	Const_{Isotropic,{1.3}}	{Crystal, Quartz−NSO_Crystal, (0 1. 0), (0 0 1.)}	{0, 0, 19.5296}	{0, 0, 1}
Surface 12	12	{Conic, 0, 0}	{Crystal, Quartz−NSO_Crystal, (0 1. 0), (0 0 1.)}	Const_{Isotropic,{1.3}}	{0, 0, 21.6521}	{0, 0, 1}
Surface 13	13	{Conic, 0, 0}	Const_{Isotropic,{1.3}}	{Crystal, Quartz−NSO_Crystal, (1. 0 0), (0 0 1.)}	{0, 0, 21.6671}	{0, 0, 1}
Surface 14	14	{Conic, 0, 0}	{Crystal, Quartz−NSO_Crystal, (1. 0 0), (0 0 1.)}	Const_{Isotropic,{1.3}}	{0, 0, 23.7667}	{0, 0, 1}
Surface 15	15	{Conic, 0, 0}	Const_{Isotropic,{1.3}}	Const_{Isotropic,{1.45646}}	{0, 0, 23.7817}	{0., 0., 1.}
Surface 16	16	{Conic, 0, 0}	Const_{Isotropic,{1.45646}}	Air	{0, 0, 33.7817}	{0., 0., 1.}
Surface 17	17	{Conic, 0, 0}	Air	Air	{0, 0, 38.7817}	{0., 0., 1.}

Figure 6.13: System information given to PolarisM, 17 total surfaces.

To ray trace each double reflection in the retarder the ray surface order parameter in Polaris-M is used. This designates the surfaces where the incident ray would refract or reflect from. It was necessary to trace each double reflection one at a time. This way, similar to the angle of incidence ray tracing, all the rays are incoherently combined exiting the retarder to get the Mueller matrix that represents the particular double reflection.

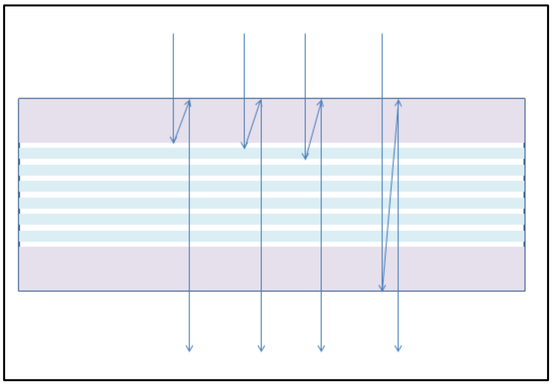

Figure 6.14: Example rays undergoing double reflections in a DKIST retarder. First incident ray is a double reflection between surface 1 and surface 2. Ray surface order is 1 2 1 2 3 4 5……15 16 17. This figure does not show the ray splitting at the birefringent surfaces.

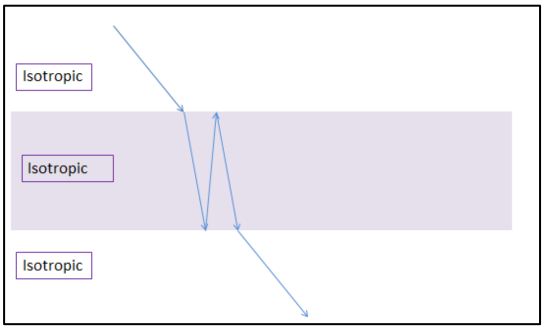

Figure 6.15: Example of double reflection in a isotropic medium.

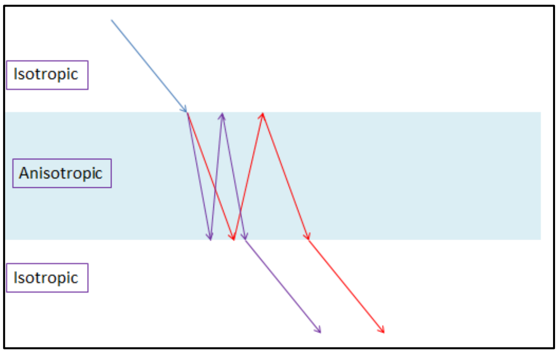

Figure 6.16: Example of double reflection in an anisotropic medium between two isotropic layers.

Because of the ray splitting in the birefringent crystals energy may split into the e and o modes of the crystal layers. Rays with Mueller matrix element $M_{0,0} < 10^{-10}$ are not saved. Any ray with a value smaller than this we consider negligible.

The PRT and MM for double reflections between every surface of the component are calculated. Summing together the Mueller matrices from each double reflection case results in less than 1% of the transmitted intensity.

APPENDIX C - MEADOWLARK RETARDER MEASUREMENTS

In the Statement of Work for the retarder assemblies, the vendor agreed to provide a data package of the measurements they perform. Subtracted retardances provided useful information when combined with our measurements to determine the clocking angles of the prototype assemblies. Measured data shown below were performed by Meadowlark and provided to the DKIST project through monthly progress reports.

MEASURED VALUES

To better understand the assembly's performance as a whole, measurements provided by Meadowlark will give us a deeper understanding of the contributions of the individual wave plate elements.

SUBSTRATES

Substrate average retardances were included in the 4th report, attached as an Appendix section: Cover window retardance tests by Hunter Schubert. 11 Infrasil plates and 3 CaF2 plates. 2 CaF2 plates were measured at 531 nm, in order to reduce noise all remaining plates were tested at 407 nm. Tabled below are the average retardances.

	Measurement wavelength	**Average retardance (nm)**	**Standard deviation (nm)**	**Average retardance (waves)**
Infrasil	407nm	0.284	0.139	7x10^-4
CaF2	2 @ 531nm, 1 @ 407nm	0.680	0.264	1.7x10^-3

Note the average retardance for CaF2 is calculated with retardance measurements at two wavelengths.

OPTIC AXIS ORIENTATION

First measurements of the optic axis tilt, Meadowlark show data that they are within tolerance, with an estimated error of ±0.005°. These external tilt angle measurements were made, and internal tilt angle calculated. Table from Meadowlark report #4.

Part No.	External Tilt Angle	Internal Tilt Angle
A1	0.2963°	0.05635°
A2	-0.7763°	-0.1476°
A3	-0.7097°	-0.13498°
A4	0.1724°	0.03279°
A5	-0.0588°	-0.011183°

Table 6.4: Optic axis orientation

Similarly, measurements were taken for the D bias plates. Table from Meadowlark report #5.

Part No.	Tilt Angle
DB-1	0.0305°
DB-2	0.0102°
DB-3	0.0837°
DB-4	0.1045°
DB-5	0.0146°

Table 6.5: Tilt angle

The MgF2 second ingot (first one broke) has a measured axis tilt of 0.01131°. The final MgF2 ingot has a measured axis tilt of 0.007°.

PLATE RETARDANCE

Bias plates for C, D and A pairs were polished to 30.80 waves at 633.443 nm. Measurements on E plate retardance were reported in November, but not the final polished down values.

RETARDANCE UNIFORMITY

Meadowlark provided a figure that indicates the points that they perform the uniformity tests.

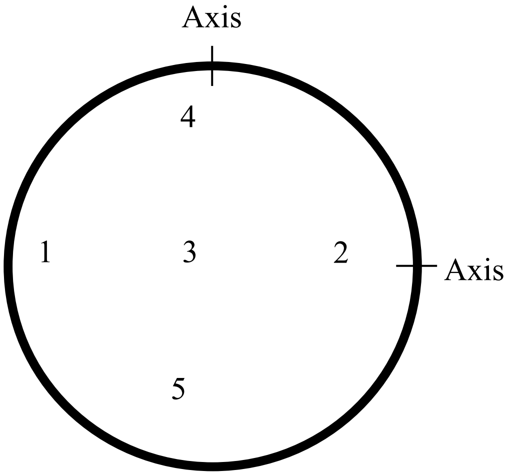

Figure 6.17: Measurement points over clear aperture.

Measurements in Meadowlark report #8 are of a G pair of the five points over the clear aperture as they get closer to the final retardance of 2.23 ± 0.01 waves at 633.443 nm. These are shown in the table below.

Location	**Retardance of G1 pair (waves at 633.443 nm)**
Center	2.2498
Location 1	2.2746
Location 2	2.2788
Location 3	2.2832
Location 4	2.2721

Table 6.6: G1 pair retardance over clear aperture.

6.4.1.1 TWE and beam deviation

Several measurements of the DL-NIRSP PCM show the change in TWE and beam deviation over time. A single measurement of DL-NIRSP SAR is tabulated as well.

Retarder	**Date**	**TWE w/ power removed**	**Beam deviation**
DL-NIRSP PCM	11/?/2014	0.195 waves	5.97 arc sec
DL-NIRSP PCM	12/1/2014	0.195 waves	8.7 arc sec
DL-NIRSP PCM	1/5/2015	0.201 waves	9.3 arc sec
DL-NIRSP PCM	1/27/2015	0.230 waves	9.7 arc sec
DL-NIRSP SAR	1/27/2015	0.395 waves	9.7 arc sec

Table 6.7: TWE and beam deviation measured with an interferometer at Meadowlark.

REFERENCES

Bass, M. (1995). *Handbook of Optics, Volume I - Fundamentals, Techniques, and Design*. (M. (CREOL) Bass, E. W. (CREOL) Van Stryland, D. R. (University of R. Willams, & W. L. (Optical S. C. Wolfe, Eds.) (Second). McGraw-Hill, Inc. http://doi.org/10.5860/CHOICE.32-5715

Bass, M., Van Stryland, E. W., Williams, D. R., & Wolfe, W. L. (Eds.). (1995). *Handbook of Optics, Volume II - Devices, Measurements, and Properties* (Second). McGraw-Hill, Inc. Retrieved from papers://101468bb-efe7-468f-814d-03d049c1bb3a/Paper/p861

Carvalho, A. (1898). Reserches de precision sur la dispersion infra-rouge du quartz. *Comptes Rendus*, *126*, 728–731.

Chandrasekharan, V., & Damany, H. (1968). Birefringence of sapphire, magnesium fluoride, and quartz in the vacuum ultraviolet, and retardation plates. *Applied Optics*, *7*(5), 939–941. http://doi.org/10.1364/AO.7.000939

Chipman, R. A. (1995). Polarimetry. In M. Bass (Ed.), *Handbook of Optics* (2nd ed., pp. 22.1–22.37). New York: McGraw-Hill, Inc.

Chipman, R. A. (College of O. S., Yun, G., & Lam, W. S. T. (2017). 9.6 Polarization ray tracing matrices for addition. In *Polarized Light in Optical Systems*.

CVI, M. G. (2003). Material Properties CVI Melles Griot. Retrieved from http://books.google.be/books?id=OE1TIkBr1I4C

de Wijn, A. G., Casini, R., Nelson, P. G., & Huang, P. (2012). Preliminary design of the Visible Spectro-Polarimeter for the Advanced Technology Solar Telescope. In *Proceedings of SPIE*.

de Wijn, A. G., Tomczyk, S., Casini, R., & Nelson, P. G. (2011). Wavelength-diverse polarization modulators for Stokes polarimetry. *Solar Polarization 6*, *437*, 413–

421. http://doi.org/10.1364/AO.49.003580

del Toro Iniesta, J. C., & Collados, M. (2000). Optimum modulation and demodulation matrices for solar polarimetry. *Applied Optics*, *39*(10), 1637–1642. http://doi.org/10.1364/AO.39.001637

Dodge, M. J. (1984). Refractive properties of magnesium fluoride. *Applied Optics*, *23*(12), 1980. http://doi.org/10.1364/AO.23.001980

Elmore, D. F. (2013). Polarization Calibration of the Advanced Technology Solar Telescope. *Solar Polarization 7, Astronomical Society of the Pacific*, *489*, 279–288.

Elmore, D. F., Lin, H., Socas Navarro, H., & Jaeggli, S. a. (2010). Utilization of redundant polarized solar spectra to infer the polarization properties of the new generation of large aperture solar telescopes. *Proceedings of SPIE Ground-Based and Airborne Instrumentation for Astronomy*, *7735*, 77354E–77354E–6. http://doi.org/10.1117/12.857061

Elmore, D. F., Rimmele, T., Casini, R., Hegwer, S., Kuhn, J., Lin, H., … Wöger, F. (2014). The Daniel K. Inouye Solar Telescope first light instruments and critical science plan. *Proceedings of SPIE Ground-Based and Airborne Instrumentation for Astronomy*, *9147*, 914707. http://doi.org/10.1117/12.2057038

Elmore, D. F., Sueoka, S. R., & Casini, R. (2014). Performance of polarization modulation and calibration optics for the Daniel K. Inouye Solar Telescope. *Ground-Based and Airborne Instrumentation for Astronomy V, Proceedings of SPIE*, *9147*, 91470F. http://doi.org/10.1117/12.2054610

Elmore, D., Ferayorni, A., Hansen, E., & Hegwer, S. (2014). *Polarimetry Analysis and Calibration Design Requirements Document, DKIST SPEC-0080*.

Ghosh, G. (1998). *Handbook of Optical Constants of Solids: Handbook of Thermo-*

Optic Coefficients of Optical Materials with Applications. Academic Press.

Ghosh, G. (1998). Sellmeier Coefficients for the Birefringence and Refractive Indices of ZnGeP(2) Nonlinear Crystal at Different Temperatures. *Applied Optics*, *37*(7), 1205–1212. http://doi.org/10.1364/AO.37.001205

Ghosh, G. (1999). Dispersion-equation coefficients for the refractive index and birefringence of calcite and quartz crystals. *Optics Communications*, *163*(1), 95–102. http://doi.org/10.1016/S0030-4018(99)00091-7

Gray, D. E. (Ed.). (1957). *American Institute of Physics Handbook*. McGraw-Hill, Inc.

Hale, P. D., & Day, G. W. (1988). Stability of birefringent linear retarders (waveplates). *Applied Optics*, *27*(24), 5146–5153. http://doi.org/10.1364/AO.27.005146

Hardy, A. C., & Perrin, F. H. (1932). *The Principles of Optics*. New York and London: McGraw-Hill, Inc.

Hill, F., Beckers, J., Brandt, P., Briggs, J., Brown, T., Brown, W., … Streander, K. (2006). Solar site testing for the Advanced Technology Solar Telescope. *Proceedings of SPIE Ground-Based and Airborne Telescopes*, *6267*. http://doi.org/10.1117/12.551812

Jenkins, F. A. (University of C., & White, H. E. (University of C. (1957). *Fundamentals of Optics* (Third). McGraw-Hill, Inc.

Lam, W. S. T., McClain, S., Smith, G., & Chipman, R. (2010). Ray Tracing in Biaxial Materials. *International Optical Design Conference and Optical Fabrication and Testing*, IWA1. http://doi.org/10.1364/IODC.2010.IWA1

Lu, S.-Y., & Chipman, R. a. (1996). Interpretation of Mueller matrices based on polar decomposition. *Journal of the Optical Society of America A*, *13*(5), 1106.

http://doi.org/10.1364/JOSAA.13.001106

Mahler, A.-B., McClain, S., & Chipman, R. (2011). Achromatic athermalized retarder fabrication. *Applied Optics*, *50*(5), 755–765. http://doi.org/10.1364/AO.50.000755

Malitson, I. H., & Dodge, M. J. (1972). Refractive Index and Birefringence of Synthentic Sapphire (p. 1405).

Mcclain, S. C., & Chipman, R. a. (1992). Polarization ray tracing in anisotropic optically active media, *1746*. http://doi.org/10.1364/JOSAA.10.002371

Navarro, H. S., Beckers, J., Brandt, P., Briggs, J., Brown, T., Brown, W., … Streander, K. (2005). Solar Site Survey for the Advanced Technology Solar Telescope . I . Analysis of the Seeing Data. *Astronomical Society of the Pacific*, *117*, 1296–1305. http://doi.org/10.1086/496939

Ossikovski, R. (2009). Analysis of depolarizing Mueller matrices through a symmetric decomposition. *Journal of the Optical Society of America. A, Optics, Image Science, and Vision*, *26*(5), 1109–1118. http://doi.org/10.1364/JOSAA.26.001109

Pancharatnam, S. (Raman Research Institute, B. (1955). Achromatic Combination of Birefringent Plates Part II. An Achromatic Quarter-Wave Plate. *Proceedings of the Indian Academy of Sciences*, *41*(4), 137–144.

Philipp, H. R. (1985). Silicon Dioxide (SiO2), Type α (Crystalline). *Handbook of Optical Constants of Solids*, 719–747. http://doi.org/10.1016/B978-0-08-054721-3.50039-3

Radhakrishnan, T. (1951). Futher studies on the temperature variation of the refractive index of crystals. *Proceedings of the Indian Academy of Sciences*, 22–34.

Rimmele, T. (2005). *ATST Science Requirements Document, DKIST SPEC-0001.*

Rimmele, T. R., Wagner, J., Keil, S., Elmore, D., Hubbard, R., Hansen, E., … Ditsler, J. (2010). The Advanced Technology Solar Telescope: beginning construction of the world's largest solar telescope. *Proceedings of SPIE Ground-Based and Airborne Telescopes*, *7733*, 77330G–77330G–17. http://doi.org/10.1117/12.857714

Snik, F., Harten, G. Van, Navarro, R., Groot, P., Kaper, L., & Wijn, A. De. (2012). Design of a Full-Stokes Polarimeter for VLT/X-shooter. *Ground-Based and Airborne Instrumentation for Astronomy IV, Proceedings of SPIE*, *8446*, 1–15. http://doi.org/10.1117/12.926163

Sosman, R. B. (1927). *The Properties of Silica*. Book Dept., The Chemical Catalog Co.

Tomczyk, S., Casini, R., de Wijn, A. G., & Nelson, P. G. (2010). Wavelength-diverse polarization modulators for Stokes polarimetry. *Applied Optics*, *49*(18), 3580–3586. http://doi.org/10.1364/AO.49.003580

Yun, G., Crabtree, K., & Chipman, R. a. (2011). Three-dimensional polarization ray-tracing calculus I: definition and diattenuation. *Applied Optics*, *50*(18), 2866–2874. http://doi.org/10.1364/AO.50.002866

Yun, G., Mcclain, S. C., & Chipman, R. a. (2011). Three dimensional polarization ray tracing calculus II : retardance. *Journal of the Optical Society of America*, *50*(18), 2866–2874.